MASTER THESIS

Langmuir Turbulence in the HYCOM Ocean Model

by

Mika Malila

Supervisors

Øyvind Breivik

Alfatih Ali

Thesis submitted in partial fulfilment of the requirements for the degree of Master of Science

in the

Master's Programme in Meteorology and Oceanography
Specialisation: Physical Oceanography
Geophysical Institute
UNIVERSITY OF BERGEN

December 2017

Declaration of Authorship

I, Mika Malila, declare that this thesis titled, 'Langmuir Turbulence in the HYCOM Ocean Model' and the work presented in it are my own. I confirm that:

- This work was done wholly or mainly while in candidature for a research degree at this University.
- Where any part of this thesis has previously been submitted for a degree or any other qualification at this University or any other institution, this has been clearly stated.
- Where I have consulted the published work of others, this is always clearly attributed.
- Where I have quoted from the work of others, the source is always given. With the exception of such quotations, this thesis is entirely my own work.
- I have acknowledged all main sources of help.
- Where the thesis is based on work done by myself jointly with others, I have made clear exactly what was done by others and what I have contributed myself.

"There is no such thing as turbulence without waves."

M.E. McIntyre

MASTER THESIS

Langmuir Turbulence in the HYCOM Ocean Model

Abstract

by Mika Malila

The impact of parameterising the turbulent mixing induced by surface wave-driven Langmuir turbulence is investigated for a basin-scale configuration of the hybrid-coordinate ocean circulation model HYCOM. Two-year, non-data assimilative model simulations are performed within the North Atlantic model domain of the operational ocean forecasting system TOPAZ4, with surface wave parameters acquired from a hindcast produced using the WaveWatch III spectral wave model. The model runs consist of one control simulation in which explicit surface wave effects are neglected, and four additional simulations, each of which implements a different modification of the K profile parameterisation (KPP) upper-ocean mixing scheme to account for the Langmuir turbulence effects. The model response to the mixing scheme modifications is analysed in terms of the mixed layer depth (MLD), the sea surface temperature (SST) and vertical temperature profiles. The largest improvements in model performance attributed to the inclusion of the Langmuir turbulence parameterisations are observed in the summer season, when the standard model configuration is shown to underestimate the mixing in the upper ocean boundary layer (OBL). In the winter, the introduction of the parameterisations tends to create exaggerated levels of near-surface mixing, leading to increased errors and biases in the model temperature fields when compared to observational datasets. It is concluded that the present set of Langmuir turbulence parameterisations implemented in the KPP code of HYCOM is inadequate for the purpose of improving the operational forecasting skill of HYCOM in a year-round, realistic North Atlantic setting—continued development and testing of alternative parameterisations is, therefore, required. It is proposed that developers seeking improved parameterisations of the process focus on validating dimensionless scaling laws of surface wave-forced boundary layers, incorporating parameters to account for varying water mass stratification, and developing methods to allow for stabilising effects in conditions of opposing surface waves and currents.

Acknowledgements

A big thank you, first and foremost, to my supervisors Øyvind Breivik, at the Norwegian Meteorological Institute (MET) and the Geophysical Institute (GFI), and Alfatih Ali at the Nansen Environmental and Remote Sensing Center (NERSC)—Øyvind for the excellent theoretical advice, and Alfatih for never hesitating to help with the numerous model-related issues I have come across. I have also received valuable help on various practical issues from Annette Samuelsen, Jiping Xie, Roshin Raj and Laurent Bertino at the ocean modelling group at NERSC. Thanks also to Francois Counillon (NERSC) for the help with the comparison of the vertical temperature profiles and, not least, for making me aware of the possibility of writing this thesis at NERSC. Kai Christensen (MET), Graig Sutherland (MET), Mostafa Bakhoday (NERSC), Alastair Jenkins (GFI) and Satoshi Kimura (currently at the Japan Agency for Marine-Earth Science and Technology, JAMSTEC) have all provided stimulating theoretical input for which I am very grateful. Finally, thanks to Jarle Berntsen (University of Bergen, UiB) for initially sparking my interest in surface waves and turbulence. The work in this thesis has been funded in part by NERSC and RETROSPECT, a joint project between MET, NERSC and the Institute of Marine Research (IMR). NERSC has also kindly provided me with office space and access to free coffee.

Contents

List of Figures

List of Tables

Frequently Occurring Abbreviations

ABL	**A**tmospheric **B**oundary **L**ayer
CL	**C**raik-**L**eibovich theory of Langmuir circulation
GLM	**G**eneralised **L**agrangian **M**ean
HYCOM	**HY**brid **C**oordinate **O**cean **M**odel
KPP	**K** **P**rofile **P**arameterisation mixed layer scheme
LES	**L**arge **E**ddy **S**imulation
MLD	**M**ixed **L**ayer **D**epth
NERSC	**N**ansen **E**nvironmental and **R**emote **S**ensing **C**enter
OBL	**O**ceanic **B**oundary **L**ayer
OGCM	**O**cean **G**eneral **C**irculation **M**odel
SST	**S**ea **S**urface **T**emperature
TKE	**T**urbulent **K**inetic **E**nergy
WW3	**W**ave**W**atch **III** surface wave model

Chapter 1

Introduction

1.1 The Oceanic Boundary Layer (OBL)

The air–sea interface acts as a mediator of key climatic factors such as heat, momentum, and gases between the energetic boundary layers of the upper ocean (OBL) and the lower atmosphere (ABL) [Jähne and Haußecker, 1998]. An important quantity regulating the interfacial exchange processes is the sea-surface temperature (SST), the accurate knowledge of which is crucial for estimating, for instance, the Earth surface energy budget [Fairall et al., 1996], forecasted hurricane intensity [Emanuel, 1999], the rate of gas transfer across the air–sea interface [Wanninkhof et al., 2009], and biological productivity in the OBL [Behrenfeld et al., 2006]. The temperature of the sea surface depends to a large degree on the intensity of vertical mixing in the OBL [Large et al., 1994]; this mixing tends to create a layer of uniform temperature, salinity and, consequently, density known as the mixed layer [de Boyer Montégut et al., 2004]. The mixed layer depth (MLD) is a measure of the vertical reach of the mixing processes that originate on the sea surface, mainly as a result of wind and heat forcing, and is subject to considerable temporal variability ranging from diurnal to seasonal time scales [Kara et al., 2003].

1.1.1 Boundary Layer Turbulence

Oceanic vertical mixing is, similarly to the mixing that occurs in the ABL, inherently turbulent, and thus occupies a wide range of mutually interactive temporal and spatial scales [e.g., Kantha and Clayson, 2000, p. 4]. The complexity of turbulent flows—their nonlinearity and apparent stochastic nature, combined with the ensuing closure problem pertaining to the mean flow equations—makes their analytical treatment difficult. Although direct numerical simulations of the governing equations of motion provide valuable insights into the behaviour of turbulent flows, currently available computing power only allows the full spectrum of scales to be resolved

in severely restricted and idealised domains [e.g. Ishihara et al., 2009]. For this reason, the computationally costly numerical models that strive to simulate large-scale natural systems such as the ocean or the atmosphere must resort to parameterising—that is, estimating in terms of known or resolvable parameters—the *subgrid-scale* turbulent processes.

The turbulence in the OBL [and to a lesser degree in the marine ABL; see, e.g., Belcher and Hunt, 1998; Charnock, 1955; Paskyabi et al., 2014] differs markedly from that in the terrestrial ABL in that the upper ocean is forced from above by a free, wavy sea surface, whereas the turbulence in the lower atmosphere stems from a comparatively rigid lower boundary: the ground [Sullivan and McWilliams, 2010]. The field of wind-generated surface gravity waves that regularly forms on the sea surface introduces two significant—and often coexisting—sources of oceanic turbulence that are absent in traditional, wall-bounded shear flows, namely surface wave breaking [Melville, 1996] and Langmuir circulation [Leibovich, 1983; Thorpe, 2004]. The latter of these two processes is a key component in the subject of the present study: the surface wave-forced OBL turbulence regime known as Langmuir turbulence [McWilliams et al., 1997].

1.1.2 Wave Breaking

The intermittent breaking, or whitecapping, of open-ocean surface waves is a small-scale process that greatly enhances near-surface turbulent dissipation and mixing in the ocean [Agrawal et al., 1992]. Its effects, however, are largely confined to a relatively shallow depth comparable to the prevailing significant wave height [Noh et al., 2004; Terray et al., 1996]. The main mechanism by which breaking waves contribute to the production of turbulent kinetic energy (TKE) is believed to be the strong velocity shear on the breaking (forward) sides of the waves and adjacent to the buoyant air bubbles that become submerged as a result of the breaking [Ardhuin and Jenkins, 2006]. The dissipation of wave energy by wave breaking is also an important source term in the energy balance equation used to compute the evolution of the wave energy spectrum in third-generation numerical wave models [Holthuijsen, 2010; Komen et al., 1994]. Wave breaking is traditionally parameterised in large-scale ocean models as either a surface boundary condition [Craig and Banner, 1994] or, more recently, as a stochastic source term for the resolved momentum and the turbulent kinetic energy (TKE) [Sullivan et al., 2004]. Although a potent source of near-surface turbulence, wave breaking is thought to be largely independent from the deeper-reaching Langmuir turbulence [e.g., Sullivan et al., 2007]; its effects on OBL mixing are hence not analysed further in the present study.

1.1.3 Langmuir Circulation

A more indirect mechanism than wave breaking, Langmuir circulation—pictured schematically in Figure 1.1—refers to a system of roll-shaped helical vortices that frequently forms in the upper OBL in the presence of wind and surface waves, and was first studied by Langmuir [1938]. The presence of Langmuir circulation is often apparent to casual observers, owing to its characteristic surface signature of roughly wind-aligned convergence streaks, or windrows, composed of buoyant material such as foam and algae. The spacing between individual windrows can vary between a few metres to roughly one kilometre, and elevated downwind and downwelling velocities are generally found within and directly beneath the surface streaks, respectively [e.g., Thorpe, 2004]. Dynamically, current theory holds that the circulation is generated by an instability mechanism related to the interaction between the mean Lagrangian (Stokes) drift of the surface waves and the vorticity induced by sheared surface currents [Craik and Leibovich, 1976]. In the most widely acknowledged theoretical model—the second Craik-Leibovich instability mechanism, or CL2 for short [Craik, 1977; Leibovich, 1977a]—the vertical vorticity induced by a disturbance of the mean surface current is tilted into the horizontal by the vertical shear of the Stokes drift. The mathematical manifestation of the torquing effect of the Stokes drift in the wave phase-averaged equations of the mean flow—also known as the Craik-Leibovich (CL) equations—is in the form of a modified pressure and a vortex force term [Leibovich, 1983], or, more contemporarily, a Stokes shear force [Suzuki and Fox-Kemper, 2016].

1.1.4 Langmuir Turbulence

Measurements of the OBL—obtained using current profilers and artificial surface drifters [Kukulka et al., 2009; Plueddemann et al., 1996; Weller and Price, 1988], bubble cloud-detecting side-scan sonar [Farmer and Li, 1995; Thorpe, 1984], and autonomous subsurface drifters [Gemmrich and Farmer, 1999; Thorpe et al., 2003]—as well as numerical large-eddy simulations (LES) of the CL equations [Grant and Belcher, 2009; Harcourt and D'Asaro, 2008; McWilliams et al., 1997; Skyllingstad and Denbo, 1995] indicate that the wave-forced OBL is a separate parameter regime with distinct characteristics from classical shear and buoyancy-driven boundary layers. Oceanic turbulence modified by the presence of Langmuir circulations is commonly referred to as Langmuir turbulence, following McWilliams et al. [1997]. In Langmuir turbulence, vertical turbulent fluxes and turbulent dissipation in the OBL are generally enhanced, and coherent structures are often observed in the velocity field as a result of Langmuir circulation cells. These velocity structures are characterised by elevated vertical and crosswind velocity fluctuations in relation to downwind velocity fluctuations; the converse is often the case in pure shear flows, in which downwind velocity fluctuations dominate over the crosswind and vertical components [Li et al., 2005].

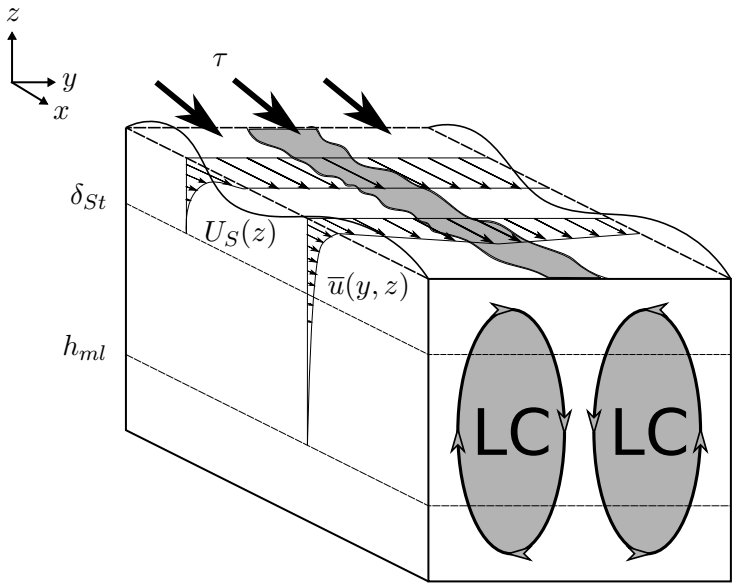

FIGURE 1.1: Schematic showing two alternating streamwise Langmuir circulation cells (denoted LC), with converging flow in the middle, often leading to a strong downwelling jet, and weaker upwelling zones on the sides. Shown in thin arrows are also an Eulerian mean current profile $\overline{u}(y,z)$ and a horizontally uniform Stokes drift profile $U_S(z)$. Note how the Stokes drift profile decays rapidly over its e-folding depth δ_{St}, whereas the mean current—with a surface maximum in the convergence zone of the Langmuir cells (the windrow, drawn as a grey streak)—reaches deeper into the OBL. Empirical estimates state that the surface Stokes drift magnitude U_{S0} can reach approximately 1% of the wind speed, whereas the Eulerian currents are generally slightly lower, on the order of 0.6% of the wind speed [Ardhuin et al., 2009]. The mixed layer depth, which typically exceeds the Stokes depth δ_{St}, is denoted by h_{ml}. The thick black arrows represent the wind stress τ, and the wavy contours illustrate the surface wave field.

1.2 Wave Effects in Ocean Models

Surface wave-induced effects on the vertical mixing in the OBL have until relatively recently not been explicitly included in global ocean and climate models, despite estimates that of the roughly 19 TW of wind energy that is absorbed by the surface wave field globally [Wunsch and Ferrari, 2004], between 2.5 [Kantha et al., 2009] and 4.5 TW [Rascle and Ardhuin, 2013] is available for the generation of Langmuir circulation alone. Several authors [e.g. Belcher et al., 2012; D'Asaro et al., 2014; Fan and Griffies, 2014; Sutherland et al., 2014] have argued that incorporating parameterisations of surface wave processes may improve model performance in reproducing key OBL properties such as the SST and the MLD, both of which at present appear systematically over- or underestimated by models in key regions [Belcher et al., 2012; Fox-Kemper et al., 2011; Sallée et al., 2013; Weijer et al., 2012].

Traditionally, the turbulence schemes designed to represent unresolved vertical mixing processes in numerical ocean models, such as the non-local K-profile parameterisation (KPP) of Large

et al. [1994] or the two-equation Mellor and Yamada [1982] scheme and its descendants [e.g., Kantha and Clayson, 1994], have borrowed their basic framework from schemes developed for modelling atmospheric turbulence. Consequently, the original versions of these schemes disregard the effects of surface waves [Kantha and Clayson, 2004; McWilliams and Sullivan, 2000], although this omission has generally been recognised as potentially problematic by the developers [Large et al., 1994; Mellor and Yamada, 1982].

1.2.1 Parameterisations

Attempts have subsequently been made to parameterise the effects of Langmuir turbulence for use in the mixing schemes of large-scale ocean models. The earliest such attempt was by McWilliams and Sullivan [2000], who formulated a modification to the KPP scheme that produced velocity and scalar profiles in conformity with LES experiments of the CL equations and previous oceanic measurements. The modification involves enhancing the turbulent velocity scale, used in KPP to determine the vertical profile of the turbulent diffusion K in the OBL, by multiplication with a function intended to represent the increased mixing due to Langmuir turbulence. This function, or enhancement factor, is defined as a function of both the friction velocity of the water (a measure of the shear production of turbulent energy induced directly by the wind stress) and the magnitude of the Stokes drift of the waves, such that the mixing increases as the Stokes drift strengthens in relation to the friction velocity; or, equivalently, as Langmuir turbulence takes precedence over shear-driven turbulence. The McWilliams and Sullivan [2000] parameterisation has received subsequent modifications to include effects that were initially neglected [e.g., Smyth et al., 2002], but their basic principle, that is, the enhancement of the modelled turbulence intensity by a parameter dependent on the surface wave field, has remained at the core of parameterisations of Langmuir turbulence in the KPP scheme [e.g., Harcourt and D'Asaro, 2008; Takaya et al., 2010].

At present, global and basin-scale ocean general circulation models (OGCMs) with horizontal resolutions of $\mathcal{O}(10)$ km are incapable of resolving the surface gravity wave motions, which take place on scales of $\mathcal{O}(0.1 - 100)$ m. Consequently, surface waves are typically represented in large-scale models as a surface forcing obtained by running a separate prognostic wave model. To conform with prevailing theory [Craik and Leibovich, 1976], the parameter that is input from the wave model is often taken to be the surface value of the Stokes drift; certain recent studies [Harcourt and D'Asaro, 2008; Li and Fox-Kemper, 2017; Van Roekel et al., 2012], however, advocate the use of vertically averaged values instead, pointing to the high sensitivity of the surface value to unresolved high-frequency spectral components. In an effort to circumvent the added computational costs of running a dedicated wave model, Li et al. [2017] have recently developed statistical lookup tables of climatological Langmuir turbulence enhancement factors for

use in KPP. It remains to be seen whether this approach can effectively replace the dependence of the parameterisations on input from separate wave models.

1.2.2 Prior Implementations of Parameterisations in Ocean Models

In an early effort to include surface wave effects in a global climate model (CLIMBER-2), Babanin et al. [2009] parameterised the mixing induced by Langmuir turbulence purely in terms of the wind forcing. Despite the crude formulation, the study showed significant modifications in the modelled temperature distributions as well as improved agreement with a global MLD climatology, with a resulting impact on global atmospheric pressure fields and local precipitation patterns. Wang et al. [2010] modified the KPP scheme of a quasi-global ocean model (ROMS) to accommodate for the direct impact of wave orbital velocities on the mixed-layer dynamics. Distinct from the Langmuir turbulence theories described above, this so-called Bv approach [Qiao et al., 2004] assumes that the turbulence induced by the wave motions constitutes an additive effect on the OBL diffusivity, in contrast to the nonlinear enhancement of the turbulent velocities inherent in the McWilliams and Sullivan [2000] formulation. It was found by Wang et al. [2010] that root mean square errors (RMSE) of modelled near-surface temperatures were reduced in the wave-modified test runs compared to model integrations in which explicit surface-wave effects were neglected.

In the study of Fan and Griffies [2014]—presumably the first research paper to publish results of implementing existing KPP parameterisations of Langmuir turbulence in a global climate simulation—a coupled ocean-wave-atmosphere model was fitted with the McWilliams and Sullivan [2000] and Smyth et al. [2002] modifications to the KPP scheme; their results indicate that the enhanced mixing induced by the McWilliams and Sullivan [2000] proposition probably overestimates the surface wave impact in the winter season, whereas the Smyth et al. [2002] model, which has an explicit dependency on the stability of the OBL stratification, was found to improve modelled winter MLD estimates when compared to climatological values. Recently, Li et al. [2016] conducted similar coupled climate simulations, incorporating the McWilliams and Sullivan [2000] and Smyth et al. [2002] parameterisations into the KPP scheme of the CESM1.2 Earth system model. They found that both parameterisations induce an excessive amount of mixing in all seasons; more promising results (in the form of reduced MLD and tracer concentration biases) were observed using alternative formulations of the wave-induced enhancement factor [see Van Roekel et al., 2012].

1.3 Goals and Structure of the Thesis

The present thesis compares the effects of incorporating four different parameterisations of Langmuir turbulence in the KPP mixing scheme of the Hybrid Coordinate Ocean Model (HYCOM) [Bleck et al., 2002] implemented in the operational TOPAZ4 ocean forecasting system [Sakov et al., 2012] at the Nansen Environmental and Remote Sensing Center (NERSC). The basin-scale model configuration covers the North Atlantic Ocean with an eddy-permitting horizontal resolution of 1/12°, and the parameterisations included in the study are those formulated by McWilliams and Sullivan [2000], Smyth et al. [2002], Harcourt and D'Asaro [2008], and Takaya et al. [2010]. Apart from Li et al. [2013], who implemented and tested a Langmuir turbulence modification of the Mellor and Yamada [1982] scheme in the South China Sea, as well as ongoing work by Dr. Alfatih Ali at NERSC, the author is unaware of additional studies concerning the basin-scale impact of parameterising Langmuir turbulence in KPP. Furthermore, surface-wave effects on the mixing have previously not been assessed for the HYCOM model. Additionally, many of the previous studies have focused on the long-time scale, climatic aspects of incorporating wave-induced mixing, whereas the present study is more inclined toward the operational application of the mixing parameterisations.

The results obtained from the two-year HYCOM integrations in the present study partly echo the previous results obtained in the climate-scale simulations of Fan and Griffies [2014] and Li et al. [2016], that is, the wintertime mixing in mid-latitude regions characterised by strong winds and rough wind seas is likely overestimated by the majority of the parameterisations, as evidenced by increased near-surface temperature biases and weaker correspondence to reanalysed SST data. A more positive impact is, however, observed in summer months, in which the enhanced mixing—induced especially by the Smyth et al. [2002] parameterisation—helps alleviate the cold SST biases of the standard HYCOM configuration which neglects explicit surface-wave effects. Promising results are also obtained with the Takaya et al. [2010] parameterisation, which is based on a similarity scaling law of Langmuir turbulence proposed by Grant and Belcher [2009].

The present thesis is structured in the following manner. A brief introduction to general ocean model characteristics, including a description of the KPP mixing scheme, is followed by a rather thorough review of the theory of Langmuir circulation and Langmuir turbulence—subjects that rarely feature in graduate level geophysical fluid dynamics courses—in Chapter 2. In Chapter 3, the experimental setup as well as the forcing and observational datasets are presented. The results of the HYCOM model runs are described in Chapter 4, and discussed in relation to previous studies in Chapter 5. The thesis concludes with a summary in Chapter 6.

Chapter 2

Model Description and Theoretical Foundations

2.1 The Ocean Model

The numerical experiments in the present study are performed using the Hybrid Coordinate Ocean Model (HYCOM) [Bleck, 2002] implemented in the TOPAZ4 ocean data assimilation system [Sakov et al., 2012], developed at NERSC.[1] HYCOM is a hydrostatic, mass-conserving ocean general circulation model (OGCM) with its foundation in the Miami Isopycnic-Coordinate Ocean Model (MICOM) [Bleck et al., 1992]. The model derives its name from the flexibility it provides in the choice of vertical coordinate: simulations can be run in purely isopycnic (i.e., constant potential density surface), z- (or p-) level (i.e., constant depth (pressure) surface), or sigma (i.e., terrain following) coordinates, or in 'hybrid' mode, in which smooth transitions occur between optimal vertical coordinate choices for each local topographic and water mass characteristic. The standard setup in HYCOM uses isopycnal coordinates in deep, stratified ocean environments; z-level coordinates in near-surface, well-mixed waters; and sigma coordinates in shallow coastal areas [e.g., Chassignet et al., 2007].

The numerical solution of partial differential equations, such as the Navier-Stokes equations that govern the motion of the water in the ocean, requires a discretisation of the continuous functions into algebraic expressions that can be solved by computers. The most common discretisation method among current OGCMs is finite differencing—a technique in which the infinitesimal differentials are replaced by discrete intervals in both space and time [e.g., Haltiner and Terry, 1980, p. 109]. Invariably, the approximations necessitated by this discretisation process give rise to residuals, known as truncation errors, that characterise the degree to which the numerical

[1] The model runs performed in this study are so-called free runs, meaning that the model is allowed to evolve on its own without data assimilative input.

approximations deviate from the original, continuous expressions [e.g., Durran, 2010, p. 36]. Reducing the size of the numerical mesh, that is, using smaller spatial grid cells or shorter time steps, helps in reducing the truncation error, but ultimately this approach relies on advances in computer technology. An alternative method, which does not require faster computing speeds, involves optimising the arrangement of the finite number of grid points that the modeller has at her disposal [Chassignet et al., 1996]. In Section 2.1.1, optimisation techniques based on altering the vertical coordinate are discussed. Section 2.1.2 discusses horizontal discretisation techniques, focusing on the C-grid discretisation implemented in HYCOM, and Section 2.1.3 briefly introduces the equations and integration algorithms used in HYCOM to model the ocean state. In Section 2.1.4, a summary is provided of the K profile parameterisation (KPP) mixing scheme implemented in the HYCOM runs of the current thesis.

2.1.1 Vertical Coordinates

The classical representation of the equations of motion in Cartesian x, y, z coordinates, where x, y are horizontal coordinates in the zonal and meridional directions, respectively, and z is the vertical coordinate opposing the Earth's gravitational pull (commonly adjusted to include the effect of the centrifugal force owing to the Earth's rotation), has been shown [see, e.g., McDougall and Church, 1986] to produce unstable numerical solutions in large-scale oceanic simulations, owing largely to an unphysical diffusion of the water mass characteristics that results from the use of z as the vertical coordinate in instances when the fluid is baroclinic.[2] The origin of this unrealistic mixing lies in the tendency of turbulent mixing in the stratified ocean to be oriented predominantly along isopycnals [Iselin, 1939], with isopycnal diffusivities typically up to seven orders of magnitude larger than diapycnal (i.e. across-isopycnal) diffusivities [McDougall and Church, 1986]. Thus, any attempt to represent the along- and across-isopycnal diffusivities with purely horizontal and vertical diffusion coefficients, respectively, is bound to induce spurious numerical mixing that departs from its naturally occurring direction and, in many cases, overshadows the physically realistic, diapycnal mixing processes [Chassignet et al., 1996].

The problem of numerical diffusion that arises from the use of depth as the vertical coordinate in stratified water with sloping isopycnals has been found [see Chassignet et al., 1996; McDougall and Church, 1986] to be effectively remedied by replacing the independent variable z with the potential density of the water ρ_{pot}. This coordinate transformation removes the numerically induced diapycnal transport, as all lateral movement (i.e., movement in the x, y direction) is confined to surfaces of constant potential density. Isopycnic coordinates are especially suitable

[2] In a baroclinic fluid, the density of the fluid depends on factors other than solely pressure, for instance temperature and salinity. The resulting lines of constant density intersect the lines of constant pressure at an angle, in contrast to a barotropic fluid, where the lines of constant density and pressure are parallel [e.g., Kundu et al., 2012, p. 178].

for modelling adiabatic fluid motion [e.g., Sun et al., 1999], and studies [e.g., Bleck et al., 1992] suggest that they provide good results also in realistic oceanic simulations where diabatic effects are taken into account. For example, internal water mass characteristics, such as the difference in buoyancy between water masses, are conserved in long-term model integrations owing to the low diapycnal diffusion that characterises the stratified open ocean, making isopycnic coordinates suitable also for climate modelling [Bleck and Smith, 1990; Chassignet et al., 2003]. Fairly significant drawbacks associated with isopycnic OGCMs arise as a result of thermobaric effects, that is, effects related to variations in sea-water compressibility with temperature and salinity [Sun et al., 1999]. The use of potential density as the vertical coordinate requires a reference density against which in-situ densities can be compared; it is, however, not possible to define a single, global reference density such that the potential density everywhere varies monotonically with depth. In fact, the use of an ill-defined reference density can cause isopycnals to overturn, obviously restricting their usefulness as a vertical coordinate [Sun et al., 1999]. The fact that the in-situ density may vary along surfaces of constant potential density may also give rise to numerical errors in pressure gradient, and, ultimately, a state of *thermobaric instability*, in which vertical truncation errors grow exponentially with time [Hallberg, 2005; Sun et al., 1999].

Terrain-following coordinates, often called sigma coordinates, were first introduced by Phillips [1957] to overcome problems associated with the computational treatment of mountains and other steep topographical features in numerical weather forecasting. Designed to ensure that the ground—or, in an oceanic context, the sea floor—always remains a coordinate surface, sigma coordinates have proven skilful in high-resolution coastal simulations, where accurate representations of the bottom boundary layer are of importance [Griffies et al., 2000]. A disadvantage related to the use of sigma coordinates, however, stems from the difficulties they induce in correctly calculating horizontal pressure gradient forces near steep topographical gradients [Griffies et al., 2009; Haney, 1991]. Examples of ocean models formulated in purely terrain-following coordinates include the Princeton Ocean Model (POM), the Regional Ocean Modeling System (ROMS), and the Bergen Ocean Model (BOM).

2.1.2 Horizontal Coordinates

HYCOM, similarly to the majority of isopycnic ocean models [Griffies et al., 2000], is horizontally discretised using the so-called Arakawa C-type staggered grid [Arakawa and Lamb, 1977, p. 181], in which horizontal momentum (u, v), and scalar (e.g., T, S) variables are all located on the grid-cell boundaries: pressure (p) and scalar values are located in the lower left corner of each grid cell (these locations are referred to as p-points), while the u and v variables are centred on the lower and left grid cell boundaries, respectively [Halliwell, 2004]. Grid points are indexed by i in the latitudinal (zonal) direction, and j in the longitudinal (meridional) direction. See Figure 2.1 for a sketch of the horizontal grid configuration.

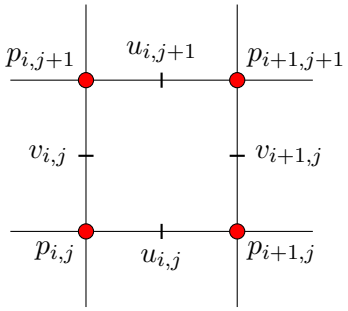

FIGURE 2.1: Sketch of the horizontal Arakawa C grid used by HYCOM. Momentum variables are stored in the u and v points, and scalar properties are stored in the pressure (p) points [Halliwell, 2004]. The i and j subscripts represent grid indices in the latitudinal (x) and longitudinal (y) directions, respectively.

The C grid has been found to provide accurate numerical results in simulations using fine (relative to the local deformation radius) horizontal resolution [Griffies et al., 2000], but the offset locations of the horizontal velocity components may cause unrealistic computational patterns in coarse-resolution simulations; these computational modes arise primarily because of the spatial averaging required to compute the Coriolis terms in the momentum equations [Adcroft et al., 1999]. Compared to alternative grid configurations—such as the Arakawa B grid (often used in z-level models), where u and v are colocated—the C grid, when applied to sufficiently high-resolution grids, is well suited for resolving large-scale gravity wave motions (such as inertio-gravity waves and boundary, or Kelvin, waves) and the energetics of baroclinic eddies [Griffies et al., 2000].

The spherical shape of the Earth renders a purely rectangular grid, such as that suggested by the schematic in Figure 2.1, unsuitable for global- and basin scale circulation models. Spherical coordinates are an intuitive alternative for modelling large-scale geophysical flows, but their practical implementation in OGCMs poses certain difficulties [Griffies et al., 2000]: first, a singularity necessarily exists at the North and South poles, and second, the convergence of the meridians near the poles leads to increasingly crowded grid cells, necessitating the use of excessively short time steps in order to satisfy the Courant–Friedrichs–Levy (CFL) condition of numerical stability.[3] These issues can be addressed with the use of generalised orthogonal curvilinear coordinate systems; the TOPAZ version of HYCOM, for example, implements a conformal mapping procedure developed by Bentsen et al. [1999], in which the poles are shifted to arbitrary locations (e.g., on land) in order to avoid singularities over water and to optimise the horizontal resolution in areas of interest [Sakov et al., 2012].

[3]The CFL condition constrains the time-step and grid cell lengths in the explicit numerical integration of certain partial differential equations. In mathematical terms, it states that the numerical domain of dependence should include the analytical domain of dependence of any particular equation. If the CFL condition is violated, the numerical scheme will lack the information needed to propagate the signals described by the equations correctly, leading to an uncontrolled growth of numerical instabilities [e.g., Press, 2007].

2.1.3 Equations and Time-Stepping Algorithms

The accurate modelling of a fluid dynamical system such as the ocean requires equations to represent the conservation of mass and momentum, as well as the laws of thermodynamics and an equation of state [e.g., Phillips, 1977, p. 8]. While the physics are accurately described by the full Navier-Stokes equations, large-scale numerical models representing the full ocean circulation often necessarily rely on certain simplifying assumptions. Traditional approximations for basin and planetary-scale fluid flows include the assumption of hydrostatic balance and the neglect of Coriolis terms involving the cosine of latitude [Marshall et al., 1997].

The HYCOM model equations [Bleck et al., 2002] are defined following the principles set forth by Bleck and Smith [1990] for the isopycnic ocean model MICOM. The isopycnic configuration approximates the ocean in terms of stacked, shallow-water layers of constant density that communicate with one another though hydrostatic pressure forces. In general spatial coordinates (x, y, s), with s representing an arbitrary vertical coordinate, the layer-integrated continuity (or mass conservation) equation for the layer mass per unit area, $\Delta p = p_b - p_t$, where the subscripts b and t refer to the bottom and top boundaries of an s-layer surface, is [Bleck et al., 2002]

$$\frac{\partial}{\partial t}_s \Delta p + \frac{\partial}{\partial x}_s (u\Delta p) + \frac{\partial}{\partial y}_s (v\Delta p) + \left(\dot{s}\frac{\partial p}{\partial s}\right)_b - \left(\dot{s}\frac{\partial p}{\partial s}\right)_t = 0. \tag{2.1}$$

Here, the subscript s implies keeping s constant, and $\dot{s} \equiv \frac{\mathrm{D}s}{\mathrm{D}t}$ is the vertical velocity in the direction of s [see, e.g., Vallis, 2006, p. 78]. The last two terms on the left-hand side of (2.1) stand for the mass fluxes across the top and bottom layer interfaces; these two terms regulate the spacing between the vertical layers, and are thus a central component of the hybrid coordinate algorithm. The HYCOM layer thickness is calculated at the end of each time step with the help of a *grid generator* module, which attempts to adjust modelled layer densities back to their reference densities by moving the density interfaces up or down, depending on the sign of the difference between the model density and the reference density; for example, if the layer has a lower density than the reference value, the lower interface is moved deeper such that the flux of denser water from below restores the reference density [Halliwell, 2004]. To prevent isopycnic layers from coalescing in weakly stratified regions, a minimum layer thickness is defined, with the result that near-surface layers that cannot be restored to their reference densities revert to z coordinates [Bleck et al., 2002].[4]

In addition to the multiple-layer continuity equation, the ocean dynamics in HYCOM are governed by a hydrostatic momentum equation for the horizontal velocity components, and an advection-diffusion equation for temperature (T) and salt (S). The thermodynamic variables T

[4]Technically, HYCOM uses the pressure, p, as the vertical coordinate instead of the geometric depth, z. In the current thesis however, the expressions are taken to be interchangeable, and the term z coordinates is used also when referring to the p coordinates of HYCOM.

and S, together with the pressure p, are also related to the potential density ρ_{pot} by a nonlinear equation of state based on the UNESCO formula [Brydon et al., 1999].

Motivated by the large differences in the characteristic time scales of internal (baroclinic) and external (barotropic, or depth-averaged) oceanic processes—the former of which may take years to reach equilibrium, while the latter processes generally adjust within a matter of days [e.g., Griffies et al., 2000]—it is customary in large-scale ocean models to decompose the model variables into slow "baroclinic" modes and fast "barotropic" modes [Higdon and de Szoeke, 1997]. The two modes are then resolved using different time step lengths, with shorter time steps used for the faster barotropic modes. In HYCOM, the baroclinic momentum equation is time-discretised using a leapfrog scheme with Asselin time-filtering, whereas the continuity and barotropic momentum equations are solved sequentially using a forward-backward time-splitting algorithm [Bleck et al., 2002].

2.1.4 The Vertical Mixing Scheme

A significant improvement provided by the hybrid-coordinate vertical grid of HYCOM over its predecessor MICOM, which is isopycnic at all vertical levels apart from a surface slab mixed layer, is that the transition from isopycnic to z-coordinates in the upper model levels enables the use of more complex mixing schemes, giving a more detailed and more realistic mixed layer structure [Bleck et al., 2002]. Whereas MICOM only supports a Kraus–Turner (KT) type slab mixing scheme [Gaspar, 1988; Kraus and Turner, 1967], where all oceanic properties are assumed to be perfectly mixed within the mixed layer, HYCOM is also equipped with the non-local K profile parameterisation (KPP) model of Large et al. [1994] and the second-order turbulent kinetic energy (TKE) closure models of Mellor and Yamada [1982] (MY) and the Goddard Institute for Space Studies (GISS) [Canuto et al., 2001], all three of which are able to provide a certain level of detail to the vertical structure of the mixed layer [e.g., Halliwell, 2004]. Although the KPP, MY, and GISS models have been found to produce qualitatively similar improvements over KT-type slab models in HYCOM [Halliwell, 2004], the current section will focus on describing the KPP scheme in more detail, as it is the one applied in the model runs performed in the present study.

The KPP vertical mixing scheme, developed by Large et al. [1994] on the basis of the principles of an atmospheric turbulence model formulated by Troen and Mahrt [1986], differs from traditional, two-equation TKE closure models [e.g., Kantha and Clayson, 1994; Mellor and Yamada, 1982], which employ a fully local, down-gradient closure assumption for the turbulent diffusion, in that the turbulent diffusivity K is allowed to be influenced by non-local effects. In practice, this non-local aspect means that K is a function of both the surface forcing and the mixing processes at the base of the boundary layer, and may at times operate up the local gradient

[Large et al., 1994]. The non-local influences may be formulated into the closure assumption of turbulent stresses as follows:

$$\overline{w'x'} = -K\Big(\frac{\partial X}{\partial z} - \gamma\Big). \tag{2.2}$$

Here, $\overline{w'x'}$ represents the vertical turbulent flux of any scalar or vectorial property $x = X + x'$, and γ is a non-local transport term related to large, coherent structures in the OBL. The non-local term in the original KPP formulation is set to zero in all but convectively unstable conditions (i.e., conditions where the surface buoyancy flux $B_f = -\alpha g H_0/(c_p\rho)$ is destabilising, that is, following HYCOM convention, $B_f > 0$),[5] and can only be non-zero for scalar properties; non-local momentum fluxes are not parameterised in the original KPP model owing to a lacking understanding of the behaviour of such processes [Large et al., 1994]. The turbulent fluxes, parameterised by (2.2), are used in KPP to model the time-evolution of mean model variables, X, with a one-dimensional vertical diffusion equation,

$$\frac{\partial X}{\partial t} = -\frac{\partial}{\partial z}\overline{w'x'}. \tag{2.3}$$

Following remarks made by O'Brien [1970], the turbulent diffusivity K in KPP is assigned a convex shape throughout the OBL (which spans the vertical range $0 < \sigma < 1$, where $\sigma = d/h_{bl}$; $d = -z$ and h_{bl} is the boundary-layer depth) by the following relation:

$$K(\sigma) = h_{bl} W(\sigma) G(\sigma). \tag{2.4}$$

In (2.4), $W(\sigma)$ is a turbulent vertical velocity scale and $G(\sigma)$ is a non-dimensional, convex shape function [see Figure 2 of Large et al., 1994, and, also, Figure 2.3]. The diffusivity profiles in the OBL are designed to smoothly match those of the interior ocean, where the diffusivity is assumed to be composed of a superposition of separate contributions by shear instability, overturning internal waves, and double diffusive processes; see Large et al. [1994] for further details on the interior mixing scheme, and the HYCOM user's manual [Bleck et al., 2002] for a thorough description of its implementation in HYCOM.

The KPP boundary-layer depth, h_{bl}, (not to be confused with the separately defined mixed-layer depth, h_{ml}) is defined as the depth d at which the bulk Richardson number,

[5] The surface buoyancy flux can be defined—neglecting the contributions of salinity, for simplicity—as a function of α, the coefficient of thermal expansion; g, the gravitational force; H_0, the surface heat flux, which is defined as positive into the ocean; c_p, the specific sea water heat capacity; and ρ, the water density [see, e.g., Pearson et al., 2015].

$$\mathrm{Ri}_b = \frac{(B_r - B)d}{(\mathbf{u}_r - \mathbf{u})^2 + W^2}, \tag{2.5}$$

surpasses a critical value, Ri_c.[6] In (2.5), $B = (\rho'/\rho_0)g$ is buoyancy, and the two terms from the left to the right in the denominator stand for resolved and unresolved shear, respectively. The subscript r denotes reference values averaged over the depth εd, where $\varepsilon = 0.1$. At $d = h_{bl}$, the averaging depth covers the so-called surface layer, in which Monin-Obukhov similarity theory (described in Section 2.2.4) applies, and fluxes are represented by dimensionless profiles derived empirically from atmospheric observations [Bleck et al., 2002; Large et al., 1994].

The turbulent velocity scale, W, represents unresolved vertical velocity fluctuations, and is generally defined in terms of dimensionless Monin-Obukhov similarity functions, Φ, as [Large et al., 1994; McWilliams and Sullivan, 2000]

$$W = \frac{\kappa u_*}{\Phi}, \tag{2.6}$$

where $\kappa = 0.4$ and u_* are the von Karman constant, a universal constant used for scaling wall-bounded turbulent flows, and the friction velocity, another general turbulent velocity scale commonly used for scaling constant-stress flows, respectively [e.g., Tennekes and Lumley, 1972, p. 54; see also Section 2.2.4]. The forms of the Monin-Obukhov stability functions, Φ, for scalars and momentum are given in Equation (3) of Large et al. [1994], and are defined such that W is enhanced in convectively unstable conditions ($\Phi \ll 1$) and reduced in stable conditions ($\Phi \gg 1$). Under destabilising forcing ($B_f > 0$), the magnitude of W inside the boundary layer is kept within 'reasonable' bounds (i.e., W is not allowed to grow beyond empirically sound values) by assuming that the $d = \varepsilon$ values apply for the entire boundary layer; no restrictions on W exist for stabilising forcing.

The convex shape function, G, is defined by [Large et al., 1994] as a third-order polynomial,

$$G(\sigma) = a_0 + a_1\sigma + a_2\sigma^2 + a_3\sigma^3, \tag{2.7}$$

in which a_0 is set to zero in order to inhibit turbulent transport across the sea surface, or $\sigma = 0$. The HYCOM version of KPP [Bleck et al., 2002] determines the remaining coefficients in (2.7) such that the K profile in the OBL transitions smoothly to the interior diffusivity below, all while keeping the requirements of Monin-Obukhov similarity theory fulfilled. The matching conditions connecting K and the interior diffusivity are provided in Equation (18) of Large et al. [1994].

[6] In HYCOM, the threshold is set to $\mathrm{Ri}_c = 0.3$ [Bleck et al., 2002].

The numerical algorithm of the KPP scheme is semi-implicit, requiring an iterative computational procedure for its implementation in HYCOM [Bleck et al., 2002]. The initial iteration involves forming vertical profiles of the diffusivity, K, using model variables computed at the previous time step. Since the vertical K profiles are constructed at p-points, the momentum variables u and v have to be interpolated horizontally to the p-points [Halliwell, 2004]. After the initial K profiles are formed, the model variables are mixed vertically by solving the one-dimensional diffusion equation (2.3) at each grid point using a tri-diagonal matrix system; the resulting, newly mixed variables are then used to form new K profiles. The above iterative procedure is repeated until the diffusivity profiles of two consecutive iterations differ by a negligible amount; testing conducted with HYCOM [Bleck et al., 2002] has shown that two iterations generally produces an optimal result when computational effort is taken into account. For further details on the numerical implementation of KPP in HYCOM, the reader is advised to consult the HYCOM user's manual [Bleck et al., 2002], and Halliwell [2004].

2.2 Langmuir Turbulence

The most marked dissimilarities in the dynamical properties between the ABL and the OBL can arguably be attributed to the ubiquitous presence of wind-generated surface gravity waves on the free interface that separates the two boundary layer regimes [Large et al., 1994; Sullivan and McWilliams, 2010]. Langmuir circulation is an example of a surface wave-induced, uniquely oceanic phenomenon that, together with other wave-related processes such as wave-breaking, distorts the motions in the upper layers of the ocean and thus modifies the well-known similarity profiles that have long been established for the ABL [Grant and Belcher, 2009; McWilliams et al., 2012, see also Section 2.2.4]. The seemingly orderly structure depicted in Figure 1.1 belies the inherent complexity of the dynamics that drive Langmuir circulation; current theory, pioneered by Craik and Leibovich [1976], ascribes its development to the interaction between the Stokes drift of irrotational surface waves and rotational surface currents, and the original mathematical representation entails a rather complicated phase-averaging procedure of the governing equations of motion.

The connection between the surface streaks, or windrows, that provide the surface signature of Langmuir circulation and the subsurface cellular structure (see Figure 1.1) was first made by Langmuir [1938], who discovered the motions following a series of experiments in a New York lake. Langmuir [1938] also realised that the process is wind-driven, and not, for instance, due to convective effects, but failed to appreciate the pivotal role of the surface waves and, especially, the Stokes drift associated with the waves. As a curious remark, Langmuir [1938] proposed Langmuir circulation as the primary mixing mechanism in the near-surface layers of oceans and

lakes; today, however, the process is recognised as one of several competing and complementary sources of mixing and transport in the OBL [e.g., Thorpe, 2004].

Addressing the modification of turbulence in the OBL by Langmuir cells adds another level of complexity to the picture. Starting with McWilliams et al. [1997], effort has been directed, chiefly by way of more or less idealised large-eddy simulation (LES) experiments, toward understanding and quantifying the effects of non-breaking wave-modified turbulence, or Langmuir turbulence, in the OBL. Building upon the analytical theory developed by Craik and Leibovich [1976] and LES results, subsequent years saw early explorations of the potential for improving large-scale ocean and climate model output by introducing enhanced OBL mixing by Langmuir turbulence into the turbulence schemes of the models; notable examples include McWilliams and Sullivan [2000], who developed the first parameterisation of Langmuir turbulence for the popular KPP mixing scheme, and Kantha and Clayson [2004], who were among the first to implement surface-wave effects in a two-equation Mellor and Yamada [1982]-type mixing scheme. More recently, Harcourt [2013, 2015] has continued the analytical development of second-moment turbulence closure models of Langmuir turbulence.

The current section will first introduce and discuss the 'laminar' Craik and Leibovich [1976] (CL) theory of Langmuir circulation and more recent developments thereof in Sections 2.2.1 and 2.2.2, before advancing into a review of the characteristics and scaling laws of Langmuir turbulence in Sections 2.2.3 and 2.2.4. The section will conclude with descriptions of the four parameterisations of Langmuir turbulence developed for KPP that are to be tested in the present study, in Section 2.2.5.

2.2.1 Craik-Leibovich Theory

The pursuit of a 'rational' theory of the dynamics of Langmuir circulation led Craik and Leibovich [1976] to derive a set of wave-averaged equations—the so-called Craik-Leibovich (CL) equations—describing the interaction between the wind-driven mean shear flow and the wave-induced Stokes drift, the properties of which are briefly introduced in the following.

The Stokes Drift

The Stokes drift is a residual particle drift in the direction of wave propagation, inherent in all propagating surface gravity waves [e.g., McIntyre, 1981]. Mathematically, the Stokes drift arises as a result of averaging the particle displacements in a wave field over several wave periods; to lowest order in wave steepness, $\epsilon = ka$, where k is the wavenumber and a is the wave amplitude, particles displaced by a passing wave follow closed, circular orbits, whereas the orbits to higher order in ϵ remain open, resulting in a net mass transport in the direction of wave propagation

[Kundu et al., 2012, pp. 284-285]. Despite being quadratic in amplitude, the Stokes drift is a property that emerges from linear theory, similar to other quadratic wave properties such as wave energy [Andrews and McIntyre, 1978b].

The physical mechanism behind the net drift is twofold: first, the positive correlation between the orbital particle motion and the motion of the wave crest itself on the crest of the wave leads to particles staying on the crests for longer than they stay in the troughs, where their orbital motion opposes that of the crests; second, linear wave kinematics dictate that the wave-induced vertical displacements are in phase with the vertical shear of the wave-induced horizontal velocities, leading to faster particle velocities on the wave crests than in the troughs [Ardhuin and Jenkins, 2006]. A peculiar quality of the Stokes drift is its strongly sheared vertical profile near the sea surface. The strong shear arises from the exponential decay of the wave orbital motions over the so-called Stokes depth, $\delta_S t = 1/(2k)$ [e.g., Rascle et al., 2006]. Because the Stokes drift is the residual velocity of the fast orbital motion of the waves, it is largely unaffected by turbulence, allowing its shear to persist even in conditions of strong mixing [Ardhuin et al., 2008b]. Moreover, the magnitude of the surface value of the Stokes drift is proportional to the third moment of the wave number spectrum of the surface waves, meaning that local wind seas—characterised by comparatively high wave numbers—generally contribute more to the surface drift than low-wave number swell of comparable significant wave height and peak period [Rascle et al., 2006].

The CL1 Mechanism

An important consequence of the phase-averaging procedure performed in Craik and Leibovich [1976] is the addition into the momentum equations of a Stokes drift-induced vortex force term that stretches and rotates the vorticity associated with the surface current shear from the cross-wind direction toward the along-wind direction, thereby creating the streamwise periodic cell structure that characterises Langmuir circulation. This approach, which relies on the assumption of a spanwise-periodic Stokes drift and a mean current that is weak compared to the wave-induced motion, is commonly referred to as the CL1 mechanism, following the terminology coined by Faller and Caponi [1978]. The CL1 theory was developed with the aim of satisfying a set of conditions based on the kinematic aspects of Langmuir circulation that were known at the time; that is, the theory was expected to predict a wind-driven system of parallel vortices aligned with the wind, with amplified downwelling speeds beneath surface convergence zones and weak upwelling regions in between [Craik and Leibovich, 1976].

In their original analysis, Craik and Leibovich [1976] assume that the sea surface in an unstratified ocean of infinite depth contains a discrete wave spectrum of small amplitude, a, waves with

wavenumber k and frequency ω. The three-dimensional velocity vector is expanded asymptotically as $\mathbf{u} = \epsilon\mathbf{u}_0 + \epsilon^2\mathbf{u}_{h.o.}$, where the lowest-order contribution is assumed to be due to the irrotational motion of the surface waves, such that the vorticity, $\boldsymbol{\omega} = \boldsymbol{\nabla} \times \mathbf{u} = \boldsymbol{\nabla} \times \mathbf{u}_{h.o.} \equiv \boldsymbol{\omega}_{h.o.}$; $\epsilon = ka$ is the spectral peak wave slope, which is assumed small in accordance with linear wave theory.[7] Vorticity is therefore confined only to the higher-order velocity fluctuations, $\mathbf{u}_{h.o.}$, and may be generated by sheared currents or any other perturbation, such as diffusion induced by wind stress [Leibovich, 1983]. The higher-order velocities are further expanded as $\mathbf{u}_{h.o.} = \mathbf{u}_1 + \epsilon\mathbf{u}_2 + \cdots$, with the resulting vorticity ordering $\boldsymbol{\omega}_{h.o.} = \boldsymbol{\omega}_1 + \epsilon\boldsymbol{\omega}_2 + \cdots$.

If the flow is separated into a time-mean and a fluctuating part, $\mathbf{u}_i = \overline{\mathbf{u}}_i + \mathbf{u}_i'$ (and correspondingly $\boldsymbol{\omega}_i = \overline{\boldsymbol{\omega}}_i + \boldsymbol{\omega}_i'$), where the mean velocity (overline) is steady in time and the fluctuating velocity (prime) is periodic, and if Coriolis effects are neglected and the eddy diffusivity, ν_t, is assumed constant, the following vorticity equation results from the perturbation expansion of the variables in the governing momentum equation [Craik and Leibovich, 1976, their Equation (9)]:

$$\boldsymbol{\nabla} \times (\overline{\mathbf{u}}_1 \times \overline{\boldsymbol{\omega}}_1) + \boldsymbol{\nabla} \times \overline{(\mathbf{u}_0 \times \boldsymbol{\omega}_2')} + \nu_t \boldsymbol{\nabla}^2 \overline{\boldsymbol{\omega}}_1 = 0. \tag{2.8}$$

Applying extensive tensor algebra, Craik and Leibovich [1976] show that the steady mean vorticity, after phase-averaging, follows the relation:

$$\nu_t \boldsymbol{\nabla}^2 \overline{\boldsymbol{\omega}}_1 = (\overline{\mathbf{u}}_1 + \mathbf{u}_s) \cdot \boldsymbol{\nabla} \overline{\boldsymbol{\omega}}_1 - (\overline{\boldsymbol{\omega}}_1 \cdot \boldsymbol{\nabla})(\overline{\mathbf{u}}_1 + \mathbf{u}_s). \tag{2.9}$$

The Stokes drift, $\mathbf{u}_s$, is defined in vector form as [e.g., Holm, 1996]

$$\mathbf{u}_s = \overline{\left(\int_0^t \mathbf{u}_0 \, \mathrm{d}t \right) \cdot \boldsymbol{\nabla} \mathbf{u}_0}, \tag{2.10}$$

and emerges from the evaluation of the phase average (denoted by the overline) in the $\boldsymbol{\nabla} \times \overline{(\mathbf{u}_0 \times \boldsymbol{\omega}_2')}$ term of (2.8). In the derivation of (2.9), a non-divergent Stokes drift velocity, $\boldsymbol{\nabla} \cdot \mathbf{u}_s = 0$, has been assumed. Considering a unidirectional Stokes drift in the x-direction, $\mathbf{u}_s = (U_S, 0, 0)$, neglecting variations in the x-direction, and rotating the coordinate system such that the x-axis is aligned with U_S, (2.9) with $\overline{\mathbf{u}}_1 = (u, v, w)$ and $\overline{\boldsymbol{\omega}}_1 = (\omega_x, \omega_y, \omega_z)$ simplifies to

$$\nu_t \nabla^2 \omega_x + \omega_y \frac{\partial U_S}{\partial y} + \omega_z \frac{\partial U_S}{\partial z} = v \frac{\partial \omega_x}{\partial y} + w \frac{\partial \omega_x}{\partial z}, \tag{2.11}$$

[7] In practice, the assumption of a small wave slope, and the consequent linearisation of the dynamics, implies that the nonlinear effects of advection take place on a time scale that is much longer than the period of the surface waves [e.g., Lane et al., 2007].

Equation (2.11) implies that the diffusion of x-vorticity and the deformation of spanwise (i.e., cross-wind) and vertical vorticity by the Stokes drift shear are balanced by the advection of streamwise (along-wind) x-vorticity. In order to obtain an alternating cell structure that is periodic in the y-direction, analogous to observed properties of Langmuir circulation, Craik and Leibovich [1976] impose a wave field consisting of "crossed" wave trains, meaning two dominant wave components of equal amplitude and horizontal wavenumber vectors (k, l) and $(k, -l)$, respectively. The crossed wave pattern produces a spanwise-periodic Stokes drift that attains a maximum where the interference between the two superposed waves creates a maximum surface displacement, and likewise a minimum where the interference creates a minimum surface displacement. By (2.11), these periodic variations in the Stokes drift deform the spanwise vortex lines associated with the vertical shear of the surface currents into streamwise-periodic Langmuir cells; see also Figure 2 of Leibovich [1983]. The generating mechanism of Langmuir circulation proposed by Craik and Leibovich [1976] and described above is known as the CL1 mechanism.

The assumption of steady motion in the analysis of Craik and Leibovich [1976] requires an ad hoc definition of the surface drift, which poses a restriction on the well-posedness of the problem [Leibovich, 1983]. Leibovich [1977b] extends the theory by introducing time-dependent surface currents, thereby producing a deterministic model that permits the time-evolution of the circulation under the assumption that the currents develop on a time scale that is long compared to the dominant surface wave period. Leibovich [1977b] also shows that the the governing momentum and vorticity balances can be written in terms of a dimensionless parameter which he calls the Langmuir number:

$$\mathrm{La} = \sqrt{\frac{\nu_t^3 k^2}{\omega a^2 u_*^2}}. \tag{2.12}$$

In a physical sense, La can be viewed as an inverse wave-controlled Reynolds number; it expresses a balance between streamwise vorticity diffusion and production by the deforming action of the Stokes drift [Leibovich, 1983]. The time-dependent model of Leibovich [1977b] also correctly predicts the logarithmic profile of the wind-induced surface drift reported by Wu [1975].

The CL2 Mechanism

The improvements to the original Craik and Leibovich [1976] paper discussed so far have neglected the most severe limitation of the CL1 model, that is, the idealised crossed wave train pattern that forms the basis of the model. As argued by Leibovich [1983], for such an orderly situation to arise the wave field would need to remain phase-locked for hundreds of wave periods. While this can be accomplished in a laboratory setting, as demonstrated by Faller and Caponi [1978], such patterns cannot be expected to form regularly in the open ocean. This would,

then, suggest that the theory is inadequate in reproducing the apparent ubiquity of Langmuir circulation in the ocean. In an effort to improve on the CL1 theory, Craik [1977] and Leibovich [1977a] propose an alternative mechanism based on an inviscid instability of the surface currents that is independent of the composition of the surface wave field; this theory is known as the CL2 mechanism.

Leibovich [1977a] shows that application of the wave-averaging procedure developed by Craik and Leibovich [1976] and Leibovich [1977b] on the stratified Boussinesq momentum equation with a constant eddy viscosity, ν_t, yields

$$\frac{\partial \mathbf{u}}{\partial t} + (\mathbf{u} \cdot \boldsymbol{\nabla})\mathbf{u} = \boldsymbol{\nabla}\pi + \mathbf{u}_s \times \boldsymbol{\omega} + \frac{\rho'}{\rho_0}\mathbf{g} + \nu_t \boldsymbol{\nabla}^2 \mathbf{u}, \tag{2.13}$$

where $\pi = p/\rho_0 + (1/2)[|\mathbf{u} + \mathbf{u}_s|^2 - |\mathbf{u}|^2]$ is pressure modified by the surface wave motion (also called a Bernoulli head), and $\mathbf{u}_s \times \boldsymbol{\omega}$ is a term known as the Craik-Leibovich (CL) *vortex force*. Rotational effects are readily incorporated with the inclusion of a Coriolis-Stokes term $\mathbf{f} \times (\mathbf{u} + \mathbf{u}_s)$, which describes an added veering of the currents due to the interaction between the Stokes drift and the vertical Coriolis vector $\mathbf{f}$ [Hasselmann, 1970; Weber, 1983]. Equation (2.13), with or without the Coriolis-Stokes term, will hereafter be referred to as the CL momentum equation.

To illustrate the instability mechanism proposed by Craik [1977] and Leibovich [1977a], Leibovich [1983] considers a unidirectional current, $\mathbf{u} = U(z,t)\mathbf{i}$, and a horizontally homogeneous wave field such that $\mathbf{u}_s = U_s(z)\mathbf{i}$. The vortex force, $\mathbf{f}_v$, in this configuration becomes

$$\mathbf{f}_v = U_s \frac{\partial U}{\partial z}\mathbf{k}. \tag{2.14}$$

The vertical unit vector, $\mathbf{k}$, implies that the vortex force acts vertically, analogously to a buoyancy force; in fact, fairly ordinary oceanic current and Stokes drift profiles are shown by Leibovich [1977a] to lead to a destabilising vortex force even in stably stratified water.

In contrast to the CL1 model, the variations in the Stokes drift need not be periodic in the CL2 model, which only requires an infinitesimal spanwise perturbation in the surface current for instability to arise. The vertical vorticity induced by the spanwise perturbation is tilted and stretched towards the horizontal by the vertical shear of the Stokes drift, thereby developing the helical cell structure that is characteristic of Langmuir circulation. The CL2 mechanism can also be explained in terms of the vortex force: the vertical vorticity produces a y-component of the vortex force that points towards the region of maximum current perturbation, causing the flow to accelerate into that region. Continuity requires the fluid to sink in the convergence zone, further amplifying the velocity perturbation and closing the feedback loop [Leibovich, 1983].

As remarked by McWilliams et al. [1997], the CL equations are the wave phase-averaged version of the full Navier-Stokes equations, where the impact of the surface waves enters through an imposed Stokes drift that is assumed given.[8] Also, any turbulence that may develop in the OBL is not allowed to influence the wave field in the classical CL theory; turbulence only acts as a dissipative source term through the constant eddy viscosity [McWilliams et al., 1997]. The more contemporary wave-turbulence interaction problem is discussed in more detail in Section 2.2.3.

It is important to recognise that the 'new' terms that enter the fluid motion equations in the CL theory—the vortex force and the Bernoulli head—are not ad hoc additions formulated to achieve a certain outcome, but emerge naturally as a consequence of the asymptotic, multiple-scale mathematical approximation developed by Craik and Leibovich [1976], Craik [1977], and Leibovich [1977a,b] in order to to separate the rapid motion and small-scale structure associated with surface waves from the slower, larger-scale current systems [see, e.g., Holm, 1996; Leibovich, 1980; Suzuki and Fox-Kemper, 2016]. Various alternative formulations of the wave–mean flow separation problem have been proposed. Garrett [1976] took a depth-integrated approach, expressing the interaction between waves and currents in terms of the wave radiation stress, a second-order property of linear waves that represents the momentum flux associated with the wave motion [Longuet-Higgins and Stewart, 1964]. This approach has been pursued further by Mellor [2003, 2008, 2016],[9] and Lane et al. [2007] have shown that it is conceptually equivalent to the vortex force formulation of Craik and Leibovich [1976].

2.2.2 The Generalised Lagrangian Mean

The purely Eulerian framework adopted in the theories described in Section 2.2.1 is cumbersome for fluid dynamical applications that involve, for instance, time-averaging of materially conserved quantities. To illustrate this point, Bühler [2014, p. 215] considers a general property, $\phi(\mathbf{x}, t)$, that is conserved following the true particle trajectories (i.e., in a Lagrangian reference frame); this can be expressed as

$$\frac{\mathrm{D}\phi}{\mathrm{D}t} = \left(\frac{\partial}{\partial t} + \mathbf{u}\cdot\boldsymbol{\nabla}\right)\phi = 0. \tag{2.15}$$

It is assumed that the usual assumptions of $\phi = \overline{\phi} + \phi'$ and $\mathbf{u} = \overline{\mathbf{u}} + \mathbf{u}'$—where overlines indicate Eulerian mean quantities and primes indicate disturbances with zero mean—apply. It is readily verified that taking an Eulerian average (e.g., averaging over a fast time scale

[8] In large-scale numerical simulations of the ocean circulation, for example, the value of the Stokes drift is usually calculated in a separate surface wave model.

[9] The Mellor [2003, 2008] papers incorrectly evaluated certain vertical wave-related fluxes, which limits the applicability of the theory derived therein to flat-bottomed domains; Ardhuin et al. [2008a] and Bennis et al. [2011] discuss the errors and propose corrections to the relevant equations.

such as a wave phase) of (2.15) results in a mean property, $\overline{\phi}$, that is not conserved along the Eulerian mean trajectories [see Bühler, 2014, Equation (10.2)]. To address this, the generalised Lagrangian mean (GLM) theory developed by Andrews and McIntyre [1978a] endeavours to define alternative, Lagrangian-mean properties, $\overline{\phi}^L$ and $\overline{\mathbf{u}}^L$, that satisfy

$$\left(\frac{\partial}{\partial t} + \overline{\mathbf{u}}^L \cdot \boldsymbol{\nabla}\right)\overline{\phi}^L = 0. \tag{2.16}$$

GLM is an exact theory, applicable to finite-amplitude wave-mean flow interaction problems, and has been shown [e.g., Ardhuin et al., 2008b; Bennis et al., 2011; Leibovich, 1980] to provide a useful framework for theoretical investigations of Langmuir circulation and turbulence; hence a brief introduction to the theory will be given in the present section.

The averaging operator used to arrive at the Lagrangian-mean variables in GLM theory is not a full, particle following Lagrangian mean—this would be near-impossible to implement in practice owing to the chaotic nature of fluid particle trajectories [Bühler, 2014, p. 216]—but, instead, an Eulerian mean of the variables evaluated at their displaced locations [e.g., Dingemans, 1997, p. 217]. With $\boldsymbol{\xi}(\mathbf{x}, t)$ denoting the displacements of the actual particle trajectories from the mean trajectories, the Lagrangian mean of the property ϕ is defined as

$$\overline{\phi}^L(\mathbf{x}, t) = \overline{\phi^\xi} = \overline{\phi(\mathbf{x} + \boldsymbol{\xi}(\mathbf{x}, t), t)}, \tag{2.17}$$

where the overlines denote Eulerian averages. In most applications to wave problems, the Eulerian averages in GLM theory are taken as time averages [Dingemans, 1997, p. 218]. See Figure 2.2 for a schematic of the concept of GLM.

The previous definition (2.17) makes it possible to define so-called Lagrangian disturbances, ϕ^ℓ, that, analogously to Eulerian disturbances, have a zero Eulerian mean [Bühler, 2014, p. 223]:

$$\phi^\ell(\mathbf{x}, t) = \phi^\xi(\mathbf{x}, t) - \overline{\phi}^L(\mathbf{x}, t). \tag{2.18}$$

If the general property ϕ is taken to be velocity, $\mathbf{u}$, then the disturbance velocity $\mathbf{u}^\ell$ can be stated in terms of the particle displacements as

$$\mathbf{u}^\ell = \overline{\mathrm{D}}^L \boldsymbol{\xi} \tag{2.19}$$

where $\overline{\mathrm{D}}^L = (\partial/\partial t + \overline{\mathbf{u}}^L \cdot \boldsymbol{\nabla})$ is the material derivative that applies to generalised Lagrangian-mean quantities [Andrews and McIntyre, 1978a, p. 616].

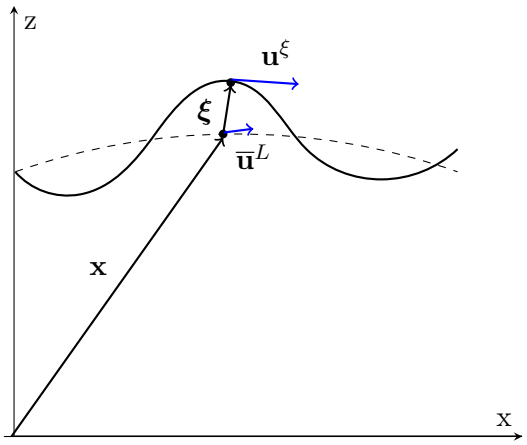

FIGURE 2.2: Two-dimensional schematic of the GLM concept, adapted from Figure (10.2) of Bühler [2014, p. 221]. The true fluid particle trajectory is shown by the solid curve, and the true particle velocity at the instantaneous particle location $\mathbf{x} + \boldsymbol{\xi}$ is denoted $\mathbf{u}^\xi$ (long blue arrow). The GLM velocity $\overline{\mathbf{u}}^L$ in the mean Lagrangian position $\mathbf{x}$ (obtained by time-averaging over the fast fluctuations) is indicated by the short blue arrow. The dashed line is the mean Lagrangian particle trajectory. If one conceptualises the dashed line as the mean Lagrangian sea level (e.g., the altitude measured by a floating, untethered buoy, and subsequently time-averaged), the Eulerian mean sea level would be slightly lower owing to the Stokes corrections of the sea-surface height that are absent from the Eulerian mean [Bühler, 2014, p. 218].

It is clear from the introduction provided above that the (hybrid) Lagrangian mean quantities as defined in the GLM theory differ from the Eulerian mean quantities; both are, however, evaluated at the fixed (Eulerian) locations $(\mathbf{x}, t)$. The difference between the two means is generally termed the Stokes correction, $\overline{\phi}^S$:

$$\overline{\phi}^S(\mathbf{x}, t) = \overline{\phi}^L(\mathbf{x}, t) - \overline{\phi}(\mathbf{x}, t). \tag{2.20}$$

In terms of velocities, $\overline{\mathbf{u}}^S = \overline{\mathbf{u}}^L - \overline{\mathbf{u}}$ represents the Stokes drift. Since GLM is an exact theory, an expression can be derived for the Stokes corrections to a desired order of accuracy, assuming small amplitude (a) displacements; Andrews and McIntyre [1978a] achieve this by first Taylor-expanding the fluid properties at the true particle positions, $\phi^\xi = \phi(\mathbf{x} + \boldsymbol{\xi}(\mathbf{x}, t), t)$, about the mean positions, $\mathbf{x}$. The resulting multivariable Taylor expansion, assuming that $\phi(\mathbf{x}, t) = \overline{\phi}(\mathbf{x}, t) + \phi'(\mathbf{x}, t)$ and $\boldsymbol{\xi} = \phi' = \mathcal{O}(a)$, is

$$\phi^\xi = \overline{\phi} + \phi' + \xi_j \frac{\partial \phi}{\partial x_j} + \frac{1}{2}\xi_j \xi_k \frac{\partial^2 \phi}{\partial x_j \partial x_k} + \mathcal{O}(a^3). \tag{2.21}$$

Here and henceforth, summation over repeated indices is implied [e.g., Aris, 1990]. Since $\overline{\phi}^S = \overline{\phi}^L - \overline{\phi} = \overline{\phi^\xi} - \overline{\phi}$, (2.21) may be averaged; recalling that $\overline{\boldsymbol{\xi}} = \overline{\phi'} = 0$, this gives [see Andrews and McIntyre, 1978a, their Equation (2.27)]

$$\overline{\phi}^S = \overline{\xi_j \frac{\partial \phi'}{\partial x_j}} + \frac{1}{2}\overline{\xi_j \xi_k}\frac{\partial^2 \overline{\phi}}{\partial x_j \partial x_k} + \mathcal{O}(a^3). \tag{2.22}$$

It is obvious that $\overline{\phi}^S = \mathcal{O}(a^2)$. The relation expressed by (2.22) for velocities u_j in place of the general quantity ϕ will be used later, in Section 2.2.3, in the derivation of the so-called Stokes shear production term in the turbulent kinetic energy (TKE) budget.

The GLM formalism gives rise to another wave-related property that is often confused with the Stokes drift, namely the *pseudomomentum* vector P_i which appears when transforming the momentum equations into GLM form [see, e.g. Dingemans, 1997, p. 221]. The pseudomomentum is the part of the total fluid momentum that is directly related to the wave motion, and can be approximated, for irrotational flow, as [e.g., Bühler, 2014, p. 220]

$$P_i = -\overline{\frac{\partial \xi_j}{\partial x_i} u'_j}. \tag{2.23}$$

Andrews and McIntyre [1978a, p. 631] show that, assuming that the mean flow is of second order in wave slope, $\epsilon = ka$, such that the flow is dominated by the wave motion, and the averaging operator is taken as a time-average, then P_i is approximated by $\overline{u}^S$ correct to $\mathcal{O}(\epsilon^3)$. This relation holds for special cases such as irrotational surface gravity waves and acoustic waves, but is not a generally applicable result [Andrews and McIntyre, 1978a, p. 632].

To show that the Craik-Leibovich (CL) momentum equation (2.13) is an Eulerian estimate of the exact flow predicted by the GLM theory, Leibovich [1980] derives the CL equation from the GLM version of the momentum equation originally derived in Andrews and McIntyre [1978a, see their equation (3.8)]. The exact GLM momentum equation for the mean flow in a constant density fluid reads

$$\overline{\mathrm{D}}_i^L(\overline{u}_i^L - P_i) + \frac{\partial \overline{u}_k^L}{\partial x_i}(\overline{u}_k^L - P_k) + 2(\boldsymbol{\Omega} \times \overline{\mathbf{u}}^L)_i + \frac{\partial \pi}{\partial x_i} = \nu_e \left[\overline{\nabla^2 u_i}^L + \overline{\frac{\partial \xi_j}{\partial x_i}(\nabla^2 u_j)^\ell} \right]. \tag{2.24}$$

Pressure forces are collected in the variable π [see Leibovich, 1980, for details], and the eddy viscosity, ν_e, is assumed constant. The rotation of the reference frame is symbolised by the angular velocity $\boldsymbol{\Omega}$. Most of the terms in (2.24) are recognisable to those who are familiar with the classical Navier-Stokes equations: the first term on the left-hand side expresses the material derivative following a fluid parcel advected with the GLM velocity $\overline{\mathbf{u}}^L$, the third term is the Coriolis force induced by a rotating reference frame, the fourth and last term on the left-hand side term is the pressure gradient force, and the right-hand side contains the viscous forces.

The second term on the left-hand side is unique to the GLM representation, and arises because the GLM transformation only conserves the fluid volume to first order in wave slope [pointed

out by Øyvind Breivik, personal communication; see also Ardhuin and Jenkins, 2006]. This is a consequence of the nonlinear nature of the GLM lifting map used to transform mean fluid particle positions to their true positions; spatial and temporal derivatives are, hence, not invariant under the GLM transformation [Bühler, 2014, p. 224]. The origin of the term is discussed in, for instance, Andrews and McIntyre [1978a, Appendix B] and Bühler [2014, p. 237], and Leibovich [1980] shows that it gives rise to the vortex force and Bernoulli head terms in the CL momentum equation (see below).

Under similar assumptions to those invoked by Craik and Leibovich [1976] in the derivation of the original CL equations, namely that the fluid flow is dominated by irrotational, small-amplitude wave motions with higher-order rotational contributions allowed, Leibovich [1980] shows that $(\overline{u}_i^L - P_i)$ can be replaced by the Eulerian mean velocity $\overline{u}_i$ to $\mathcal{O}(\epsilon^4)$ accuracy.[10] The assumption of a constant eddy viscosity also allows the viscous term to be asymptotically approximated purely in terms of the Laplacian of the mean Eulerian velocity [the details, again, are found in Leibovich, 1980]. With the aforementioned simplifications, the exact momentum equation (2.24) reduces to the CL momentum equation (2.13), in which only the Eulerian mean velocity and the Stokes drift are retained. While the GLM approach of Leibovich [1980] maintains a large number of simplifying assumptions, similarly to the original Craik and Leibovich [1976] analysis, the derivation is considerably more concise, as it avoids the multiple-scale perturbation expansions of the original calculations.

Recently, Suzuki and Fox-Kemper [2016] have revisited the various wave–current interaction theories that have been devised in order to explain Langmuir circulation. They assert that the traditional Craik-Leibovich representation using the vortex force, $\mathbf{u}_s \times \boldsymbol{\omega}$, diffuses the forces attributable to the mean Eulerian currents and the surface waves, thus complicating the analysis of the energetics of the flow. A more transparent formulation, Suzuki and Fox-Kemper [2016] argue, is the formally equivalent decomposition of the forces into a Lagrangian advection, $(\overline{\mathbf{u}}^L \cdot \boldsymbol{\nabla})\overline{\mathbf{u}}$ (which includes both the Eulerian advection and the Stokes advection), a Lagrangian Coriolis force, $\mathbf{f} \times \overline{\mathbf{u}}^L$, and a Stokes shear force, $\overline{u}_i^L \nabla \overline{u}_i^S$. The motivation for this reformulation is that the Stokes shear force is the force that transfers energy between the waves and the mean flow, whereas the advection and Coriolis terms do not transfer wave energy. Because the vertical shear of the Stokes drift typically dominates the horizontal shear in magnitude, it is found that the vertical Stokes shear force, $\overline{u}_i^L(\partial \overline{u}_i^S / \partial z)$, produces non-hydrostatic pressure perturbations on the flow that drive Langmuir circulation-like cells [see Suzuki and Fox-Kemper, 2016, their Figure 1].

[10] Recall that the pseudomomentum $\mathbf{P}$ is asymptotically equal to the Stokes drift $\overline{\mathbf{u}}^S$ in the case of irrotational, small-amplitude surface gravity waves.

2.2.3 Wave-Turbulence Interactions in the OBL

Given the paucity of accurate data and the arduous nature of acquiring measurements in rough seas [Sullivan and McWilliams, 2010], investigations of the modification of OBL turbulence by the presence of Langmuir circulation have historically relied heavily on large-eddy simulations (LES) of the CL equations that were derived in Sections 2.2.1 and 2.2.2. LES is a turbulence modelling technique that takes advantage of the multiple-scale aspect of turbulent flows by explicitly resolving the large, energy-containing scales that exhibit the largest flow-dependence, and parameterising the more predictable properties of the (approximately) isotropic small scales [Kantha and Clayson, 2000, p. 78]. In essence, the methodology of LES involves a low-pass filtering of the three-dimensional velocity field, resulting in a set of filtered equations that describe the evolution of the resolved velocities; the sub-grid scale, unresolved motions are represented by residual stress terms that must be approximated by other means [Pope, 2000, pp. 558-559]. Too computationally expensive to be practicable in realistic basin- or global-scale oceanic simulations, LES is nevertheless a valuable validation tool for evaluating the performance of more economical turbulence closure models, as well as a comparatively inexpensive alternative to the brute-force approach of direct numerical simulations (DNS) [Kantha and Clayson, 2000, p. 78].

In the high-Reynolds number environment of the global OBL, the 'laminar' Langmuir number, La, defined in (2.12) approaches zero, and the flow characteristics become dependent on another set of parameters. McWilliams et al. [1997] argue that relevant flow parameters in the wind-forced OBL are the water-side friction velocity, $u_* = (\tau/\rho)^{1/2}$, where τ is the wind stress applied on the ocean surface and ρ is the water density, and the surface value of the Stokes drift speed, $U_{S0} = a^2 k\omega$ [valid for monochromatic, deep-water waves; see, e.g., Kundu et al., 2012, p. 285]. These two variables are readily combined to form a dimensionless parameter that McWilliams et al. [1997] name the turbulent Langmuir number,

$$\mathrm{La}_t = \sqrt{\frac{u_*}{U_{S0}}}. \tag{2.25}$$

By construct, wind-induced shear production is expected to dominate the turbulence structure when $\mathrm{La}_t \gtrsim 1$, and when $\mathrm{La}_t \ll 1$, the deforming effect of the Stokes drift shear overshadows other production mechanisms. The latter OBL regime is known as Langmuir turbulence. A value of $\mathrm{La}_t \approx 0.3$ has been found [e.g., Belcher et al., 2012; McWilliams et al., 1997; Smith, 1992] to be representative of the global OBL structure [see also Thorpe, 2004].

Starting with a general form of the fluid momentum equation (e.g., (2.13), neglecting the wave-induced vortex force and pressure terms), an equation can be derived for the kinetic energy of turbulent fluctuations following the procedure demonstrated in, for example, Stull [1988, p. 151]. Assuming that the flow variables can be decomposed into mean and fluctuating parts

(e.g., $u = \overline{u} + u'$; i.e., the classical Reynolds decomposition [e.g., Tennekes and Lumley, 1972, p. 28]), the turbulent kinetic energy (TKE) per unit mass is $\overline{e} = 0.5\overline{(u'^2 + v'^2 + w'^2)}$, and the equation that describes its evolution can be written as

$$\underbrace{\frac{\partial \overline{e}}{\partial t}}_{\text{I}} = \underbrace{-\overline{\mathbf{u}_h' w'} \cdot \frac{\partial \overline{\mathbf{u}}_h}{\partial z}}_{\text{II}} + \underbrace{\overline{w'b'}}_{\text{III}} \underbrace{- \frac{\partial}{\partial z}\left(\frac{1}{2}\overline{w'e} + \frac{1}{\overline{\rho}}\overline{w'p'}\right)}_{\text{IV}} \underbrace{- \varepsilon}_{\text{V}} , \tag{2.26}$$

where $\mathbf{u}_h = \overline{\mathbf{u}}_h + \mathbf{u}_h'$ consists of the horizontal velocity components, $(u, v) = (\overline{u} + u', \overline{v} + v')$. In deriving (2.26), the common assumptions of a horizontally homogeneous, incompressible Boussinesq flow with negligible subsidence (i.e., $\overline{w} \approx 0$) have been made [see Stull, 1988, p. 86]. Term I, the Eulerian time-derivative of $\overline{e}$, represents the local time-evolution of the TKE. Term II quantifies the mechanical (e.g., wind stress-induced) shear production of TKE, that is, the extraction of TKE from the mean current by the turbulent (Reynolds) stresses; this term always constitutes a source of turbulent energy. The buoyant production, term III, can be either a source or a sink for the TKE, depending on the stability of the fluid's stratification. Term IV contains the vertical gradients of the vertical turbulent transport $0.5\overline{w'e}$ and the pressure covariance $\overline{\rho}^{-1}\overline{w'p'}$; these *flux divergences* act only to spatially redistribute TKE, and therefore constitute neither sources nor sinks of turbulent energy [Kantha and Clayson, 2000, p. 48]. The viscous dissipation of TKE is represented by Term V; this sink of TKE describes the work of viscous stresses on the fluctuating strain rate of the fluid; although the viscous processes take place on very small scales compared to the mean flow and the large turbulent eddies, the dissipation of TKE is an integral property of turbulent flows and can never be neglected [e.g., Kantha and Clayson, 2000, p. 49].

Non-breaking surface waves—the effects of which are neglected in (2.26)—distort oceanic turbulence by two mechanisms: directly through the orbital particle motions, and by the second-order effect of the vertical shear of the Stokes drift. The straining effect of the particle motions is weak and therefore often neglected, whereas the Stokes drift—while even weaker due to the second-order dependence on the wave slope—acts cumulatively, thereby becoming increasingly important with the passing of several wave periods [Teixeira and Belcher, 2002]. Based on LES results of Polton and Belcher [2007], the dynamical balance in the turbulent near-surface Stokes layer in the absence of breaking waves is found to be between the production and deformation of TKE by the Stokes drift and the dissipation of TKE, while deeper in the OBL the dissipation acts on the turbulent transport of TKE. The main mechanisms at work in Langmuir cell-forced turbulence are: *i*) the production of turbulence by the mean shear; *ii*) the deformation of turbulence by the Stokes drift; and *iii*) the blocking of turbulence by the air-sea interface [Teixeira and Belcher, 2010]. All these factors combined give Langmuir turbulence a distinctly different character from shear-driven turbulence (see Section 2.2.4), although evidence also exists of

purely surface stress-driven flows producing features, such as surface convergence streaks, that are usually attributed to the presence of Langmuir circulation [e.g., Tsai et al., 2005].

It is customary to model the contribution of non-breaking surface waves to the TKE budget (2.26) with the inclusion of a production term that represents the extraction of energy by the turbulent stresses from the vertical shear of the Stokes drift. First introduced in McWilliams et al. [1997]—who found it as a result of deriving a steady TKE budget from the CL momentum equation (2.13)—this so-called *Stokes production* term, P_{St}, has the form

$$P_{St} = \overline{\rho u' w'} \frac{\partial U_S}{\partial z}, \tag{2.27}$$

where ρ is the water density. According to McWilliams et al. [1997], the Stokes production term arises due to the wave-induced pressure (or Bernoulli head) term in the CL equation; the authors, however, omit crucial details of the derivation—details such as the manner in which they decompose the flow variables into mean, wave, and turbulent constituents—thus obfuscating the origin of the production term.

Teixeira and Belcher [2002] derive (2.27) in a wave-following Lagrangian framework, assuming a mean flow composed entirely of wave motions. They compare the growth rate of TKE suggested by the Stokes production term with the growth rate obtained from a rapid distortion theory (RDT) model of wave-turbulence interaction, finding that both estimates produce remarkably similar growth rates. They also find that most of the TKE associated with the wave motions is contained in streamwise vortices, as would be expected for turbulent flows distorted by coherent Langmuir cells.

An important assumption, invoked by both McWilliams et al. [1997] and Teixeira and Belcher [2002], is that the turbulent fluctuations are uncorrelated with the wave phase. This assumption is also central in the derivation of the Stokes production term using the Generalised Lagrangian Mean (GLM) theory carried out by Ardhuin and Jenkins [2006]. Separating the motion into mean flow, wave, and turbulent components—where the wave and mean flow motions are assumed to be of similar magnitude—and assuming no phase-coherence between the turbulence and waves, Ardhuin and Jenkins [2006] write

$$\overline{P}_S^L = \overline{\rho u_i' w_j'}^L \overline{\frac{\partial u_i}{\partial x_j}}^L, \tag{2.28}$$

where u_i contains both the wave and mean flow components of the velocity. It should be noted that the GLM average is taken of the entire shear term, not purely of the velocity. Focusing in the following on the wave component, $\widetilde{u}_i$, say, an expression will be sought, following Ardhuin

and Jenkins [2006], for the covariance between the turbulent stresses and the shear induced by the orbital particle motions of the surface waves.

To further simplify the problem, Ardhuin and Jenkins [2006] consider two-dimensional linear, monochromatic, and sinusoidal free-surface displacements, $\eta = a\cos(kx - \omega t)$, where a is the (small) wave amplitude, k is the wave number, and ω is the wave frequency, which follows the dispersion relation $\omega^2 = gk\tanh(kD)$. The gravitational force is denoted by g, and D is the water depth; the waves are taken to travel in the positive x direction, while oscillating orthogonally to the direction of propagation, parallel to the vertical z axis. The horizontal and vertical orbital velocity components ($\widetilde{u}$ and $\widetilde{w}$, respectively) induced by waves of such form are described by the well-known expressions [see, e.g., Phillips, 1977, p. 44]

$$\widetilde{u} = a\omega F_{cs}\cos(kx - \omega t), \tag{2.29a}$$

$$\widetilde{w} = a\omega F_{ss}\sin(kx - \omega t). \tag{2.29b}$$

Here, the symbols $F_{cs} = \cosh[k(z+D)]/\sinh(kD)$ and $F_{ss} = \sinh[k(z+D)]/\sinh(kD)$ represent the parts of the expressions that contain the z-dependence. Expressions (2.29a) and (2.29b) apply for water of arbitrary depth, that is, no deep or shallow-water approximations have been made at this stage. Expressions for the linearised, small-amplitude particle fluctuations can be obtained from (2.29) by time-integration [see, e.g., Kundu et al., 2012, pp. 260-262]:

$$\xi_1 = -aF_{cs}\sin(kx - \omega t), \tag{2.30a}$$

$$\xi_3 = aF_{ss}\cos(kx - \omega t). \tag{2.30b}$$

To lowest order in wave slope, the particle orbits are closed ellipses, with ξ_1 and ξ_3 defining the semi-major and the semi-minor axes, respectively [Kundu et al., 2012, p. 262].

Using the GLM definitions (2.20) and (2.22) together with the linear velocity components and displacements, and recalling that the Eulerian means (e.g., averages over one or several wave periods at a fixed location in space) of the harmonically oscillating orbital velocity components are zero, Ardhuin and Jenkins [2006] show (see also Appendix A) that the shear terms in (2.28) reduce to[11]

$$\overline{\frac{\partial\widetilde{u}}{\partial z}}^{L} = \overline{\frac{\partial\widetilde{w}}{\partial x}}^{L} = a^2k^2\omega F_{ss}F_{cs}. \tag{2.31}$$

[11] The expressions given by Ardhuin and Jenkins [2006]—their Equations (10) and (11)—include erroneous factors of 1/2; this has been corrected in (2.31). See Appendix A for the exact calculations.

In order to simplify the notation, the deep-water approximation—that is, the assumption that the water depth is large compared to a characteristic wavelength of the surface waves—will be made in the following. In the deep-water limit, where $kD \to \infty$, the hyperbolic expressions F_{ss} and F_{cs} can both be approximated as e^{kz} [e.g., Holthuijsen, 2010, p. 120], and the Stokes drift, $U_S \approx a^2 k \omega e^{2kz}$ [Kundu et al., 2012, p. 285]. It thus becomes apparent that the wave-induced shears in (2.31) each account for half of the vertical shear of the Stokes drift, that is

$$\overline{\frac{\partial \widetilde{u}}{\partial z}}^L + \overline{\frac{\partial \widetilde{w}}{\partial x}}^L \approx 2a^2 k^2 \omega e^{2kz} \approx \frac{\partial U_S}{\partial z}. \tag{2.32}$$

Under the assumption that mean wave-induced modulations of the turbulent stresses can be neglected (i.e., $\overline{u'w'}^L = \overline{u'w'}$), Ardhuin and Jenkins [2006] argue that the wave-turbulence covariance in (2.28) reduces to the form suggested by the Stokes production term (2.27), similarly to what was found by McWilliams et al. [1997] and Teixeira and Belcher [2002].

It may be noted that evaluating the shears of the Lagrangian-mean velocity components $\overline{\widetilde{u}}^L$ and $\overline{\widetilde{w}}^L$ instead of taking the GLM of the shears, as was done above, leads to a somewhat different result. For example, whereas $\overline{\partial \widetilde{w}/\partial x}^L$ is nonzero—owing to the fact that the wave crests correlate with a larger volume of water than the wave troughs [Ardhuin and Jenkins, 2006]—the horizontal gradient of $\overline{\widetilde{w}}^L$, $\partial \overline{\widetilde{w}}^L \big/ \partial x$, is, in fact, zero. This discrepancy stems from the fact that, as mentioned in Section 2.2.2, the GLM average does not commute with covariant differentiation due to the nonlinear nature of the lifting operation that is required to move analytically between mean and actual particle positions [Bühler, 2014, p. 224];.

With the addition of the Stokes production term (2.27) into the standard turbulent kinetic energy budget (2.26), the classical form of the wave-modified TKE budget, or, equivalently, the TKE budget for Langmuir turbulence, is obtained [see McWilliams et al., 1997]:

$$\frac{\partial \overline{e}}{\partial t} = -\overline{\mathbf{u}_h' w'} \cdot \frac{\partial \overline{\mathbf{u}}_h}{\partial z} - \overline{u'w'} \frac{\partial U_S}{\partial z} + \frac{\overline{w'\rho'}}{\overline{\rho}} g + \frac{\partial}{\partial z}\left(\frac{1}{2}\overline{w'e} + \frac{1}{\overline{\rho}}\overline{w'p'}\right) - \varepsilon. \tag{2.33}$$

Although often used specifically to model turbulence distorted by Langmuir circulations, the Stokes production term in (2.33) is not directly related to the Craik-Leibovich vortex force that drives the cellular motion in the wave-averaged CL momentum equations; as Ardhuin and Jenkins [2006] point out, the term appears as a consequence of the wave-induced modified pressure when the conservation equation for the TKE is derived from the CL equations. The Stokes production term should, perhaps, therefore be viewed in a more general sense as encompassing the aggregate contribution of the non-breaking wave-induced orbital particle motions to the turbulent kinetic energy of the flow [Kai Christensen, private communication].

The vertical shear of the Stokes drift plays an important role in several mixing parameterisations and turbulence closure models that strive to incorporate the effects of non-breaking surface waves and Langmuir circulations into schemes developed for rigid-wall atmospheric flows. In the non-local KPP scheme, for instance, it is customary [see McWilliams and Sullivan, 2000, and Section 2.2.5] to include Langmuir effects by modifying the turbulent diffusivities by factors formulated as power laws of La_t, a parameter which, in essence, quantifies the relative importance of wall-bounded shear production to Stokes shear production [Belcher et al., 2012, see also Section 2.2.4]. Kantha and Clayson [2004] include the Stokes production term in a two-equation, local turbulence closure scheme based on the Mellor and Yamada [1982] 2.5-level closure model, and find that its addition leads to increased upper-ocean homogeneity and mixed-layer deepening. In order to fully incorporate the Langmuir effects into second-order closure schemes, Harcourt [2013] modifes the algebraic stability functions arising from the closure assumptions to include explicit dependencies on the Stokes gradient. Harcourt [2015] further expands on the Reynolds stress models that form the basis of two-equation closure models by focusing on the wave-modified closure of the pressure-strain rate terms, which redistribute energy between the turbulent stresses [Pope, 2000, p. 389]. Finally, Suzuki and Fox-Kemper [2016] have shown, as partly discussed in Section 2.2.2, that the vertical Stokes shear force induces subsurface pressure perturbations that redistribute turbulent momentum fluxes according to the direction of the verticl Stokes shear. These non-hydrostatic effects are believed to force circulations well beyond the shallow e-folding depth of the Stokes drift.

2.2.4 Langmuir Turbulence in Stable Stratification

Turbulent flows are characterised by their wide, Reynolds number-dependent spectrum of spatial scales; the famed *energy cascade* theory holds that turbulent kinetic energy (TKE) is input at the large scales, from which it is transferred by processes that are independent of viscosity to smaller scales, before finally being dissipated by viscous forces on the so-called Kolmogorov microscales [Pope, 2000, p. 182]. Owing to this dependence of the small-scale viscous dissipation on the large-scale flow, estimates of the turbulent dissipation rate ε can be made by scaling the inviscid, large-scale turbulence characteristics [Tennekes and Lumley, 1972, p. 20].

The lack of consensus regarding the scaling of Langmuir turbulence is often suggested as a leading source of uncertainty in the validation of parameterisations of the process [e.g., Grant and Belcher, 2009]. Hence, several theories aimed to account for the modifications induced by non-breaking surface waves on the scaling of turbulent length and velocity scales in the OBL are described in the current section; a modified length scale—the so-called Langmuir stability length—will also be implemented in the KPP scheme in order to assess its impact on the mixing induced by the Langmuir turbulence parameterisations (see Section 4.1.4 for the results of the experiment). The current section begins with a short review of classical scaling laws of turbulent

flows in neutrally and stably stratified fluids, before discussing in more detail the characteristic length and velocity scales that have been proposed for Langmuir turbulence.

In conventional shear-driven, wall-bounded flows in which the Reynolds stresses are assumed constant, the mean horizontal velocity $\overline{u}$ is universally assumed to have a logarithmic profile, giving a mean shear of the form [e.g., Tennekes and Lumley, 1972, p. 54]

$$\frac{\partial \overline{u}}{\partial z} = \frac{u_*}{\kappa z}, \tag{2.34}$$

where $u_* = (\tau/\rho)^{1/2}$ is the water-side friction velocity, defined in terms of the wind stress τ and the water density ρ, and $\kappa = 0.4$ is the von Karman constant. The logarithmic $\overline{u}$-profile follows from the integration of (2.34). In steady-state conditions, without destabilising buoyancy fluxes, the conservation equation for turbulent kinetic energy (2.26) reduces to a balance between the shear production, the work done against the turbulence by the buoyancy flux, and the dissipation rate [Osborn, 1980]:

$$\overline{u'w'}\frac{\partial \overline{u}}{\partial z} - \frac{\overline{w'\rho'}}{\overline{\rho}}g = -\varepsilon. \tag{2.35}$$

Further assuming that the buoyant production is negligible compared to the shear production and rewriting the constant Reynolds stress in (2.35) in terms of the friction velocity, using $-\rho\overline{u'w'} = \rho u_*^2$ [Tennekes and Lumley, 1972, p.53], gives

$$\varepsilon = \frac{u_*^3}{\kappa z}. \tag{2.36}$$

The scaling suggested by (2.36)—the well-known *law of the wall*—applies for purely wall-bounded, unstratified shear flows such as those encountered in ocean-bottom boundary layers [Tennekes and Lumley, 1972, p.159], and although evidence supporting its applicability in the surface OBL and in near-surface layers of lakes has been reported [Churchill and Csanady, 1983; Richman et al., 1987; Thorpe et al., 2003], the more modern consensus [Craig and Banner, 1994; Gargett and Grosch, 2014; Grant and Belcher, 2009; Sutherland et al., 2013; Terray et al., 1996], supported by observations [D'Asaro, 2001], is that the scaling of the dissipation rate near the ocean surface is likely modified to some (relatively uncertain) degree by the presence of surface waves. The most marked departure from the law of the wall is often seen in the uppermost metres of the OBL, where breaking waves (whitecaps) directly inject turbulent kinetic energy into the ocean [Agrawal et al., 1992; Terray et al., 1996]. However, enhanced rates of TKE dissipation have been observed at depths well beyond the depth of penetration of whitecaps [e.g., Kitaigorodskii et al., 1983], pointing to the presence of additional surface wave-related processes, such as Langmuir circulations, influencing the profile of the TKE dissipation in the OBL. This

has led to attempts to define a velocity scale similar to u_* which could be used to scale the dissipation profile in the OBL outside of the direct influence of the surface breakers. Grant and Belcher [2009] argue that, provided the dominant large eddies in the OBL are due to Langmuir circulations (i.e., $\mathrm{La}_t \ll 1$, and negligible convection), the TKE production-dissipation balance of (2.36) can be stated in terms of a Langmuir velocity scale, w_{*L}, as $\varepsilon = w_{*L}^3/\lambda$, where λ is the large-eddy length scale.

The vortex force formalism of Craik and Leibovich [1976] and subsequent studies modifies (see Section 2.2.3) the *steady-state* TKE budget by adding a term to account for the extraction of TKE from the Stokes drift shear [see, e.g., Grant and Belcher, 2009; Polton and Belcher, 2007, and (2.33)]:

$$\overline{u'w'}\frac{\partial \overline{u}}{\partial z} + \overline{v'w'}\frac{\partial \overline{v}}{\partial z} + \overline{u'w'}\frac{\partial U_S}{\partial z} - \frac{\overline{w'\rho'}}{\overline{\rho}}g + \frac{\partial}{\partial z}\left(\overline{w'e} + \frac{1}{\rho}\overline{w'p'}\right) = -\varepsilon. \tag{2.37}$$

In contrast to (2.35), the cross-wind mean current, $\overline{v}$, has been retained in (2.37), as have the divergences of the turbulent energy and pressure work fluxes. The third term on the left-hand side is the Stokes production term, which represents the contribution of the orbital particle motion associated with non-breaking surface waves to the turbulent kinetic energy. Although the Stokes production of TKE directly forces the flow only down to a depth comparable to the e-folding depth of the Stokes drift, $\delta_{St} = 1/2k$, or $z/h_{ml} \approx -0.3$, the turbulent transport (i.e., the fifth term on the left-hand side of (2.37)) is believed to spread the enhanced dissipation over the entire mixed layer [Grant and Belcher, 2009]. Hence, Grant and Belcher [2009] argue that the dominant length scale for the large eddies in Langmuir turbulence should be the mixed layer depth, h_{ml}, instead of the Stokes depth, δ_{St} [see also Polton and Belcher, 2007]. They support their argument with idealised (no wave breaking, for instance) LES studies which show a dominance of Stokes production over shear production in the near-surface Stokes layer, and a marked decrease in the Stokes production below $z/h_{ml} \approx -0.3$ coincident with an elevated turbulent transport. It may be noted that in a recent study, Kukulka and Harcourt [2017] find that δ_{St} may, in fact, be the more relevant length scale in wind seas characterised by relatively short (i.e., higher-wavenumber) waves.

An early proposition for the form of the Langmuir velocity scale w_{*L} was given by Smith [1996], who used dimensional arguments and CL theory to arrive at the scaling relation

$$w_{*L} = (u_*^2 U_{S0})^{1/3}. \tag{2.38}$$

His underlying assumption was that the contribution of Langmuir circulation to the mixed layer momentum transport was constant over h_{ml}. The same scaling law was arrived at by Grant

and Belcher [2009], who assumed that the velocity covariance $\overline{u'w'}$ scales as u_*^2, whereas the average Stokes shear in the mixed layer, $\partial U_S/\partial z$, was assumed to scale as U_{S0}/h_{ml}, following from the arguments presented above. Using (2.38) and the characteristic length scale h_{ml} Grant and Belcher [2009] propose that the dissipation rate of Langmuir-dominated turbulence should scale as

$$\varepsilon = \frac{w_{*L}^3}{\lambda} = \frac{u_*^2 U_{S0}}{h_{ml}}. \tag{2.39}$$

When the Stokes production term of the TKE budget is approximated as in expression (2.39), an informative interpretation of the turbulent Langmuir number, $\mathrm{La}_t = (u_*/U_{S0})^{1/2}$, is revealed: its square is nothing but the ratio of the shear production to the Stokes production [Belcher et al., 2012].

The above discussion has neglected buoyancy fluxes entirely, focusing instead on the relation between the production of TKE by mechanical wind and wave forcing in unstratified waters. In conditions of significant stabilising buoyancy forcing, the relevant parameter quantifying the predominance of buoyant TKE suppression over shear production in the OBL is the Monin-Obukhov length scale L_{MO} [Large et al., 1994]:

$$L_{MO} = -\frac{u_*^3}{\kappa B_f}, \tag{2.40}$$

where B_f, as described in Section 2.1.4, is the surface buoyancy flux, defined (following HYCOM convention) such that $B_f < 0$ acts to stabilise the water column and thus suppress the production of TKE. Physically, $d = L_{MO}$ represents the depth below which the buoyant suppression is strong enough to inhibit the mechanical production of TKE by the mean shear, thereby effectively providing a limit to the boundary layer depth; following this reasoning, Large et al. [1994] restrict the KPP boundary layer depth h_{bl} to values lower in magnitude than L_{MO} in conditions of stabilising surface forcing. In neutrally stratified water, the limiting factor for h_{bl} in KPP is the Ekman layer depth $h_E = 0.7u_*/f$, where f is the Coriolis parameter.

The logarithmic velocity profiles found in neutrally stratified shear flows near solid boundaries are no longer strictly valid in stably stratified flows, which require somewhat more complex scaling laws. In the ABL, a set of scaling laws for turbulent flow variables known as Monin-Obukhov (MO) similarity theory [Monin and Obukhov, 1954] has been found [see, e.g., Foken, 2006] to approximate, to a reasonable degree of accuracy, scalar and wind gradient profiles in the constant-stress surface layer. The theory is formulated in terms of non-dimensional functions, with separate forms for scalar variables and momentum; the independent variable in the Monin-Obukhov similarity functions is the dimensionless stability parameter $\zeta = d/L_{MO}$ [see Equation (3) of Large et al., 1994, for the KPP version of the functions]. Atmospheric scientists routinely

use ζ to distinguish between wind stress-dominated ($\zeta \ll 1$) and buoyancy-dominated ($\zeta \gg 1$) boundary-layer regimes [e.g., Lombardo and Gregg, 1989].

While the Monin-Obukhov similarity scaling laws were empirically formulated based on atmospheric measurements, experiments have been reported [e.g., Lombardo and Gregg, 1989] that point to their applicability within the oceanic surface layer. However, many argue [e.g., Belcher et al., 2012; Noh and Jin Kim, 1999; Skyllingstad and Denbo, 1995; Sutherland et al., 2014] that the neglect of surface wave effects in the classical MO theory necessitates modifications in order for the theory to be properly applicable to the OBL. Analyses of the horizontal variability of La_t on global [Belcher et al., 2012] and regional scales [Gargett and Grosch, 2014] show that the value of La_t remains fairly constant over large spatial and temporal extents (see also Figure 3.1). In their global analysis, Belcher et al. [2012] find that the probability distribution of 10-year, spatially averaged values of La_t over Northern and Southern Hemisphere oceans peaks sharply at approximately $\mathrm{La}_t = 0.3$ and $\mathrm{La}_t = 0.35$, using wind and wave forcing from ERA-Interim [Dee et al., 2011] and ERA-40 reanalyses [Uppala et al., 2005], respectively.

The relatively constant global value of La_t in the range $0.3 < \mathrm{La}_t < 0.4$ reported by Belcher et al. [2012] suggests that the turbulence in the upper layers of the world oceans is consistently in a surface wave-controlled state. Since a value of $\mathrm{La}_t \ll 1$ implies a dominance of wave forcing over wind forcing in the OBL [McWilliams et al., 1997], an analogue to L_{MO} can be defined that weighs buoyancy-driven convective turbulence against wave-forced Langmuir turbulence; Belcher et al. [2012] consequently introduce the *Langmuir stability length*, L_{LT}, as

$$L_{LT} = -\frac{w_{*L}^3}{B_f}. \tag{2.41}$$

In contrast to L_{MO}, defined in (2.40), the definition of L_{LT} does not include the von Karman constant, which is a direct consequence of the law-of-the-wall scaling of the mean Eulerian shear, $\partial\overline{u}/\partial z$ (see (2.34)).

A dimensionless parameter, h_{ml}/L_{LT}, can be formed analogously to ζ such that $h_{ml}/L_{LT} < 1$ implies Langmuir or Stokes-dominated TKE production in the OBL, and $h_{ml}/L_{LT} > 1$ indicates that the TKE production is dominated by buoyancy [Belcher et al., 2012; Sutherland et al., 2014]. As noted by Sutherland et al. [2014], the Langmuir stability length can also be related to the Monin-Obukhov length as $L_{MO} = L_{LT}\mathrm{La}_t^{-2}$. Using this relation, and assuming a global value of La_t of ~ 0.3, Sutherland et al. [2014] define a cutoff for the transition between wave and convective domination as $|h_{ml}/L_{LT}| = 1$, inspired by Lombardo and Gregg [1989], who used $h_{ml}/L_{MO} = 10$ as a cutoff between wind- and convectively-forced turbulent regimes.

As mentioned above, the KPP mixing scheme limits the boundary-layer depth h_{bl} to values lower than L_{MO} when the surface buoyancy flux is stabilising, as in the case of surface heating

($H_0 > 0$ and, consequently, $B_f < 0$). Because large-scale ocean circulation models using KPP are known to induce warm sea-surface temperature (SST) and shallow mixed-layer (MLD) biases in simulations of summertime ocean states [Fan and Griffies, 2014; Li and Fox-Kemper, 2017; Li et al., 2016], an experiment will be conducted in the present study that replaces L_{MO} with L_{LT} in the KPP scheme. The motivation for the experiment is to assess whether the OBL mixing will be impacted by the surface wave-modified scaling of a central turbulence length scale; for more information about the experiment, see Chapter 3, and for the results, see Chapter 4 and, specifically, Figure 4.5.

2.2.5 Parameterisations of Langmuir Turbulence

The inclusion of the effects of non-breaking surface waves (specifically, the effects directly related to the Stokes drift) in large-scale ocean models, whose coarse numerical meshes inevitably prohibit resolving the small-scale wave motion, requires not only modifications of the subgrid-scale mixing schemes—the main focus of the current section—but also of the model conservation equations for momentum and scalars [van den Bremer and Breivik, 2017]. McWilliams and Restrepo [1999] were among the first to derive a set of wave-averaged, planetary geostrophic equations for the large-scale ocean circulation based on the Craik–Leibovich (CL) and generalised Lagrangian mean (GLM) theories described in Sections 2.2.1 and 2.2.2. The authors find that the proper inclusion of surface wave effects in the hydrostatic primitive equations of OGCMs requires the addition of the CL vortex force and the Stokes–Coriolis force of Hasselmann [1970], as well as a modified Stokes drift-induced tracer advection. If Langmuir turbulence effects are included in the mixing parameterisations, then these large-scale effects are readily incorporated in the model equations as they use the same wave-model input parameters (namely, the surface values of the horizontal Stokes drift velocities) as the turbulence schemes. In the following, descriptions will be provided of the four KPP Langmuir turbulence parameterisations that are tested in the numerical experiments of this thesis.

The McWilliams and Sullivan [2000] Parameterisation

In order to introduce the enhanced mixing effects of Langmuir turbulence—effects originally neglected by Large et al. [1994]—McWilliams and Sullivan [2000] propose a modification of the KPP mixing scheme based on LES studies of the OBL. The LES experiments of McWilliams and Sullivan [2000] are set up to integrate three-dimensionally discretised versions of the incompressible continuity equation, the CL momentum equation (2.13) (including both the Coriolis-Stokes and the vortex forces), and a scalar advection equation (with an added Stokes drift-induced advection term) in an open-ocean, deep-water domain in the mid-latitudes. The model is forced by a uniform wind stress and a monochromatic (i.e., single-wavenumber and single-frequency)

wave field. The wind and the waves are designed to be roughly in equilibrium; consequently, $\mathrm{La}_t = (u_*/U_{S0})^{1/2} \approx 0.3$ in all experiments. A weak, uniform heat loss is also imposed on the sea-surface, resulting in a weakly convective, chiefly wind and wave-forced OBL.

Citing observational evidence [e.g., Smith, 1999] and previous LES studies [Skyllingstad, 2000] suggesting that transverse (i.e., across-wind) velocities in fully developed Langmuir turbulence scale with U_S, McWilliams and Sullivan [2000] propose an enhancement of the unresolved turbulent velocity scale in the KPP scheme, W (see (2.6)), by an La_t-dependent factor, F_{LT}. Accordingly, W is modified as follows:

$$W = \frac{\kappa u_*}{\Phi} F_{LT}, \tag{2.42}$$

and the Langmuir enhancement factor, F_{LT}, is defined as

$$F_{LT} = \left[1 + \frac{C_w}{\mathrm{La}_t^{2\alpha}}\right]^{1/\alpha}. \tag{2.43}$$

The definition of F_{LT} in (2.43) includes two empirical constants, α and C_w, the former of which determines the form of W in the transition between shear-dominated ($\mathrm{La}_t \gtrsim 1$) and Langmuir-dominated ($\mathrm{La}_t \ll 1$) turbulent regimes. Lacking robust empirical evidence, McWilliams and Sullivan [2000] rather arbitrarily set $\alpha = 2$. The value of the second constant, C_w, is optimised by fitting profiles of the turbulent diffusivity, K, as defined in (2.4), of various flow variables to the LES results. An empirical value of $C_w = 0.08$ is found to optimally reproduce the modelled diffusivity profiles of the density field; this value has also been used in subsequent studies [Fan and Griffies, 2014; Li et al., 2016] that have incorporated the McWilliams and Sullivan [2000] parameterisation in large-scale ocean models.

An illustrative example of the enhancement of turbulent diffusivities in the OBL is provided in Figure 2.3. Using a typical [see Large et al., 1994; Troen and Mahrt, 1986] shape function of the form $G(\sigma) = \sigma(1-\sigma)^2$, and following McWilliams and Sullivan [2000] by setting $u_* = 0.0061$ m/s, $\Phi = 0.9$, $\mathrm{La}_t = 0.3$ (giving $F_{LT} = 3.3$), and assuming for simplicity that $h_{bl} = 1$, Figure 2.3 shows the characteristic convex shape of a standard KPP K profile (solid curve) and an enhanced K profile (dashed curve). Note that the diffusivities are normalised by $h_{bl}u_*$. A similar figure is shown by McWilliams and Sullivan [2000]; see, for instance, their Figure 6(c).

An inspection of the definition of the modified velocity scale (2.42) reveals that W approaches the original Large et al. [1994] definition (2.6) when Langmuir effects are expected to be weak; likewise, when $\mathrm{La}_t \ll 1$, indicating strong Langmuir forcing, W becomes proportional to U_{S0}. As emphasised by McWilliams and Sullivan [2000], however, (2.43) lacks an explicit stability dependency. This, combined with the fact that the LES experiments performed by McWilliams

and Sullivan [2000] only include weakly convective forcing, prompts the authors to caution that their proposed generalisation of the KPP model may not be applicable in a full range of realistic oceanic conditions without further modifications.

In a global, climatic-time scale investigation of the impact of parameterised Langmuir turbulence on OBL mixing, Fan and Griffies [2014] modified the KPP scheme of a coupled atmosphere-ocean-wave general circulation model (CM2M; developed at the National Oceanic and Atmospheric Administration, NOAA) according to the McWilliams and Sullivan [2000] proposition, finding that it induced abnormal mixed-layer deepening in winter months—especially in mid-latitude storm track regions—compared to a control simulation with no wave effects included. The impact on the mixed-layer depth (MLD) in the summer months, on the other hand, was minor when contrasted with the control experiment. Similarly, the modelled sea-surface temperature (SST) resulting from the McWilliams and Sullivan [2000] parameterisation exhibited an increased annual bias compared to the control, particularly in the Northern hemisphere. Fan and Griffies [2014] argue that these results suggest that the parameterisation exaggerates the wave-induced turbulent mixing in weakly stratified winter conditions, and underestimates the mixing in stably stratified summer conditions. Similar results were obtained by Li et al. [2016], who implemented and tested parameterisations of Langmuir turbulence in long-term integrations of the Community Earth System Model (CESM; developed at the National Center for Atmospheric Research, NCAR). The McWilliams and Sullivan [2000] parameterisation was shown to induce excess mixing, leading to increased root mean square errors (RMSE) of both summer and winter MLDs compared to a control run with no wave effects.

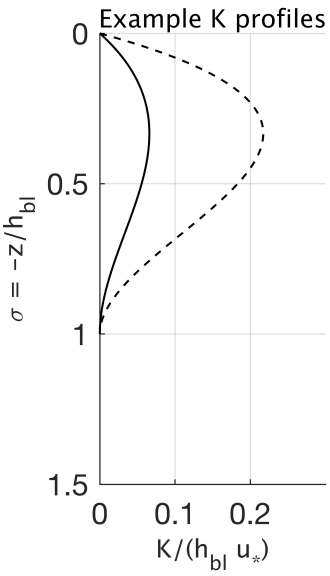

FIGURE 2.3: Standard KPP boundary-layer turbulent diffusivity (K) profile (solid) as a function of σ and normalised by $h_{bl}u_*$, following McWilliams and Sullivan [2000]. The dashed profile is K with W enhanced by $F_{LT} = 3.3$. See the text for more details.

The Smyth et al. [2002] Parameterisation

The lack of a direct dependence on stability parameters is often cited as the main limitation of the McWilliams and Sullivan [2000] parameterisation of Langmuir turbulence [see Fan and Griffies, 2014; Li et al., 2016; McWilliams and Sullivan, 2000]. Based on analyses of LES experiments and observational data of strongly stable (daytime warming) and strongly unstable (nocturnal cooling) forcing conditions in an equatorial setting, Smyth et al. [2002] address this

issue by extending the form of the KPP generalisation suggested by McWilliams and Sullivan [2000] to include a dependence on the convective velocity scale, $w_* = (\kappa B_f h_{bl})^{1/3}$, a common scaling of the RMS velocity fluctuations in convectively unstable turbulent boundary layers [Deardorff, 1970]. The proposed modification makes C_w—which was assigned a constant value of 0.08 in (2.43)—a function of w_* and the friction velocity, u_*, such that the Langmuir enhancement factor, F_{LT}, is reduced in destabilising surface forcing ($B_f > 0$) and enhanced in stabilising conditions ($B_f < 0$). The altered form of the turbulent velocity scale is

$$W = \frac{\kappa u_*}{\Phi}\left[1 + \frac{C_w(u_*, w_*)}{\mathrm{La}_t^4}\right]^{1/2}, \tag{2.44}$$

where

$$C_w = 0.15\left[\frac{u_*^3}{u_*^3 + 0.6w_*^3}\right]^2 \tag{2.45}$$

ensures that the enhancement is prevented from attaining unreasonably high levels in strongly convective conditions. Smyth et al. [2002] motivate the choice of the two constants in (2.45), 0.15 and the second power, by wishing to adhere to the results of McWilliams and Sullivan [2000] in weakly convective conditions, while simultaneously providing enhanced and reduced wave-induced mixing in strongly stable and in strongly unstable conditions, respectively, in accordance with their own LES experiments. The factor 0.6 in the denominator of (2.45) follows from a stability-dependent parameterisation of non-local momentum fluxes by Brown and Grant [1997].

Smyth et al. [2002] also propose a parameterisation for the non-local momentum fluxes that were neglected by Large et al. [1994] in the original KPP formulation because of inadequate empirical evidence. Comparing the vertical current profiles produced by the standard KPP scheme with their wave-forced LES results, Smyth et al. [2002] find that KPP overestimates the vertical shear of the currents in the mixed layer; the authors show that incorporating the vertical shear of the Stokes drift in a non-local momentum flux parameterisation based on the atmospheric model of Brown and Grant [1997] produces weaker-sheared current profiles more closely resembling the LES experiments. This additional momentum flux parameterisation has not been implemented in previous large-scale modelling studies to incorporate the Smyth et al. [2002] scheme, and is also neglected in the remainder of the present study.

The Harcourt and D'Asaro [2008] Parameterisation

Based on LES results obtained by Li et al. [2005], Harcourt and D'Asaro [2008] propose an alternative generalisation of KPP to accommodate for the effects of Langmuir turbulence. Retaining

the basic principle of (2.42), they graphically estimate an optimal fit to a plot [Figure 4 of Li et al., 2005] which depicts the modelled vertical turbulent velocity scaled by the friction velocity (a dimensionless measure of the turbulence intensity) against La_t. Harcourt and D'Asaro [2008] find that the best fit to the LES data is given by

$$W = \frac{\kappa u_*}{\Phi}\left[1 + \frac{0.098}{\mathrm{La}_t^2}\right]^{1/2}. \tag{2.46}$$

The LES experiments of Li et al. [2005], on which Harcourt and D'Asaro [2008] base their proposed Langmuir turbulence parameterisation, are relatively idealised in that they only include wind forcing and the vertical Stokes drift profile is exponential, corresponding to a monochromatic surface wave field. In comparison to McWilliams and Sullivan [2000], who included a weakly stabilising surface heat flux in their LES experiments, the Langmuir turbulence-induced enhancement of W proposed by (2.46) is evidently less sensitive to La_t than (2.42). To the author's knowledge, the Harcourt and D'Asaro [2008] parameterisation has not been tested in a realistic OGCM previously; however, results presented in Chapter 4 show that the low sensitivity of the Harcourt and D'Asaro [2008] parameterisation to the surface wave forcing (i.e., La_t) has a markedly more moderate effect on the turbulent mixing in the HYCOM model compared to the more sensitive parameterisations of McWilliams and Sullivan [2000] and Smyth et al. [2002].

Motivated by the lack of consensus regarding the scaling of turbulent velocity fluctuations in Langmuir turbulence, Harcourt and D'Asaro [2008] also perform LES experiments of their own, forced by more realistic wind and wave forcing than prior experiments. Instead of relying on the monochromatic surface wave field approximation implemented by the majority of prior LES studies [e.g., Li et al., 2005; McWilliams and Sullivan, 2000; McWilliams et al., 1997; Skyllingstad and Denbo, 1995; Smyth et al., 2002], Harcourt and D'Asaro [2008] use a wide range of 10-meter wind values to compute the horizontal surface stresses, and compute vertical Stokes drift profiles from empirical wave energy spectra, $F(\omega, \theta)$, where ω is wave frequency and θ represents the directional spread of the wave field. Harcourt and D'Asaro [2008] find that the turbulence forced by the spectral Stokes drift estimates is most accurately parameterised in terms of a modified Langmuir number, La_{SL}, in which a surface-layer (SL) vertical average of the Stokes drift is used instead of the more common surface value. Subsequent studies [e.g., Kukulka and Harcourt, 2017; Li and Fox-Kemper, 2017; Li et al., 2016; Van Roekel et al., 2012] have further investigated alternative La_t definitions in parameterisations of Langmuir turbulence; although their results indicate that implementing modified definitions of La_t in KPP may lead to improved mixed-layer properties, the current study will only implement the classical, surface Stokes drift-dependent definition (2.25).

The Takaya et al. [2010] Parameterisation

The critical parameter regulating the heat exchanges between the ocean and the atmosphere is the skin SST [e.g., Webster et al., 1996], defined as the temperature of the thin, diffusive sublayer in direct contact with the atmosphere, and observable by infrared radiometers sensitive to a specific range of wavelengths [Donlon et al., 2007]. The skin SST is known to exhibit large diurnal variability compared to bulk SST estimates obtained at larger depths. Since numerical models and several measurement techniques (e.g., moored buoys) typically give a bulk temperature value for the top several metres of the ocean, the diurnal variation of the skin SST must often be estimated by prognostic methods [Zeng and Beljaars, 2005].

Takaya et al. [2010] modify a prognostic skin SST scheme developed by Zeng and Beljaars [2005] to include a surface wave-dependence under stable (surface warming) forcing conditions, in which the standard scheme has been found to overestimate the surface temperature. Whereas the original scheme parameterised the thermal diffusivity K_T in terms of classical Monin-Obukhov similarity theory, the Takaya et al. [2010] modification adds an La_t-dependent enhancement factor to the diffusivity formula:

$$K_T = \frac{-\kappa u_* f(\mathrm{La}_t)}{\phi(\zeta)}. \tag{2.47}$$

The Langmuir enhancement function $f(\mathrm{La}_t)$ is defined as positive definite, and is chosen to follow the Langmuir turbulence velocity scaling of Grant and Belcher [2009] and Smith [1996] (see (2.38)):

$$f(\mathrm{La}_t) = \max(1, \mathrm{La}_t^{-2/3}). \tag{2.48}$$

Takaya et al. [2010] validate the modified K_T parameterisation by comparing integrations of a medium-range weather forecast model, in which the scheme has been implemented, with satellite and in-situ observations of the skin SST. The added impact of Langmuir turbulence (in terms of increased mixing) is found to improve the model's representation of the diurnal SST variability. The results support the observations of Li et al. [1995], who found that the daytime warming-induced restratification of shallow, diurnal mixed layers can be significantly delayed, and even entirely inhibited, by the presence of Langmuir circulations and turbulence.

Although not originally designed to parameterise Langmuir turbulence in the KPP mixing scheme, the K_T enhancement function of Takaya et al. [2010] given by (2.48) has been implemented in the HYCOM version of KPP in an equivalent manner to the previously described parameterisations, that is, as a multiplicative enhancement factor for the unresolved turbulent

vertical velocity, W. Similarly to the Harcourt and D'Asaro [2008] parameterisation, impacts resulting from incorporating the Takaya et al. [2010] parameterisation in large-scale ocean models have not been published previously.

Chapter 3

Methods and Dataset Descriptions

3.1 Experimental Setup

The numerical experiments are performed by running version 2.2.37 of HYCOM [Wallcraft et al., 2009] in the TOPAZ4 domain configuration, which covers the North Atlantic and Arctic Oceans with a mesh of 800 longitudinal and 880 latitudinal grid points. The horizontal resolution gives an effective grid size of 12-16 km, which means that the model is eddy-resolving in low to mid-latitudes, but not so in the Arctic owing to the small deformation radius in that region [Sakov et al., 2012].[1] The model domain is further divided into four focus regions that will be analysed in more detail. The focus regions are chosen to represent regions with distinct water mass characteristics, in order to assess the impact of the parameterisations in different geographical locations: Region A contains the Sargasso Sea (45–75°W, 20–30°N); Region B contains the western arm of the Gulf Stream (40–70°W, 35–50°N); Region C contains the Labrador and Irminger Seas (20–60°W, 52–60°N); and Region D contains the North and Norwegian Seas (15°E–15°W, 50–70°N).

Hybrid vertical coordinates are used in the model's 28 vertical layers, the top five of which are set to remain in z-coordinates at all times by assigning intentionally low reference densities to the five layers closest to the surface; TOPAZ4 convention [Sakov et al., 2012] is used for

[1] Analogously to atmospheric high and low pressure systems, the extratropical oceans are replete with baroclinic eddies with distinctive temperature and salinity characteristics. Markedly smaller in size compared to their atmospheric counterparts due to the comparatively high density of water, oceanic mesoscale eddies range in size from a few tens of kilometres in mid latitudes to less than 10 km in radius in polar regions [Chelton et al., 1998]. The characteristic length scale of these eddies is given by the first baroclinic Rossby deformation radius, a dynamical measure which largely depends on the water stratification and the latitude. In order to properly resolve the oceanic deformation radius, ocean models need a sufficiently high horizontal resolution; HYCOM's 1/12° resolution manages to resolve the structure of the larger eddies in lower latitudes, however, in higher latitudes, where the grid size is comparable to or even larger than the deformation radius, the model resolution is said to only permit, or in the latter case, prohibit, the representation of eddying structures [e.g., Hallberg, 2013].

TABLE 3.1: Reference density and coordinate type of each vertical model layer, following TOPAZ4 convention [Sakov et al., 2012]. The reference densities of the five layers closest to the surface are intentionally low in order to force those layers to remain in z-coordinates at all times. One thousand must be added to the reference densities to attain units of [kg/m^3].

Layer	Reference density	Vertical coordinate
1	0.1	z-level
2	0.2	z-level
3	0.3	z-level
4	0.4	z-level
5	0.5	z-level
6	24.05	isopycnic
7	24.96	isopycnic
8	25.68	isopycnic
9	26.05	isopycnic
10	26.30	isopycnic
11	26.60	isopycnic
12	26.83	isopycnic
13	27.03	isopycnic
14	27.20	isopycnic
15	27.33	isopycnic
16	27.46	isopycnic
17	27.55	isopycnic
18	27.66	isopycnic
19	27.74	isopycnic
20	27.82	isopycnic
21	27.90	isopycnic
22	27.97	isopycnic
23	28.01	isopycnic
24	28.04	isopycnic
25	28.07	isopycnic
26	28.09	isopycnic
27	28.11	isopycnic
28	28.13	isopycnic

the remaining layer reference densities. A list of reference densities per vertical level is provided in Table 3.1. Note that terrain-following sigma coordinates are excluded from the model configuration in the present thesis, also in accordance with standard TOPAZ4 convention.

Following initialisation from the World Ocean Atlas climatology [Antonov et al., 2006] and an initial spin-up simulation, each model run is started from the same restart file on the model date Jan 2, 2007 and integrated until Dec 30, 2008.[2] The model is allowed to evolve freely in response to the surface forcing, that is, no data assimilation is used to update the model variables at any stage. One control run is performed in which all surface wave forcing has been turned off (i.e., the standard HYCOM/TOPAZ4 setup), as well as four modified runs in which Langmuir turbulence effects have been parameterised in the KPP mixing scheme according to the McWilliams and

[2]The restart file was provided to the author by Dr. Jiping Xie at NERSC.

Sullivan [2000], Smyth et al. [2002], Harcourt and D'Asaro [2008], and Takaya et al. [2010] parameterisations. In addition to the KPP modifications, the four parameterised model runs also include the Coriolis-Stokes force, the CL vortex force, and a Stokes drift-induced tracer advection term in the model dynamics.

3.1.1 Modifications to the Standard KPP Code

The Langmuir turbulence parameterisations of McWilliams and Sullivan [2000], Smyth et al. [2002], Harcourt and D'Asaro [2008], and Takaya et al. [2010] have been added to the KPP code of HYCOM by developers at the Service Hydrographique et Ocanographique de la Marine (SHOM). The implementation is based on the La_t-dependent enhancement of the unresolved turbulent velocity scale W described in Section 2.2.5; modifications are made to the main KPP code *mxkprf.f*, and the parameterisations, as well as the Stokes-modified dynamics, are turned on with designated flags in the HYCOM configuration file *blkdat.input*.

The horizontal surface Stokes drift components u_{S0} and v_{S0} are read into the p points of the model grid from three-hourly forcing files (see Section 3.2.2) and used, together with the standard KPP friction velocity u_*, to calculate $\mathrm{La}_t = u_*/U_{S0}$, where the surface Stokes drift speed U_{S0} is defined as the magnitude $U_{S0} = (u_{S0}^2 + v_{S0}^2)^{1/2}$.

Two errors were found in the original SHOM formulation of the Smyth et al. [2002] parameterisation which produced overly intense mixing in early test runs: the convective velocity scale w_* had the wrong sign, and the definition of the enhancement factor included a maximum condition in the denominator which allowed for division by a very small number (included to prohibit division by zero) when w_* became negative. The aforementioned bugs were fixed by correcting the sign in the definition of $w_* = (\kappa B_f h_{bl})^{1/3}$ from negative to positive and restricting its range to values larger than or equal to zero, and by removing the maximum condition from the denominator of the Smyth et al. [2002] enhancement factor definition.[3]

The KPP code was modified further for the experiment in which the Monin-Obukhov length scale L_{MO} was replaced with the Langmuir stability length L_{LT}. In this case, the KPP variable $hmonob(i,j)$, which stands for L_{MO} and is used as an upper bound for h_{bl} under stabilising surface forcing conditions, was simply redefined to depend on the Langmuir velocity scale $w_{*L} = (u_*^2 U_{S0})^{1/3}$ instead of the traditional pure u_*-dependency. All fixes and modifications to the KPP code performed specifically for the present thesis are shown in Appendix B.

[3] The described fixes to the bugs in the KPP scheme were proposed by Dr. Alfatih Ali.

3.2 Forcing Datasets

The dynamical properties of the OBL exhibit a diurnal cycle forced by surface fluxes of heat and momentum, originating largely from solar heating, nighttime cooling and wind stress [Price et al., 1986]. The current section provides a brief description of the atmospheric and sea ice forcing applied on the ocean dynamics in HYCOM, as well as an introduction to the Wavewatch III surface wave model, which is the source of the wave forcing applied in the model runs.

3.2.1 Atmospheric and Sea Ice Forcing

Atmospheric forcing at the sea surface, including precipitation, cloud cover, and 10-m wind speeds [see Sakov et al., 2012, for more details], is applied using ERA-Interim reanalysis data [Dee et al., 2011] every 6 model hours. Produced by the European Centre for Medium-Range Weather Forecasts (ECMWF) using a 4D variational data assimilation scheme, ERA Interim is a continuously updated atmospheric reanalysis that currently extends from 1979 to present time, and is available for free download on the ECMWF website. The implementation of the atmospheric forcing in TOPAZ4 follows standard HYCOM procedure.

Sea ice is modelled by a coupled singular-thickness, elastic-viscous sea ice model [Hunke and Dukowicz, 1997], in which the thermodynamics follow the Drange and Simonsen [1996] formulation of air-sea fluxes over the open ocean and sea ice [see also Sakov et al., 2012].

3.2.2 Surface Wave Forcing

In the present model configuration, the forcing by wind-generated surface waves is represented by a single parameter, the Stokes drift, which is applied as a forcing variable every three model hours, and acquired offline[4] from an IFREMER hindcast [Rascle and Ardhuin, 2013] produced using a dedicated global wave prediction model called Wavewatch III (hereinafter WW3) [Tolman et al., 2009]. Developed at the National Oceanic and Atmospheric Administration (NOAA), WW3 is a third-generation wave model used in real-time operational wave forecasts at NOAA and IFREMER alongside other institutions. The horizontal resolution of WW3 is 0.5°; this has been interpolated to the 1/12° grid of TOPAZ4. In addition, the wave parameters are only available up to 80°N, hence HYCOM model output from areas further north has been masked out in all analyses of the results in Chapter 4.

In WW3, as in the majority of modern wave models, the surface wave field is assumed to consist of a superposition of weakly interacting wave components, each with its own distinct frequency, wavenumber and direction; thus, the wave energy is conveniently represented in

[4]The wave forcing has been downloaded and compiled into HYCOM forcing files by Dr. Alfatih Ali at NERSC.

spectral form, and linear wave theory is assumed to hold locally for individual components of the energy (technically the amplitude variance) density spectrum $F(k,\theta)$, where $\mathbf{k} = \mathbf{k}(\mathbf{x},t)$ is the wavenumber vector and θ is the direction [Tolman et al., 2009].[5] The total wave energy is obtained by integrating F over all wavenumbers and directions; however, since wave energy is not conserved when currents coexist with waves on the ocean surface [Bretherton and Garrett, 1968], instead of computing the evolution of the energy, WW3 solves for a conserved quantity known as the action density spectrum $N(k,\theta) = F(k,\theta)/\omega$ with the conservation equation [Tolman et al., 2009]

$$\frac{\mathrm{D}N}{\mathrm{D}t} \equiv \left\{ \frac{\partial}{\partial t} + \boldsymbol{\nabla}_x \cdot (\mathbf{c}_g + \overline{\mathbf{u}}) + \frac{\partial}{\partial k}\dot{k} + \frac{\partial}{\partial \theta}\dot{\theta} \right\} N = \frac{S}{\omega}, \tag{3.1}$$

where

$$\dot{k} = -\frac{\partial \omega}{\partial D}\frac{\partial D}{\partial s} - \mathbf{k} \cdot \frac{\partial \overline{\mathbf{u}}}{\partial s}, \tag{3.2a}$$

$$\dot{\theta} = -\frac{1}{k}\left[\frac{\partial \omega}{\partial D}\frac{\partial D}{\partial m} - \mathbf{k} \cdot \frac{\partial \overline{\mathbf{u}}}{\partial m} \right]. \tag{3.2b}$$

In the above expressions, bold notation indicates vectorial quantities, D is the water depth, and s and m are mutually perpendicular directional coordinates. The wave group velocity vector is given by $\mathbf{c}_g$ and the mean surface current is denoted $\overline{\mathbf{u}}$. The conservation equation (3.1) describes the slow-time scale evolution of the energy spectrum in water of variable depth, including wave refraction effects due to currents (expressions (3.2a) and (3.2b)) [Komen et al., 1994, p. 47].

In (3.1), S stands for nonconservative source terms that impact the evolution of the energy density spectrum F; these source functions generally include parameterisations of the wave growth induced by the winds, wave dissipation (mainly through wave breaking), and nonlinear wave-wave interactions that transfer energy between wave components. Wave model generations are differentiated based largely on their treatment of the nonlinear term: in first-generation models this term was neglected and the waves were assumed fully independent, whereas second-generation models used simplified theoretical spectra to crudely approximate the wave-wave interactions. In modern, third-generation models, the nonlinear source term is parameterised using empirical reasoning, removing the need for a priori assumptions [e.g., Tolman et al., 2002].

[5] Under the linear assumption, the wavenumber k and the intrinsic (i.e., observed in a reference frame moving with any existing mean current) frequency ω are related through the dispersion relation $\omega^2 = gk \tanh kD$, where g is gravity and D is the water depth. This allows the frequency-wavenumber-direction spectrum to be reduced to a two-dimensional wavenumber-direction, or alternatively, frequency-direction spectrum [e.g., Holthuijsen, 2010, p. 50].

The variable of interest in the present thesis, the surface value of the wave-induced Stokes drift U_{S0}, is estimated in the Rascle and Ardhuin [2013] hindcast in terms of the wave energy spectrum as

$$U_{S0} = \left| \int_0^{2\pi} \int_0^{0.72\text{Hz}} 4\pi f k(\cos\theta, \sin\theta) F(f,\theta)\, \mathrm{d}f\, \mathrm{d}\theta \right|, \tag{3.3}$$

where $f = \omega/(2\pi)$ is the ordinary wave frequency. The cutoff frequency of 0.72 Hz is required for the computational solution of the integral, and might, according to Rascle et al. [2008], lead to an underestimation of the true magnitude of the surface drift by the neglect of the highest-frequency wave components.[6] The magnitude of the wavenumber, $|k(\cos\theta, \sin\theta)|$, is proportional to f^2 by the deep water linear dispersion relation $\omega^2 = gk$, giving the integrand a high, $\mathcal{O}(f^3)$, sensitivity to frequencies approaching the cutoff limit.

The WW3 hindcast of Rascle and Ardhuin [2013] is forced by operational ECMWF Integrated Forecast System wind forcing, which is a distinct product from the ERA-Interim reanalysis employed to force the ocean model in the present thesis. As explained in Section 2.2.3, an informative measure of the sea state in wind and surface wave-forced conditions is the ratio of the wind-induced friction velocity to the wave-induced surface Stokes drift expressed by the turbulent Langmuir number $\mathrm{La}_t = (u_*/U_{S0})^{1/2}$ [see also, e.g., McWilliams et al., 1997]; maps of the the seasonally averaged values of La_t are given in Figure 3.1 to provide a visual overview of the wind and wave forcing. The figure shows that the winter season, especially, is clearly separated into two regimes: one, encompassing large parts of the open ocean, in which $\mathrm{La}_t \approx 0.3$ (a Langmuir turbulence-dominated regime), and another in which $\mathrm{La}_t \gg 1$ (wind-forced and convective regimes).

3.3 Model Validation

The output from the HYCOM model runs is compared to a number of empirically based datasets, which are briefly introduced in the current section. The analysed quantities are the mixed-layer depth (MLD), the sea-surface temperature (SST), and vertical profiles of ocean temperatures, and the datasets selected to validate these fields are, respectively, the IFREMER MLD climatology [de Boyer Montégut et al., 2004], the OSTIA SST reanalysis produced at the National Centre for Ocean Forecasting (NCOF) [Donlon et al., 2012], and the EN4 observational dataset of vertical temperature profiles [Good et al., 2013]. In addition to the descriptions of the

[6] In fact, Breivik et al. [2014] estimate that the unresolved, high-frequency spectral tail generally accounts for roughly 30% of the surface Stokes drift speed. For this reason, it is customary to parameterise the high-frequency contributions to the spectrum. Rascle and Ardhuin [2013], however, make no mention of adding a parameterised spectral tail to their estimate (3.3).

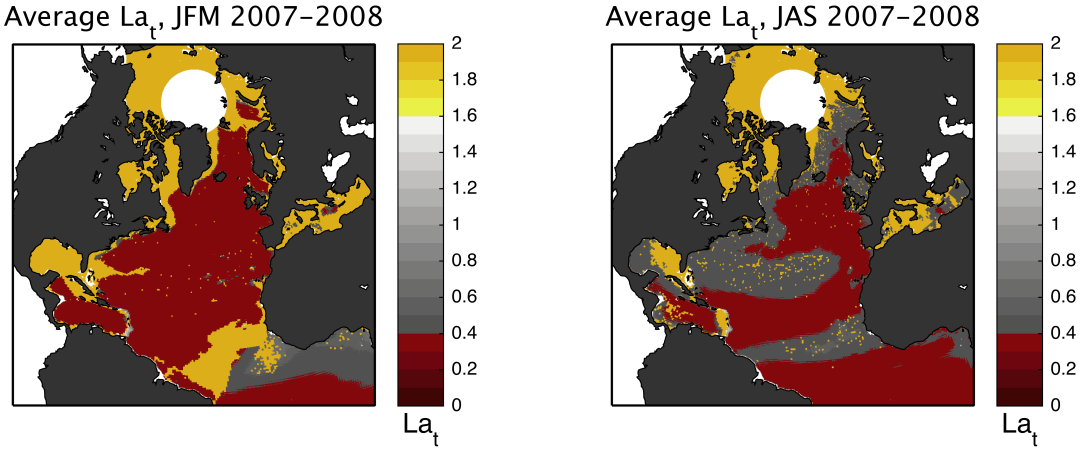

(a) (b)

FIGURE 3.1: Time-averaged turbulent Langmuir number, $\mathrm{La}_t = (u_*/U_{S0})^{1/2}$, where u_* is calculated from the ERA-Interim wind forcing, and U_{S0} is obtained from the WW3 hindcast. (a) shows the average over January-February-March (JFM) of 2007-2008; (b) shows July-August-September (JAS) 2007-2008. Low values of La_t (red) indicate significant modifications of the OBL turbulence structure by the presence of Langmuir circulation cells [Belcher et al., 2012; McWilliams et al., 1997]. Yellow colouring represents regions where $\mathrm{La}_t \gtrsim 2$, indicating negligible Langmuir forcing. Note the rather abrupt transitions between red and yellow colouring in winter months, suggesting that values of either $0.3 < \mathrm{La}_t < 0.4$ or $\mathrm{La}_t \gg 1$ consistently apply for large parts of the model domain.

observational data, the current section will provide descriptions of the main statistical methods used in Chapter 4 to compare the model runs to the aforementioned datasets.

3.3.1 Observational Datasets

Modelled MLD is compared with a gridded global climatology covering the 1961–2008 period, produced at IFREMER following the methodology of de Boyer Montégut et al. [2004]. In the climatology, the MLD is defined as the depth at which the water density surpasses 0.03 kg/m^3 of its reference value at a depth of 10 m. To reproduce this density criterion in the model output, the modelled MLD is computed, using daily averages, by linearly interpolating between the depth of the vertical model layer at which the 0.03 kg/m^3 threshold is exceeded and the depth of the layer above that. Further, the direct comparison between the climatology and the model fields requires a horizontal interpolation of the climatology's 2° grid onto the 1/12° grid of HYCOM.

Modelled sea-surface temperatures (SST) from the five model runs are compared against the 1/20°-resolution National Centre for Ocean Forecasting (NCOF) OSTIA gridded SST reanalysis dataset [Donlon et al., 2012] interpolated onto the TOPAZ4 model grid. The OSTIA dataset is composed of both satellite and in-situ data, and the daily reanalyses are currently used in operational forecasts at the European Centre for Medium-range Weather Forecasting (ECMWF).

2007-2008 January-February-March (JFM) and July-August-September (JAS) means of both OSTIA and model SST fields are calculated from daily average files; on certain days for which OSTIA data were unavailable, the preceding days' OSTIA data were used twice in forming the seasonal averages. The model SST is taken as the temperature of the uppermost model layer, which is 3 m thick.

EN4 [Good et al., 2013] is an oceanic dataset that consists of observed vertical profiles of temperature and salinity starting from the year 1900. The quality-controlled dataset is composed of oceanic profiling data from a variety of sources, including Argo floats, ocean stations, CTD casts, moored and drifting buoys, and gliders. The EN4 dataset is largely based on data included in the World Ocean Database [Levitus et al., 2013]; other sources include the Arctic Synoptic Basin Wide Oceanography project (ASBO) and the Global Temperature and Salinity Profile Program (GTSPP). In the current thesis, only data corresponding to the highest quality flag is used.

No temporal averaging has been performed on the EN4 data, although the instantaneous profiling data is provided in aggregate monthly NetCDF files. The validation of the vertical profiles is performed by directly comparing the EN4 profile data with daily-mean model fields of temperature, spatially interpolated to the observation locations. Because the model variables (below the uppermost few layers) are expressed in isopycnic coordinates, while the observed profiles are given in z-coordinates, the model variables have to be vertically interpolated to the depths of the observations. The vertical interpolation is performed following the procedure outlined in Wang et al. [2017]. In addition to vertical interpolation, model variables are horizontally interpolated to the longitude, latitude points of the observed profiles using a bilinear interpolation procedure, described in Appendix C.

3.3.2 Statistical Analysis

Student's t Test

To determine whether implementing the parameterisations of Langmuir turbulence in KPP has a noticeable effect on the modelled SST fields, the statistical significance of the differences between the mean SSTs induced by the control run and the parameterised model runs is analysed using a statistical method called the paired-sample Student's t test (hereinafter only t test). In practice, the t test is performed individually on each grid cell within each focus region. The test, therefore, gives an indication of the local significance of the differences, analysed over time.

An underlying assumption in a paired-sample t test is that the variance in two samples (in the present case, the seasonal time series of daily-average SSTs in a specific grid cell in the control run and in one of the wave-forced runs) is largely due to identical forcing [Press, 2007, p. 729].

Since the model runs in the current thesis are performed with identical atmospheric forcing, this assumption is considered valid. The test variable t is defined in terms of the standard errors S_D of the two samples [see Press, 2007, p. 727],

$$t = \frac{\overline{M}^c - \overline{M}^p}{S_D}, \tag{3.4}$$

where S_D is written in terms of the variance (Var) and covariance (Cov) as

$$S_D = \sqrt{\frac{\mathrm{Var}(M^c) + \mathrm{Var}(M^p) - 2\mathrm{Cov}(M^c, M^p)}{N}}, \tag{3.5}$$

and M stands for the modelled SST (with M^c symbolising the control run and M^p symbolising any of the model runs in which Langmuir effects are parameterised). The overbars represent seasonal averaging, and N gives the number of days over which the averaging is to be performed.

The null hypothesis in the paired-sample t test is that the means of the two differences analysed are the same. The probability that the this null hypothesis can be rejected is evaluated using a so-called p value—obtained from a probability distribution known as the Student's t distribution—which gives the probability that the magnitude of the calculated variable t can be attributed purely to chance [Press, 2007, p. 727]. A small p value, therefore, means that the test statistic is likely to be robust, indicating that the means of the differences in questions are significantly different from one another, and the null hypothesis can be rejected. The critical p value for rejecting the null hypothesis in the present thesis is chosen as $p = 0.05$; when the value of p is lower than this, the means of the differences are said to be significantly distinct at the 5% significance level. In this thesis, the t test is conducted in Matlab using the built-in *ttest* function.

Sea-Surface Temperature Improvement

The SST is also analysed in terms of a seasonally averaged parameter which will be referred to as the *improvement* over the control run induced by the introduction of the Langmuir turbulence parameterisations into the KPP mixing scheme. Letting O_i represent the daily SST values in a particular grid cell in the interpolated OSTIA reanalysis, and M_i (as above) the corresponding modelled SSTs in the same grid cell, the seasonally averaged SST improvement, I_{SST}, in each grid cell is defined as

$$I_{SST} = \frac{1}{N}\sum_{i=1}^{N}\Big\{|O_i - M_i^c| - |O_i - M_i^p|\Big\}, \tag{3.6}$$

where N is the number of days over which the seasonal averaging is performed. Since the model is integrated over a period of 2 years (2007–2008), $N = 179$ for the JFM average and $N = 182$ for the JAS average. The unit of I_{SST} is temperature (in °C), and a positive value indicates that the parameterised model run gives an SST estimate that is closer to the reanalysis than the SST estimate produced by the control run, whereas a negative improvement implies that the control run is more accurate. The improvement is calculated separately for each focus region.

The SST improvement will be displayed in the form of so-called box plots, which include six statistical characteristics concerning the spatial distributions of the improvement within each focus region: the median (indicated by horizontal lines inside the boxes), the first and third quartiles (the upper and lower edges of the boxes, respectively), the upper and lower extremes (the upper and lower whiskers, respectively), and the statistical significance of the difference between the medians, depicted by notches surrounding the median lines. The statistical significance of the difference between medians is determined by whether the notches surrounding the median lines overlap. This approximate visual measure implies that the difference between two medians is statistically significant at a roughly 95% level of confidence if the notches do not overlap. Where the notches do overlap, a statistically significant difference between the medians may not be asserted [McGill et al., 1978]. In the current thesis, the box plots in Chapter 4 are also generated in Matlab, using the built-in *boxplot* function.

Root-Mean-Square Error and Bias

The comparison of the model results against the EN4 observed vertical temperature profiles is presented in the form of vertical profiles of the root-mean-square error (RMSE) and the bias (B) between the model and the observations, averaged both seasonally (JFM and JAS averages) and spatially (over the focus areas). Each focus region is layered vertically into 37 layers of downward-increasing thickness, and the seasonal-average RMSE of the temperature (in units of °C) within each vertical layer is computed in the conventional way [see, e.g., Willmott and Matsuura, 2005] as

$$\mathrm{RMSE} = \left[\frac{1}{N}\sum_{i=1}^{N}(M_i - O_i)^2\right]^{1/2}, \tag{3.7}$$

where X_i and Y_i represent the observed and the modelled temperatures, respectively, in each observation location i within the layer. The seasonally averaged bias,

$$\mathrm{B} = \frac{1}{N}\sum_{i=1}^{N}(M_i - O_i), \tag{3.8}$$

is layer-averaged over the same vertical intervals as the RMSE.

The RMSE is commonly used as an indicator of model performance in physical sciences owing to its practicality and apparent simplicity of interpretation: the measure has the same dimension as the variable on which it is based (in the present case temperature), and the squaring of the model–observation errors gives an indication of the magnitude of the errors [Willmott and Matsuura, 2005]. However, as discussed by Willmott and Matsuura [2005], the RMSE is *not* a measure of the true average error and, in fact, lacks a clear physical interpretation; in addition, the use of squared errors may give unwarranted weight to abnormally high model–observation differences [e.g., Legates and McCabe, 1999]. With these restrictions in mind, the RMSE is, nonetheless, chosen as a model performance measure in the present thesis to enable comparisons to previous studies [e.g., Li et al., 2016; Wang et al., 2010] in which it has been used as a model performance estimator.

For unbiased estimators, the RMSE equals the variance, or scatter, of the estimator around its average [e.g., Thomson and Emery, 2014, p. 235]. However, the influence of the bias is made clear by the following decomposition [e.g., Mentaschi et al., 2013]:

$$\mathrm{RMSE}^2 = \mathrm{SC}^2 + \mathrm{B}^2, \tag{3.9}$$

where SC expresses the scatter component of the RMSE,

$$\mathrm{SC} = \sqrt{\frac{\sum_{i=1}^{N} \left[(M_i - \overline{M}) - (O_i - \overline{O})\right]^2}{N}}. \tag{3.10}$$

The overbars in the above expression denote average values.

A geometrical interpretation of (3.9) reveals [see, e.g., Mentaschi et al., 2013, their Figure 3] that SC and B can be viewed as composing an orthogonal basis for the projection of the RMSE; an evaluation of model performance in terms of the RMSE is, therefore, incomplete without an explicit specification of the bias. Mentaschi et al. [2013] further caution that low values of the RMSE, which in theory indicate skilful model predictions, may overestimate the model performance in the presence of significant negative biases.

Chapter 4

Results

The current chapter displays results obtained from the free (i.e., no data assimilation) historical model runs of the HYCOM ocean model implemented in the TOPAZ4 data assimilation system, using the K profile Parameterisation (KPP) vertical mixing scheme. The model is integrated for two years, 2007–2008, in five different configurations: one control run is performed in which no surface wave-related modifications to the model equations or the KPP scheme are made, and four runs are performed in which Stokes drift terms are added to the momentum and tracer-advection equations (the Coriolis-Stokes and the CL vortex forces, and the advection by the Stokes transport, respectively) following the principles of McWilliams and Restrepo [1999] and the KPP scheme is modified according to the Langmuir turbulence parameterisations presented in Section 2.2.5.

In the figures and text of the current chapter, abbreviations are used to refer to the different Langmuir turbulence parameterisations. The McWilliams and Sullivan [2000] parameterisation is referred to as MS2000; Smyth et al. [2002] as S2002; Harcourt and D'Asaro [2008] as HD2008; and Takaya et al. [2010] as T2010. The control run without wave effects is referred to as CTRL.

In the first section, a descriptive analysis of the modelled mixed-layer response is provided, including comparisons with the IFREMER gridded MLD climatology [de Boyer Montégut et al., 2004]. Section 4.2 examines the model performance in simulating the sea-surface temperature (SST) and compares the model output to the OSTIA SST reanalysis [Donlon et al., 2012]. Finally, in Section 4.3, the modelled subsurface temperature response is evaluated against the instantaneous vertical temperature profiles of the EN4 dataset [Good et al., 2013].

4.1 Mixed Layer Depth (MLD)

4.1.1 Overview

Figure 4.1 shows the average mixed layer depth (MLD) of the winter months January, February, and March (JFM), for both the IFREMER 1961–2008 climatology and the five HYCOM model runs of the years 2007–2008, projected onto maps of the TOPAZ4 model domain (excluding areas north of 80°N). Figure 4.2 shows similar maps for the summer months July, August, and September (JAS). In all cases, the MLD is calculated using the density threshold criterion of de Boyer Montégut et al. [2004], where the MLD is defined as the depth at which the water density increases by 0.03 kg/m^3 from a reference value at 10 m depth. However, instead of using the first HYCOM layer interface at which the threshold is exceeded as the estimate for the MLD, a linear interpolation is performed between that layer and the one above for a more conservative estimate (see also Section 4.1.5).

The winter (JFM) climatological mean MLD is shown in Figure 4.1(a). The IFREMER climatology is shown to have two regions characterised by comparatively deep mixed layers, one in the Labrador Sea southwest of Greenland, and another in the central Greenland Sea off the east coast of northern Greenland. The deepest average winter mixed-layer depth is found in the latter region, where the MLD reaches approximately 1300 metres. The figure also shows the boundaries of four focus regions that will be analysed in more detail. Chosen to represent unique water mass characteristics, the focus regions are defined as follows: Region A covers approximately the Sargasso Sea area, Region B is designed to include the majority of the Gulf Stream system as it escapes offshore off the North American east coast, Region C covers the bulk of the Labrador and Irminger Seas surrounding the southern tip of Greenland, and Region D contains large parts of the North and Norwegian Seas.

A map of the JFM average mixed-layer depths produced by the control run, in which no surface-wave effects are included, is shown in Figure 4.1(b). In contrast to the IFREMER climatology, the control run generates the deepest mixing in the Labrador and Irminger Seas south of Greenland–areas known for deep convection triggered by strongly destabilising surface heat fluxes in the winter season [Lazier et al., 2002]. The deepest average modelled MLDs in this region surpass 1200 m. Moderate to deep mixing is also produced over much of the mid-latitude storm track, extending from the central east coast of North America to the Norwegian Sea.

The MS2000 Langmuir turbulence parameterisation induces intense wintertime mixing in the waters surrounding southern Greenland (Figure 4.1(c)). The average MLD in this region exceeds 1800 m in parts, the deepest among all model runs. Whilst this may appear excessive, mixed-layer depths of similar magnitude have episodically been observed in the region [see, e.g., Lazier et al., 2002]. MS2000 also intensifies the mixing compared to the control run within

the mid-latitude storm track region, whereas low latitudes appear relatively unaffected by the parameterised turbulence enhancement.

Less vigorous than MS2000, the S2002 parameterisation—shown in Figure 4.1(d)—nonetheless induces strong enhanced wintertime mixing over the control in the Labrador and Irminger Seas region, with maximum average MLDs approaching 1600 m. S2002 is the only parameterisation of those included to explicitly consider the stability of the water column, restricting the effect of wave-enhancement in strongly destabilising surface forcing. These stabilising effects notwithstanding, S2002 is shown to produce the second-deepest MLD estimates out of all five model runs.

Figure 4.1(e) shows the JFM average MLD field induced by parameterising the Langmuir effects with HD2008. The mixing effects of HD2008 are moderate in comparison to the other parameterisations tested; in fact, the maximum average MLD produced by HD2008 is lower than the maximum produced by the control run by roughly 50 m (1233 m for HD2008 against 1282 m for CTRL), implying that parameterising the surface-wave effects as a function of La_t may, in certain conditions, act to stabilise the water column. This, however, is likely a result of minor water mass circulation changes caused by the differences in mixed-layer dynamics between the model runs. The Langmuir enhancement factor is, after all, a positive definite function and therefore cannot directly reduce the modelled turbulent diffusivities.

The fourth parameterisation tested, T2010, generates the average wintertime MLD field shown in Figure 4.1(f). The mixing effect produced by T2010 is very similar to that produced by S2002—the deepest mixed-layer depth, for instance, being only 70 m shallower (1512 for T2010, 1582 for S2002)—even though the Langmuir enhancement factor of S2002 is a function of both the convective velocity scale, w_*, and the turbulent Langmuir number, La_t, whereas the one defined by T2010 only depends on La_t.

A striking feature of the maps included in Figure 4.1 is that the MLD fields of the various model runs, even after seasonal averaging over two years, all display almost identical large-scale spatial patterns. This suggests that the dominant effect of parameterising Langmuir turbulence in KPP—using the prevailing F_{LC}-dependent methodology introduced by McWilliams and Sullivan [2000], implemented in each of the four parameterisations included in this study—is a highly localised enhancement of the mixing rate; the large-scale model dynamics appear largely unaffected by the introduction of surface-wave parameters, at any rate in the comparatively short, two-year model integrations performed in the present study.

The summer (JAS) modelled mixed-layer depth fields, shown in Figures 4.2(b)–4.2(f), imply dramatically weaker mixing rates throughout the entire model domain; likewise, differences among the various model runs are markedly smaller in magnitude than in the winter (JFM) season. The SM2000 (Figure 4.2(c)) and S2002 (Figure 4.2(d)) parameterisations once again

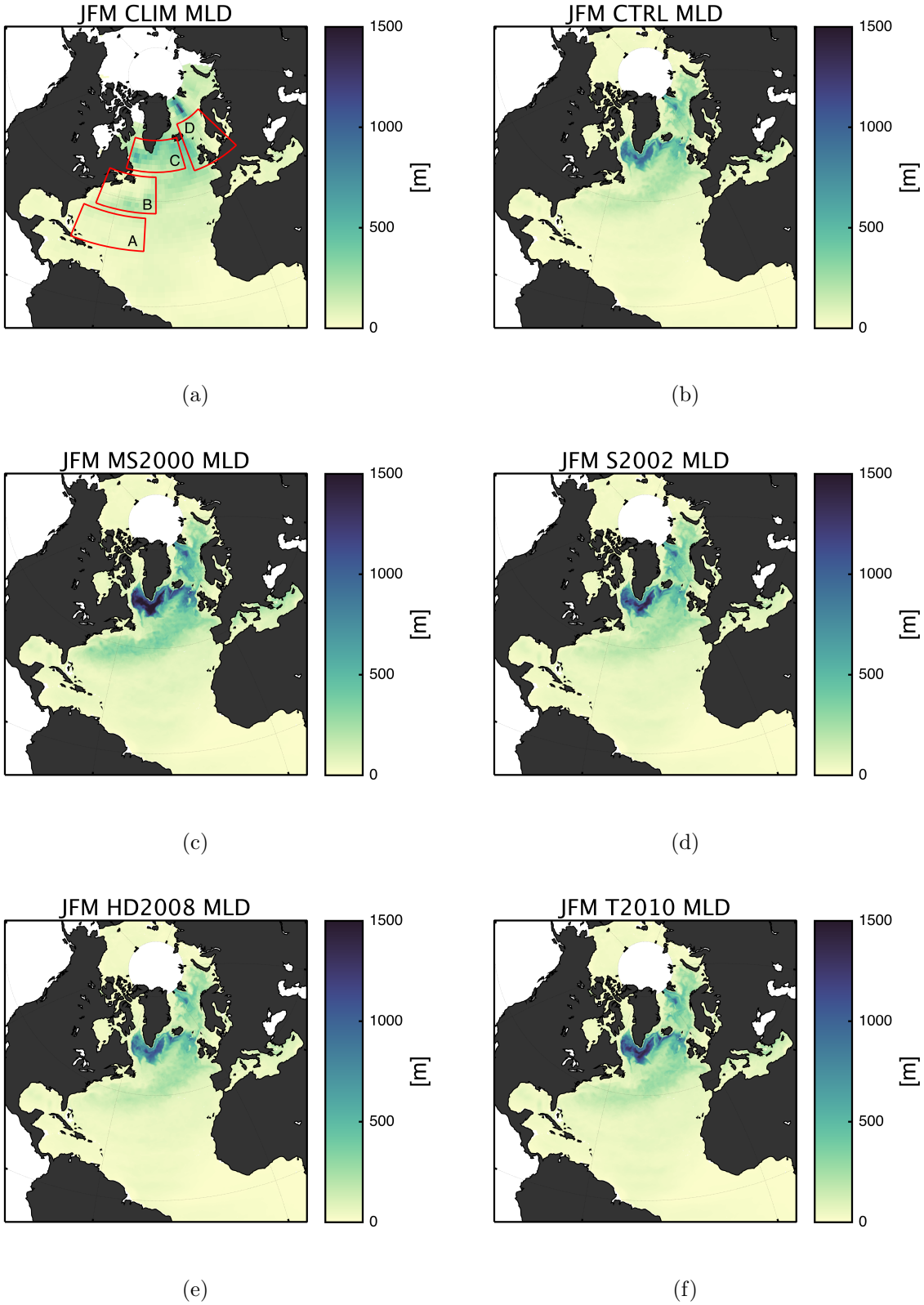

FIGURE 4.1: January-February-March (JFM) mean mixed-layer depths (MLD) over the model domain for 2007-2008. (a) shows the IFREMER 1961–2008 gridded monthly MLD climatology (CLIM) based on the method developed by de Boyer Montégut et al. [2004]; (b) shows the control run (CTRL) without wave forcing; (c) shows the model run using the MS2000 parameterisation; (d) shows S2002; (e) shows HD2008; and (f) shows T2010.

produce the deepest-reaching mixing, with maximum MLDs of roughly 100 m, although CTRL (Figure 4.2(b)), HD2008 (Figure 4.2(e)), and T2010 (Figure 4.2(f)) all come close, with maxima of roughly 90 m. The deepest MLDs are found in the low latitudes south of the equator, presumably owing to the fact that JAS constitutes the winter season in the Southern Hemisphere. The IFREMER gridded climatology (Figure 4.2(a)) appears to exhibit largely similar spatial patterns and MLD magnitudes to the model runs, suggesting that the model produces realistic levels of mixing in the typically stable surface forcing conditions found in summer months. As in the winter, the mixing is highly local—although perhaps less obviously so—as evidenced by certain unchanging spatial patterns present in all model runs.

4.1.2 Zonal Averages

Among the model runs, the most moderate MLD estimates are invariably produced by the control experiment in which no surface-wave effects are included. This is a natural consequence of the method by which the mixing by Langmuir turbulence is parameterised in the KPP scheme. Equations (2.42) and (2.43) make it clear that the Langmuir enhancement factor, F_{LC}, can only act to increase the turbulent velocity scale, W. This velocity scale, in turn, is used to determine the boundary layer depth, h_{bl} (see (2.5)), over which the KPP scheme performs the vertical mixing of the upper-ocean model variables.

Differences in MLD between the model runs are apparent in Figure 4.3, which plots zonally averaged mixed layer depths over the model domain from South to North. Figure 4.3(a), which depicts Northern-Hemisphere winter (JFM) means of the zonally averaged MLDs, shows that the deepest mixing throughout the majority of the North Atlantic is induced by the MS2000 parameterisation (red line), with average mixed-layer depths exceeding 500 metres in roughly the 55°N–65°N latitude range. Following MS2000 are the T2010 (green) and S2002 (yellow) parameterisations, with maximum mean MLDs surpassing 400 metres, although in a narrower region surrounding the 60°N latitude than that in which MS2000 exceeds 500 m. HD2008 (purple) closely resembles the control run in most of the model domain, an observation that is perhaps more clear in Figure 4.3(c), which plots the differences between the JFM means of the control run against the parameterisations and the climatology. The climatology (grey) exhibits slightly deeper JFM mean mixed-layer depths than any of the model runs in the equatorial latitudes between 10°S and 10°N, and markedly shallower MLDs in the mid to high latitudes between roughly 50°S and 65°N. Interestingly, the climatological mean MLD north of 70°N is clearly deeper (around 200 m) than that of the model runs, all of which appear to converge to a depth of around 50 m as the 80°N boundary is approached.

The Northern-Hemisphere summer (JAS) means of the zonally averaged MLDs and MLD differences against the control run are plotted in Figures 4.3(b) and 4.3(d), respectively. The

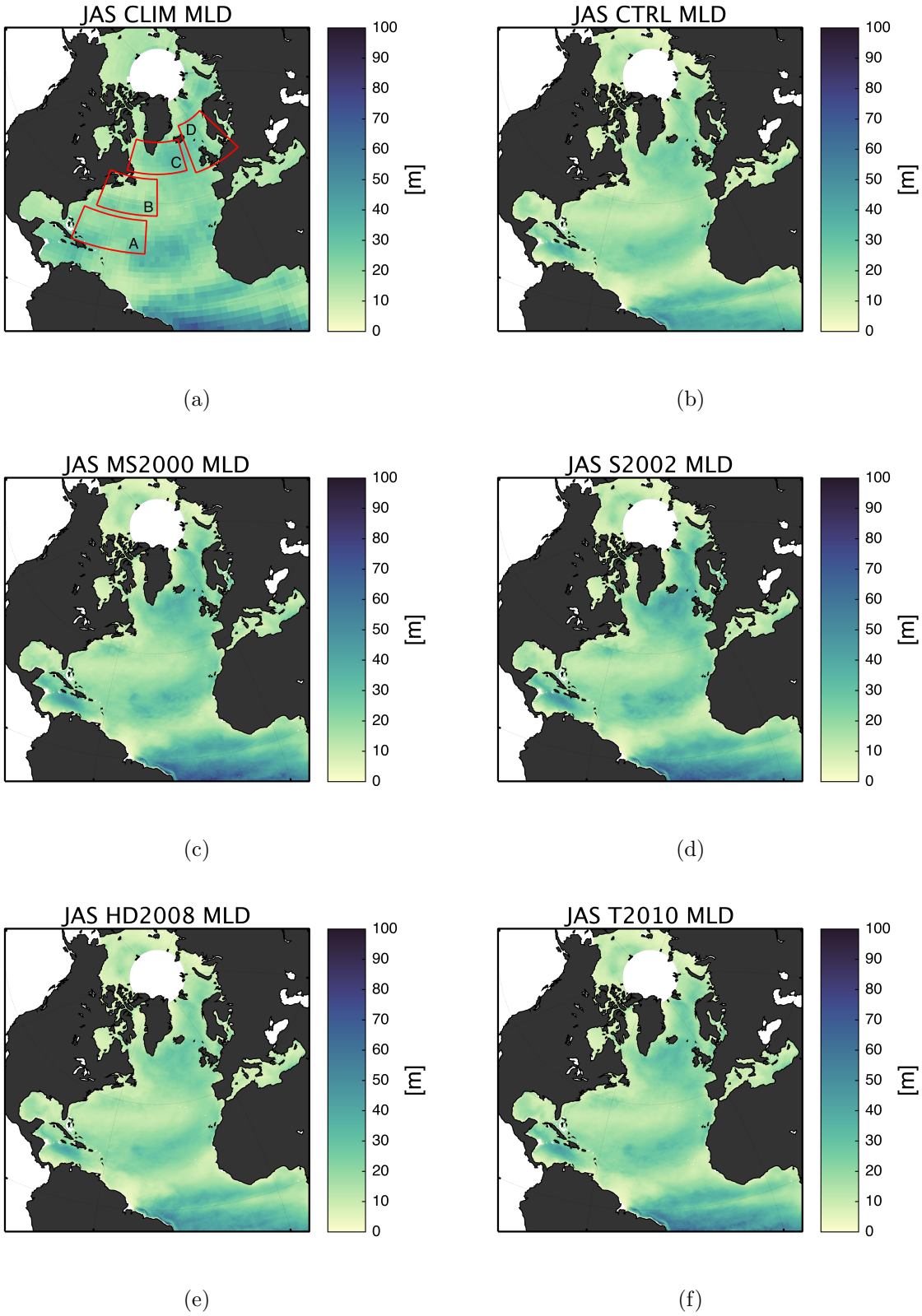

FIGURE 4.2: As Figure 4.1 but for July-August-September (JAS). Note that the colour scaling differs from Figure 4.1.

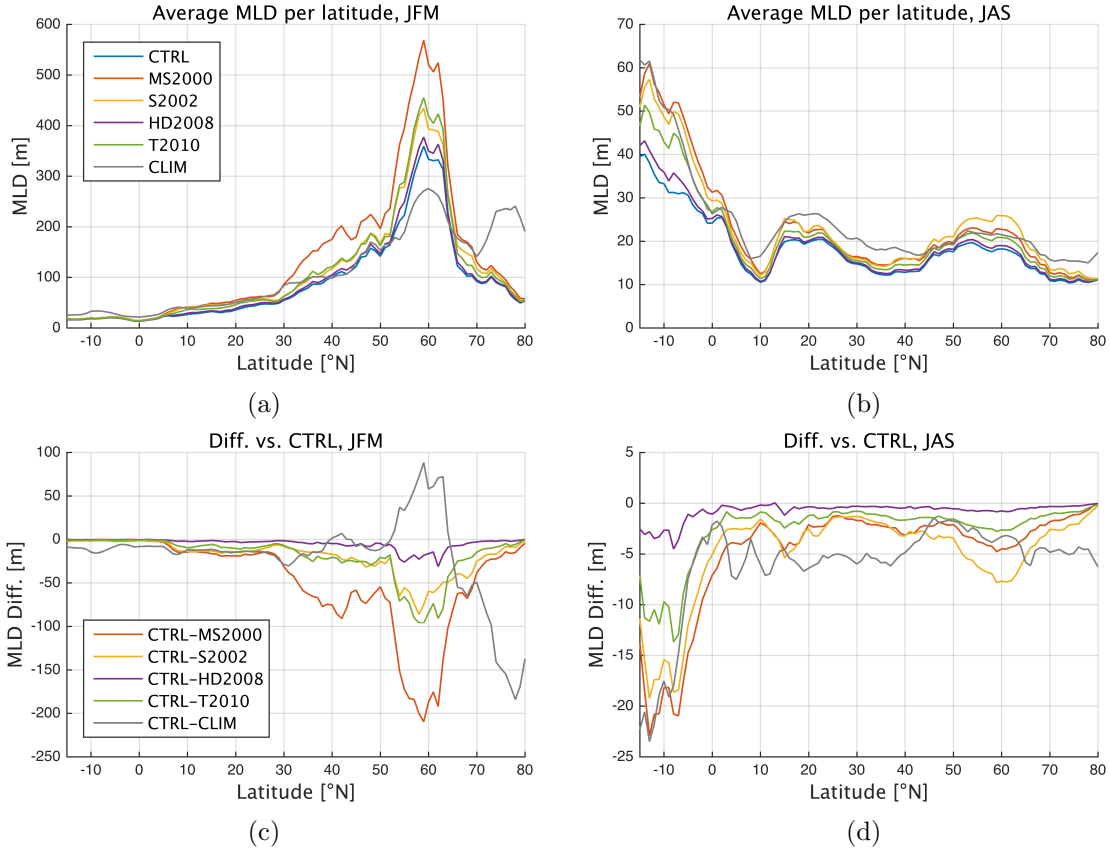

FIGURE 4.3: Zonal averages of MLD between 15°S–80°N in the model domain for (a) the January-February-March (JFM) mean of 2007-2008; and (b) the July-August-September (JAS) mean of 2007-2008. The grey lines show the IFREMER climatology. The control run is shown in blue; the run with the MS2000 parameterisation in red; S2002 in yellow; HD2008 in purple; and T2010 in green. Figures (c) and (d) show the corresponding differences relative to the control run. Note that the vertical scale differs between the plots.

deepest mixed layers in this season are found south of the Equator, most likely owing to the fact that July, August and September are winter months in the Southern Hemisphere. Of the model runs, MS2000 once again produces the deepest mixing in the low latitudes, but S2002 catches up north of 10°N, and eventually surpasses the other parameterisations in the mid and high latitudes. This behaviour may be related to the explicit dependency of the S2002 parameterisation on stability parameters, a property which allows for enhanced mixing in the stabilising forcing conditions often found in summer months. It should be noted, however, that the summer MLD differences among the parameterisations are small—on the order of ten to twenty metres at most—compared to the large ($\mathcal{O}(100m)$) differences induced by convective mixing in the winter months. In contrast to the winter months, the summer climatology is on average slightly deeper than the model runs north of the Equator—apart from a region in the mid latitudes between 45°S and 65°N in which S2002 and MS2000 induce deeper mixing—and the control run consistently produces the shallowest MLD estimates.

4.1.3 Time Evolution of the MLD

Time series of the MLD evolution, shown in Figure 4.4, illustrate the seasonal variability of the mixing produced in the different model runs within the four focus regions indicated in the maps in Figures 4.1 and 4.2. The numerous, comparatively large fluctuations in MLD produced by MS2000 in the Sargasso Sea region (Focus Region A; Figure 4.4(a)) indicate that the model responds rapidly to the enhanced levels of mixing, especially in winter months. Similar, although markedly more pronounced, behaviour is observed in the Gulf Stream region (Focus Region B; Figure 4.4(b)), where MS2000 causes the winter MLDs to far exceed the values produced by the other parameterisations. All model runs create comparatively deep winter mixed layers in the Labrador and Irminger Seas region (Focus Region C; Figure 4.4(c)); the MS2000 parameterisation is again the most vigorous, although less obviously so than in the Gulf Stream region. It is probable that the deep mixing in Region C is due to a combined effect of strong convective and wind and wave forcing. In the North and Norwegian Seas region (Focus Region D; Figure 4.4(d)), the model runs can roughly be divided into three groups; CTRL and HD2008 perform alike, producing the lowest average winter mixed-layer depths, while S2002 and T2010 induce deeper-reaching, and very similar, average mixing. The clearly deepest mixing is in this region is, expectedly, produced by MS2000. In all regions, the MLDs induced by all model runs converge to low values in summertime.

4.1.4 Impact of the Langmuir Stability Length

Motivated by the observed and hypothesised dissimilarities between Monin-Obukhov (M-O) similarity theory and the similarity scaling theories of Langmuir turbulence (see Section 2.2.4), an experiment (denoted S2002LLC) was conducted in which L_{MO} (the M-O length scale) was replaced by the Langmuir stability scale, L_{LT}, introduced by Belcher et al. [2012], in the KPP mixing scheme. Defined in (2.41), the Langmuir stability length weighs the relative importance of the buoyant production or suppression of turbulent kinetic energy (TKE) against the impact of the Stokes production associated with the surface waves. L_{MO} acts as an upper bound for the KPP boundary-layer depth h_{bl} in conditions characterised by stabilising surface forcing; by using L_{LT} instead of L_{MO}, the upper bound for h_{bl} can be expected to increase in strongly wave-forced regimes. It should, however, be kept in mind that the condition that restricts h_{bl} to values lower than these length scales is only put into effect when the traditional bulk Richardson number criterion produces a deeper boundary-layer depth estimate.

Figure 4.5 shows the zonally averaged JFM (a) and JAS (b) mean mixed-layer depths produced by the regular S2002 parameterisation (identical to Figure 4.3) and the S2002LLC experiment, as well as the differences between the two. The figures reveal that the effect of using the Langmuir stability length instead of the M-O length scale is minimal: the largest differences

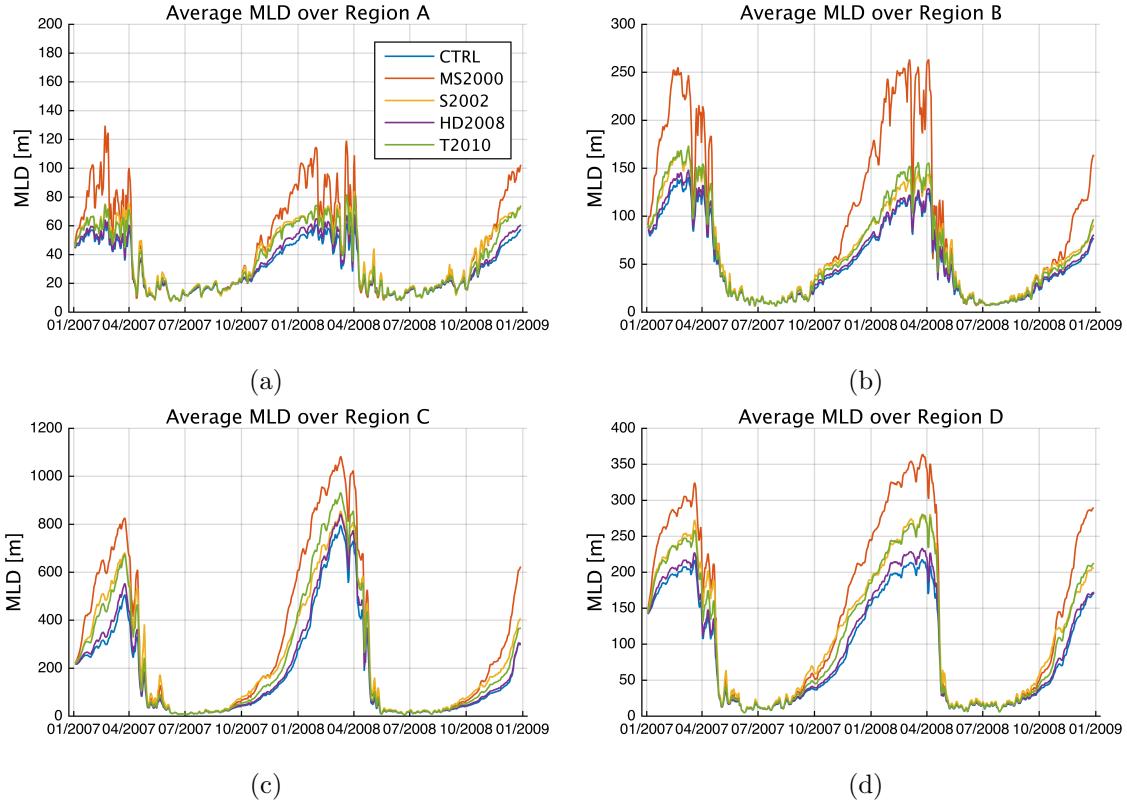

FIGURE 4.4: Time series of modelled mixed-layer depths (MLD) averaged over the four focus regions: (a) the Sargasso Sea region (Region A), (b) the Gulf Stream region (Region B), (c) the Labrador and Irminger Seas region (Region C), (d) and the North and Norwegian Seas region (Region D). The colour coding follows that used in previous figures. Note that the scaling differs between all subfigures.

occur in the mid to high latitudes in winter, but even here the differences are modest at less than 10 m in magnitude—by comparison, the maximum difference between the control run and the MS2000 parameterisation was as high as 200 m in the winter months (see Figure 4.3(c)). In the summer, when the surface buoyancy fluxes may be expected to be stabilising more often than in winter owing to warmer air temperatures and calmer winds, the zonal-mean MLDs deviate even less (on the order of a few meters at most) between the two experiments. Also of note is that the S2002 experiment generally produces deeper mixed layers in both seasons, especially in low to mid latitudes.

4.1.5 Limitations of MLD for Model Validation Purposes

Comparing the mixed-layer depths (MLD) of large-scale ocean model runs with climatological fields—as was done above—can give useful insights into the behaviour of the model and the implemented mixing scheme; however, using the mixed-layer depth as a model validation parameter involves certain complications that are worth keeping in mind. For instance, the potential for large distances between isopycnic or z layer surfaces in highly unstratified regions

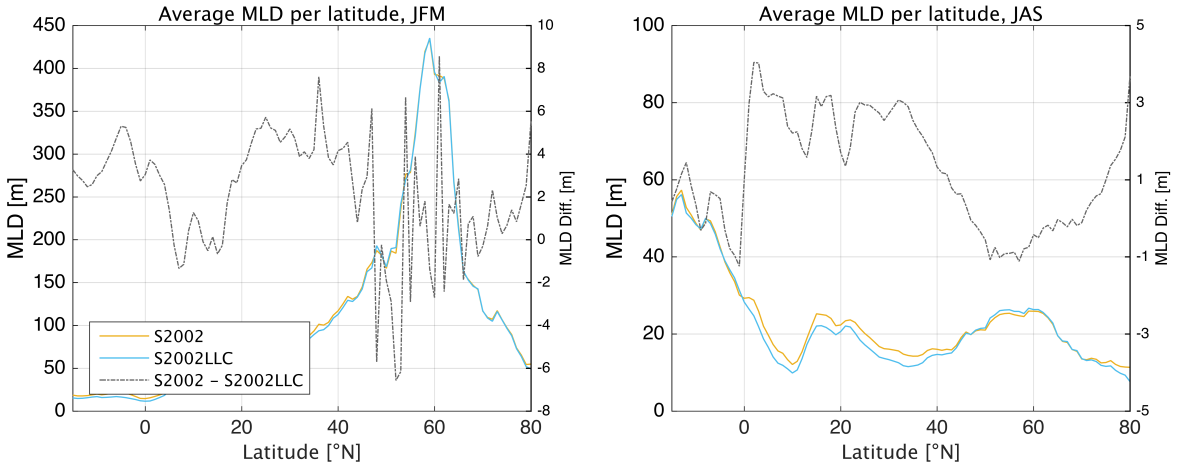

(a) (b)

FIGURE 4.5: Zonally averaged January-February-March (a) and July-August-September (b) mean MLD for the regular S2002 parameterisation (yellow) and the S2002LLC experiment (blue), in which the Monin-Obukhov length, L_{MO}, has been replaced by the Langmuir stability length, L_{LT}, in the KPP scheme. The criterion in the KPP scheme preventing the boundary-layer depth from exceeding L_{MO} kicks in when the surface buoyancy forcing is stabilising, that is, $B_f < 0$. Being the only parameterisation of those included in the present study to take buoyancy effects into account, the S2002 parameterisation has been chosen for the current experiment. The grey dashed-dotted lines are drawn relative to the right-hand y axes, and show the differences between S2002 and S2002LLC. Note that the scales of the two graphs differ in the y direction.

may induce large variations in MLD in deep mixed layers depending on the choice of method by which the modelled MLD is approximated [Sallée et al., 2013]. To illustrate this, Figure 4.6 shows two different estimates of the zonally averaged winter (JFM) MLD calculated from the same model output (i.e., output from the run in which the MS2000 parameterisation was used). The orange line in the figure is the MLD calculated by the standard, linear interpolation method used in all MLD estimates in the present study (see Sections 3.3.1 and 4.1.1), whereas the red line is calculated by simply using the vertical layer interface at which the density criterion of de Boyer Montégut et al. [2004] is fulfilled as the mixed-layer depth estimate. Clearly, the standard estimate that involves interpolation between model layers (MS2000) is more conservative than the alternative estimate in which no interpolation is used (MS2000NI); in the sub-polar latitudes, the differences in the zonal averages exceed 100 m. Because these purely definition-dependent differences are on the order of the root-mean-square errors (RMSE) of modelled–observed MLDs reported for the MS2000 and S2002 parameterisations in previous studies [e.g., Li et al., 2016], the MLD is not used for validation purposes in the present study, but has nonetheless been included in order to illustrate the impact on the mixing induced by the different parameterisations.

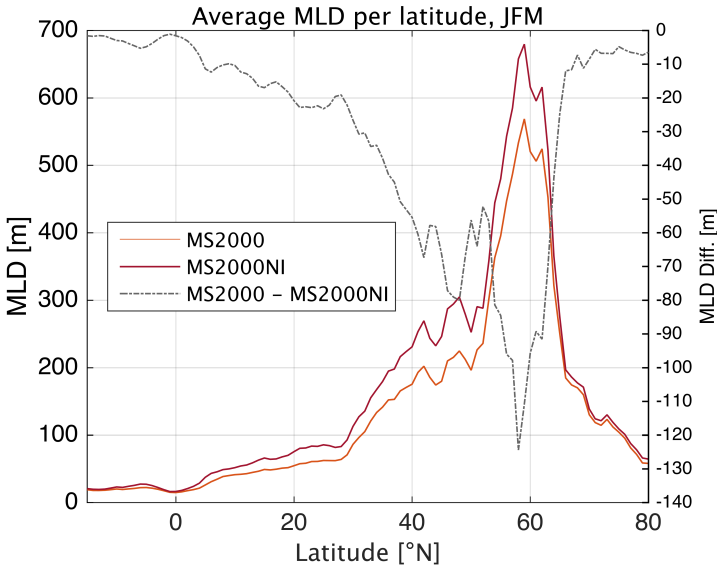

FIGURE 4.6: Orange line: the JFM zonal averages of the modelled mixed-layer depth (MLD) produced by the MS2000 parameterisation, estimated by the linear interpolation method used throughout the present thesis (i.e., the same as shown in Figure 4.3(a)); red line: the zonally averaged JFM MLD produced by MS2000, estimated using no interpolation (hence the NI in the label MS2000NI, implying No Interpolation), simply assigning the MLD to the nearest isopycnic-layer surface corresponding to the density criterion of de Boyer Montégut et al. [2004]; grey line: the difference between MS2000 and MS2000NI. The left-hand y axis is associated with the coloured, solid lines, while the dashed-dotted grey line is to be read relative to the right-hand y axis.

4.2 Sea-Surface Temperature (SST)

4.2.1 Overview

The SST is compared in terms of differences between the OSTIA reanalysis [Donlon et al., 2012], interpolated to the model grid, and the five model runs. Table 4.1 lists the statistical significance (obtained using the Student's t test presented in Section 3.3.2) of the differences between SST fields produced by the control run and the parameterised runs, in the entire model domain (TP4) as well as in the different focus regions. It is obvious that the changes in SST resulting from parameterising Langmuir turbulence effects are widely significant. As expected, MS2000 induces noticeable changes in the surface temperature fields in most regions and seasons; the smallest effects are observed in the Labrador and Irminger Seas region (Region C) in winter, when additional mixing of the already-well-mixed water masses produced by the control run has a slightly more limited impact on the SST. The changes in SST induced by S2002 are highly significant in all regions in summer, when stabilising surface forcing causes the parameterisation to enhance the turbulent mixing; a somewhat weaker impact is observed in the more unstable conditions prevalent in winter months. While producing the most moderate changes in MLD out of the four parameterisations tested, HD2008 nevertheless induces statistically significant

TABLE 4.1: Percentage of grid cells showing statistically significant (at the 95% significance level) JFM (JAS) differences in SST relative to the control run. The regions covered are the complete TOPAZ4 model domain (TP4), and the four focus regions (A-D). The significance is estimated with the paired-samples Student's t test described in Section 3.3.2.

Region	MS2000	S2002	HD2008	T2010
TP4	91.8 (91.1)	83.5 (90.5)	75.7 (77.1)	82.6 (86.6)
A	96.4 (100.0)	73.7 (100.0)	79.8 (87.5)	78.7 (98.72)
B	95.8 (92.9)	85.6 (91.9)	82.2 (79.7)	87.6 (87.2)
C	88.9 (97.3)	84.1 (99.6)	83.5 (85.0)	86.7 (93.4)
D	93.1 (95.4)	90.5 (97.1)	86.9 (87.4)	92.5 (92.0)

SST changes in large parts of the model domain; furthermore, comparatively small variation is observed in the number of grid cells showing statistically significant differences between seasons within the majority of the focus regions—an exception being the Sargasso Sea (Region A), in which differences to the control run are more noticeable in summer than in winter. While it was shown in Section 4.1 that T2010 often performs similarly to S2002, Table 4.1 shows that T2010 tends to induce somewhat more modest changes in summer months and, especially within the focus regions, slightly more widespread changes in winter months (as mentioned above, unstable stratification reduces the enhancement factor of S2002, whereas T2010 has no explicit stability dependence).

Shown in Figure 4.7(a) is the mapped JFM mean SST calculated from the daily OSTIA reanalysis data. Mesoscale eddying features and other fine-scale SST structures have clearly been smoothed out by the seasonal averaging. The white spots adjacent to the east coasts of North America and Greenland indicate grid cells with sea ice; the temperatures for these locations are excluded from the dataset and, consequently, from the present analysis.

Figure 4.7(b) shows the difference between OSTIA and the control run in which surface wave effects are neglected, with the boundaries of the four focus regions overlaid in red. The control run obviously severely overestimates the SST—with differences exceeding 5 °C—in the western and central parts of the Gulf Stream system, as indicated by the dark blue band running through the middle of Region B. Most likely, however, much of this error stems from an often observed [see, e.g., Sakov et al., 2012] mismatch between the modelled and reanalysed location of the core of the Gulf Stream, and cannot, therefore, be attributed primarily to biases originating from misrepresentations of the turbulent mixing. Regions where the control run underestimates the SST are found chiefly in mid to high latitudes. Areas ranging from the eastern edge of Region B to the central and eastern parts of Region C, which encompasses the Labrador and Irminger Seas surrounding the southern tip of Greenland, along with large parts of the Northern and Norwegian Seas (covered by Region D) are characterised by lower-than-observed SST, as indicated by the dark green colours in the figure. Outside the focus areas, the model appears to somewhat overestimate the temperature offshore from the western coast of North Africa.

The Northern-Hemisphere winter (JFM) average differences between the control run and the MS2000 parameterisation, shown in Figure 4.7(c), indicate that the parameterised model run produces noticeably colder surface temperatures in mid- to high-latitude regions of the model domain. This is a likely consequence of the vigorous wintertime mixing induced by MS2000 seen in Figures 4.3(a) and 4.3(c), which efficiently transports water properties vertically and thus consistently exposes new water masses the air above the sea surface. Warmer SSTs relative to the control are also produced by the MS2000 parameterisation in the Labrador Sea southwest of Greenland and in the Greenland sea region north of Iceland.

Figure 4.7(d) shows the JFM average SST differences to CTRL attributable to representing the Langmuir turbulence effects with the S2002 parameterisation, which, unlike the other parameterisations included, explicitly accounts for buoyancy effects. A marked reduction in the difference to the control is observable compared to the large deviations produced by MS2000; this implies that the stability dependency of S2002 is effective in reducing turbulent mixing rates in destabilising surface forcing, as intended. Whether the reduction in intensity is sufficient is, however, questionable; as was shown in Figure 4.7(b), the control run already underestimates the SST compared to the reanalysis in many regions, indicating that the mixing induced by the standard model configuration may already be too vigorous. Thus, any additional enhancement of turbulent diffusivities (the effect of all four parameterisations) may be detrimental to model performance.

As shown in Section 4.1, the wintertime mixing that results from parameterising Langmuir turbulence with the HD2008 scheme exhibits comparatively small deviations from the control run in large parts of the model domain–a likely reflection of the relatively weaker sensitivity of the enhancement factor, F_{LC}, used in HD2008 to low values of La_t (see (2.46)) compared to the enhancement factors used in MS2000 (2.43) and S2002 (2.44). The weak additional mixing is also manifest in the modelled SST field (Figure 4.7(e)): neither substantial positive nor negative differences are observed, an exception being the Gulf Stream region where patches of positive and negative differences alternate roughly along the core of the main current system.

The JFM average SST field linked to the T2010 parameterisation is shown in Figure 4.7(f). Qualitatively, the model output most resembles that produced by S2002, with similar SST structures visible in the regions that lie to the south and west of southern Greenland. The T2010 parameterisation also appears to reproduce a narrow region of surface cooling relative to the control run along the East Greenland current–a pattern also visible in Figure 4.7(c) for MS2000; a close examination of Figure 4.7(b) shows that the control run tends to overestimate the surface temperature along the current.

The Northern-Hemisphere summer (JAS) mean SST of the OSTIA reanalysis for 2007-2008 is mapped in Figure 4.8(a), and the difference to the control run in Figure 4.8(b). As in the winter, the control run overestimates the surface temperature in the core of the Gulf Stream,

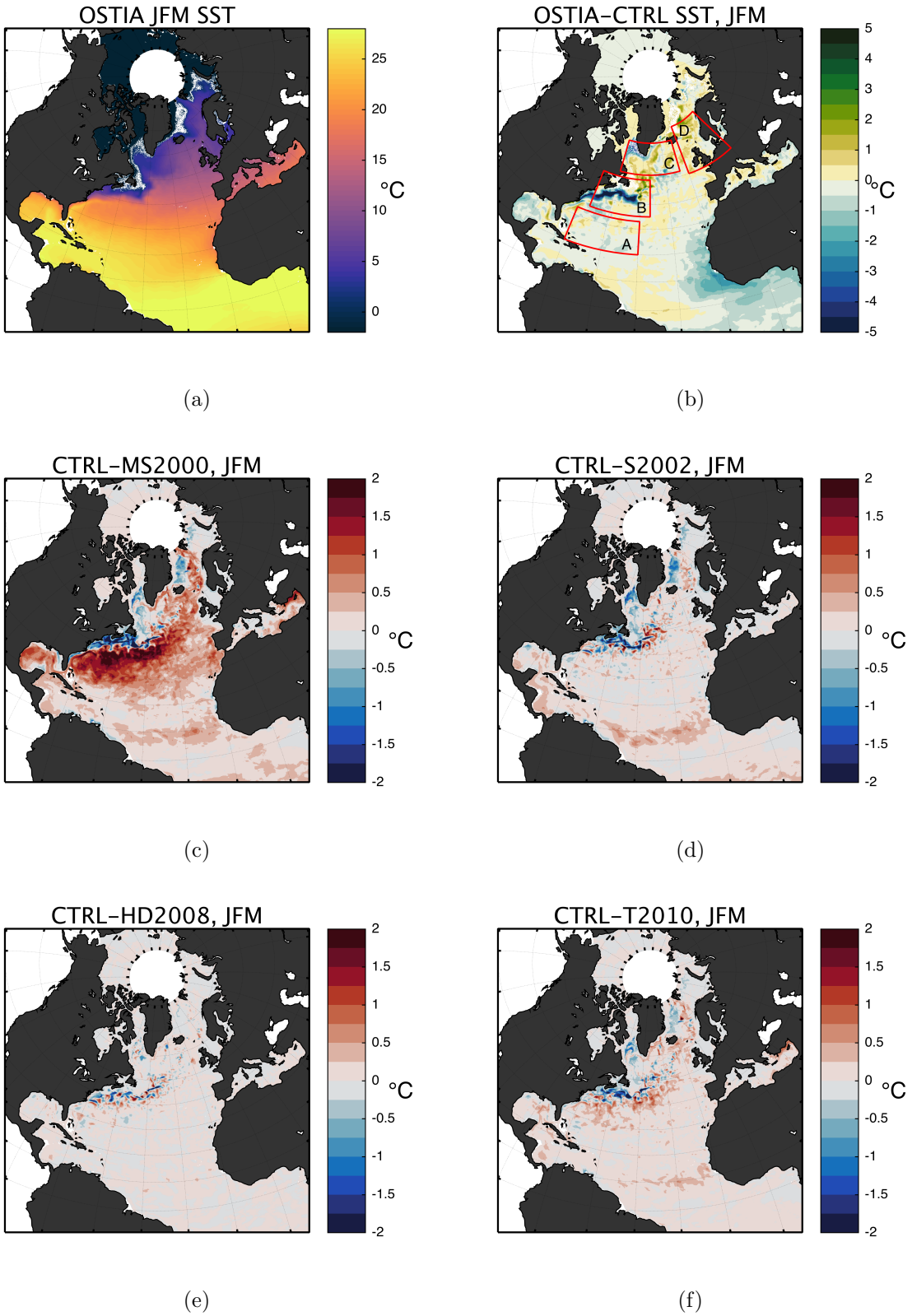

FIGURE 4.7: (a) January-February-March mean SST field from the OSTIA reanalysis interpolated to the TOPAZ4 model grid. (b) The difference between OSTIA and the control run, with positive (green) values indicating regions where the model underestimates the surface temperature and negative (blue) values indicating regions of overly warm modelled SST relative to the reanalysis. The regions marked with red borders indicate the four focus regions. (c)–(f) SST difference (in °C) relative to the control run using the MS2000, S2002, HD2008, and T2010 parameterisations, respectively. Positive (red) values indicate regions where the parameterisations produce colder SSTs than the control, and negative (blue) values show regions where the control is colder, indicating that the parameterisations induce a warming effect.

although the bias appears somewhat lower in magnitude in the summer season. Overall, south of roughly the 40 °N latitude, the control run slightly overestimates the SST in relation to the reanalysis. Regions of underestimation by the control are found immediately north and south of the Gulf Stream core, as well as in parts of the North Atlantic Drift extension. Moreover, the model produces lower-than-observed SSTs for various high-latitude regions and semi-enclosed seas, most notably the Hudson Bay and the Beaufort, East Siberian, Kara, and Baltic Seas.

Figure 4.8(c) shows that the enhanced turbulent mixing induced by the MS2000 Langmuir turbulence parameterisation produces colder sea-surface temperatures than the control run in most of the model domain also in the summer season. Certain high-latitude regions in which extensive river and glacial runoff and the melting of sea ice typically produce fresh surface layers that inhibit deep mixing in summer months, such as Hudson Bay [e.g., Ferland et al., 2011] and Baffin Bay off the western coast of Greenland [e.g., Zweng and Münchow, 2006], on the other hand, exhibit warmer surface temperatures in the MS2000 run, suggesting that the mixing induced by the parameterisation is strong enough to overcome the stable stratification, thus mixing warmer, subsurface water masses upward in the water column. MS2000 is the only scheme to produce this effect, however; none of the other parameterisations are able to pierce through the strong seasonal thermocline—S2002 (Figure 4.8(d)) produces colder SSTs than the control in the same regions, while HD2008 (Figure 4.8(e)) and T2010 (Figure 4.8(f)) produce scarcely noticeable effects.

Overall, S2002 produces a summertime (JAS) SST field comparable in magnitude to MS2000, with considerable cooling (on the order of 1 °C) relative to the control run over the bulk of the mid and high latitudes, whereas HD2008 and T2010 have a more moderate effect. Being the least sensitive to surface-wave forcing by design, the HD2008 parameterisation only produces noticeable average deviations from the control in the Gulf Stream region. T2010 appears to produce more widespread, albeit also comparatively weak, surface cooling over the control run.

4.2.2 SST Improvement

Figures 4.9 and 4.10 contain box plots of the average SST *improvement* (see Section 3.3.2) over the control run induced by the introduction of the Langmuir turbulence parameterisations into the KPP mixing scheme. The box plots provide descriptive statistics (again, see Section 3.3.2 for more information) of the improvement, in °C, relative to the OSTIA SST reanalysis in each of the four focus regions, averaged over JFM (Figure 4.9) and JAS (Figure 4.10). A positive improvement indicates that the parameterised model run reduces the magnitude of the SST bias compared to the control run, whereas a negative improvement implies the reverse.

As shown in Figure 4.9(a), the S2002, HD2008 and T2010 parameterisations produce a rather neutral improvement over CTRL in the Sargasso Sea region in winter, while MS2000 clearly

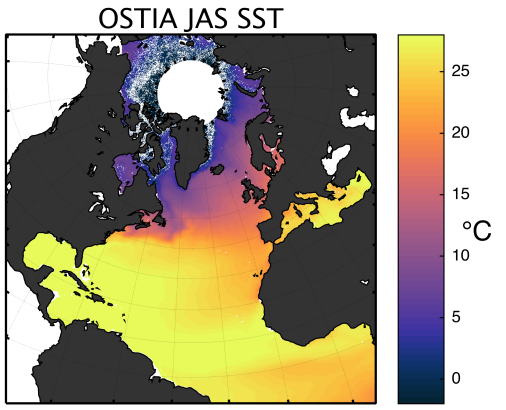

(a)

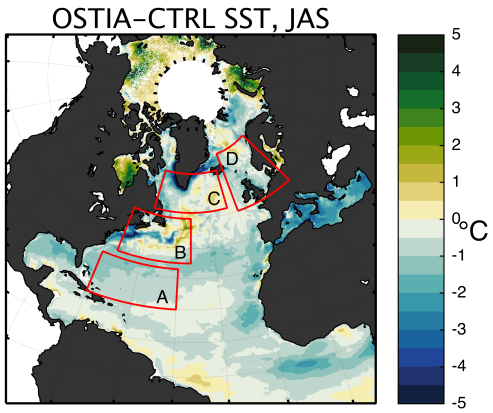

(b)

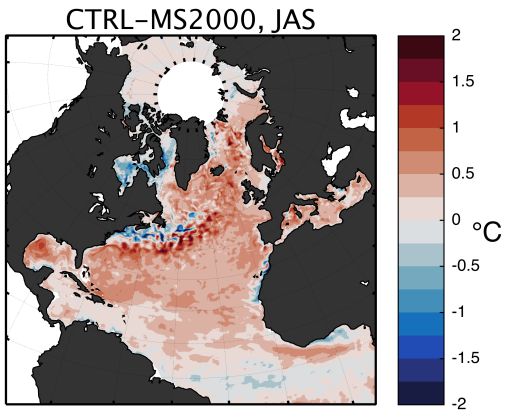

(c)

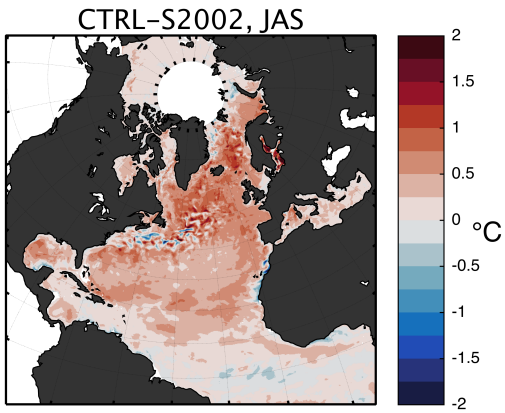

(d)

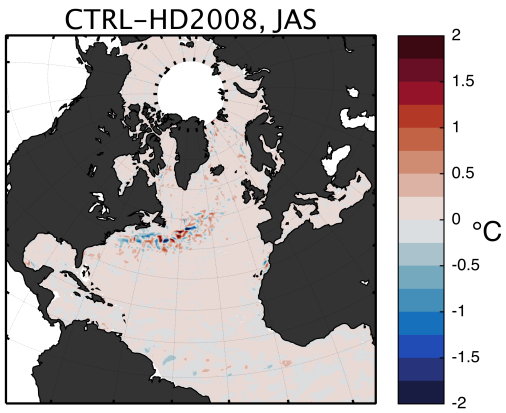

(e)

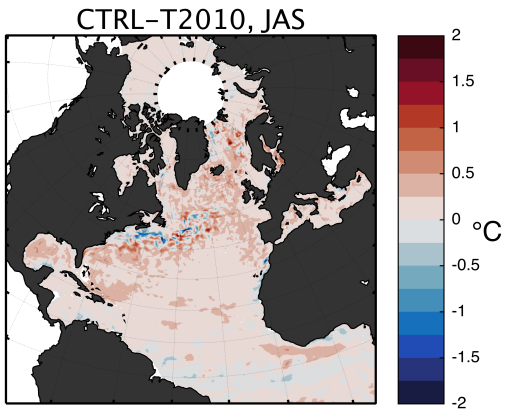

(f)

FIGURE 4.8: As Figure 4.7, but for July-August-September.

increases the bias relative to the reanalysis. MS2000 also exhibits a wider spread, with a larger amount of grid cells showing positive improvement than in the other model runs; however, the median improvement induced by MS2000 is clearly negative. A closer inspection of Figure 4.9(a) reveals (by overlapping notches) that the median improvements attributed to HD2008 and T2010—both of which have a median improvement of zero—cannot be distinguished from one another in terms of statistical significance.

The JFM improvement in the Gulf Stream region, depicted in Figure 4.9(b), resembles the situation shown in Figure 4.9(a), that is, MS2000 induces a largely negative improvement, while the remaining parameterisations have a comparatively neutral effect. It should be noted that the scale of the y axis is different from the other plots, and the spread exhibited by MS2000 is, in fact, larger in this region than in any other region. Also, in Region B, all medians are distinct at the 95 % significance level.

In the Labrador and Irminger seas (Figure 4.9(c)) none of the parameterisations has an obviously detrimental impact on the modelled SSTs; MS2000, however, again exhibits the largest spread in improvement. Furthermore, a statistically significant difference of the medians between S2002, HD2008 and T2010 cannot be asserted by a visual inspection of the notches surrounding the respective median lines.

The MS2000 parameterisation performs comparatively poorly—with the entire interquartile range comprising negative values—in the North and Norwegian Seas region, the improvement statistics of which are shown in Figure 4.9(d). Largely neutral or slightly negative improvement is induced by the other parameterisations, and all medians are significantly independent from one another.

To summarise Figure 4.9, MS2000 induces a largely negative JFM average SST improvement over the control run in all regions apart from Focus Region C. In accordance with previously shown results, HD2008 has a comparatively weak impact on the SST field, with median values consistently approximately zero and a relatively small spread in the distribution of the improvement within the focus regions. S2002 and T2010 produce similar improvement statistics in all focus regions, confirming the observations of their mutually comparable effects made previously in this thesis.

In contrast to the generally poor or neutral JFM average improvements seen in Figure 4.9, the JAS averages shown in Figure 4.10 exhibit positive improvement attributable to certain parameterisations in certain regions. In Region A—Figure 4.10(a)—clear positive improvement is produced by the MS2000, S2002 and T2010 parameterisations; the HD2008 median improvement, on the other hand, remains close to zero. Region B (Figure 4.10(b)) is characterised by more or less neutral improvement by all parameterisations; the S2002 median is, however, slightly positive (0.1°C). Note that the scale in Figure 4.10(b) differs from the other plots. In

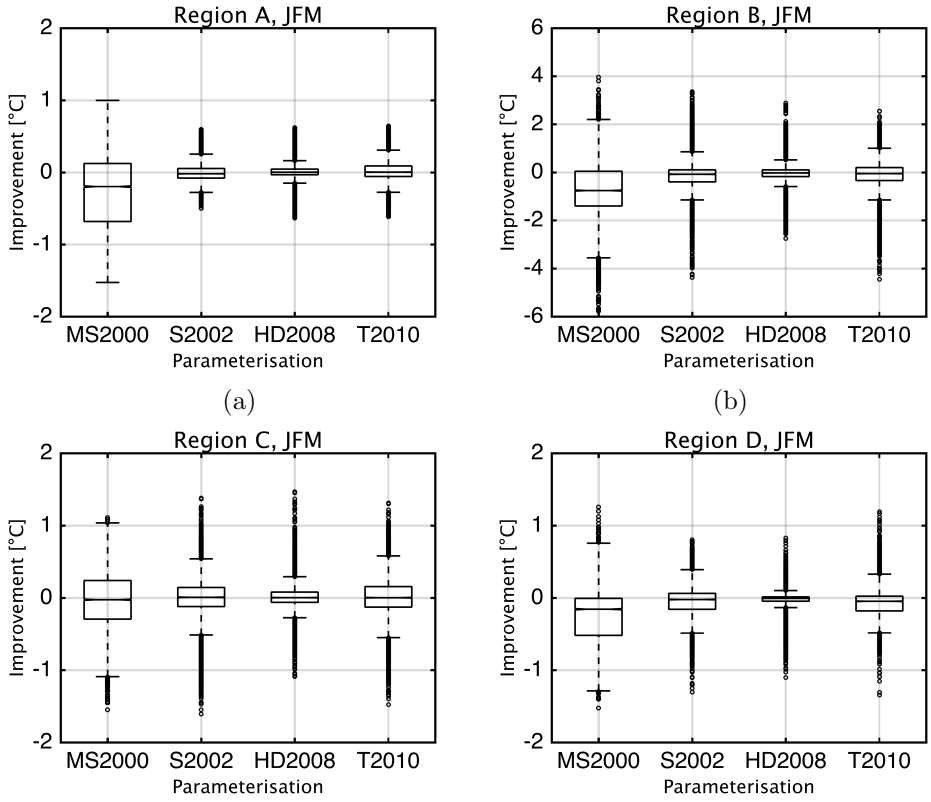

FIGURE 4.9: JFM-average box plots of the SST improvement for individual grid cells within each of the four focus regions. The upper and lower box boundaries indicate the levels of the upper and lower quartiles of the data, respectively, and the horizontal lines inside the boxes indicate the median values. The whiskers indicate the extreme values; outliers are marked with circles. A positive improvement indicates that the parameterisation produces an SST field closer to the reanalysis than that produced by the control run; a negative improvement indicates that the control run is more accurate. (a) shows Region A (The Sargasso Sea region), (b) shows region B (The Gulf Stream region), (c) shows region C (The Labrador and Irminger Seas region), and (d) shows region D (The North and Norwegian Seas region). Note that the temperature range in (b) differs from that in the other subfigures.

Figures 4.10(c) and 4.10(d), showcasing Regions C and D, the S2002 parameterisation produces the largest spreads in the SST improvement, a likely reflection of the enhanced turbulent mixing induced by stabilising surface buoyancy fluxes. In general, however, all parameterisations perform fairly well in regions C and, especially, D, with positive median improvements exhibited by MS2000, S2002 and T2010. HD2008 exhibits rather neutral improvement in region C, but also shows slight positive improvement in region D. All medians are statistically distinct in Figure 4.10(d), however in Figure 4.10(c), a statistically significant difference between MS2000 and T2010 cannot be detected.

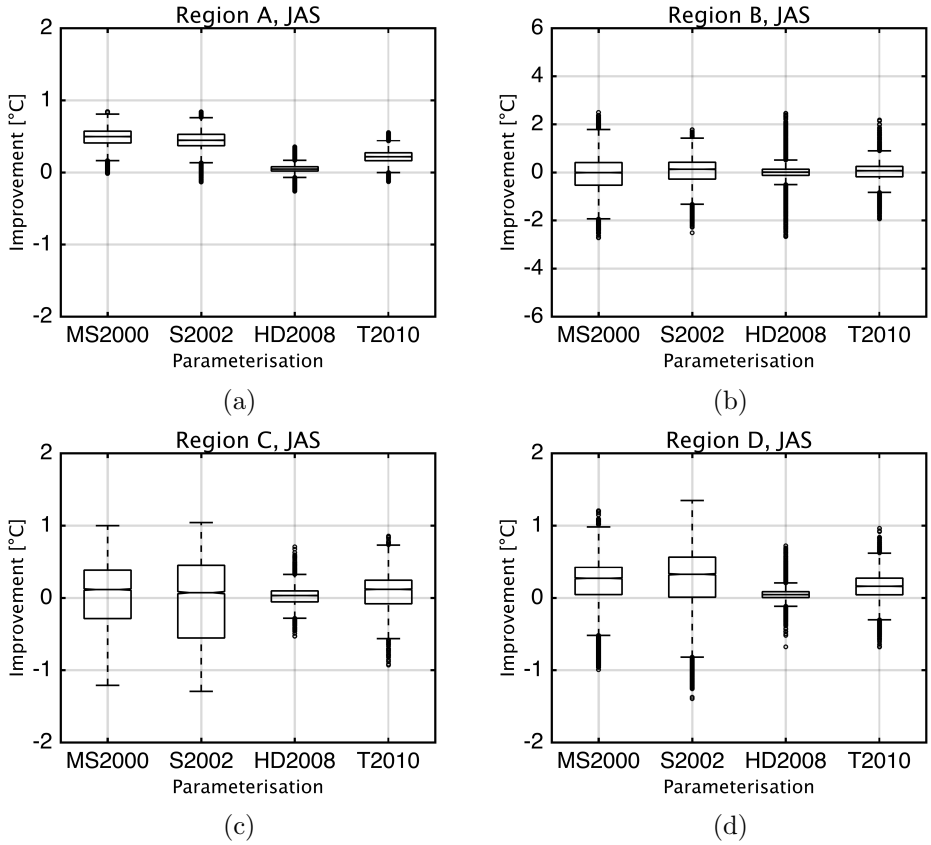

FIGURE 4.10: As Figure 4.9, but for JAS. Note that the temperature range in (b) differs from the other subfigures.

4.3 Vertical Temperature Profiles

The current section presents a comparison of the model run results against the measured subsurface temperature profiles contained in the EN4 dataset [Good et al., 2013]. The EN4 data consist of instantaneous profiles, and daily-average model temperatures are used in the comparison. A table (Table 5.1) which summarises numerically the results of the current section is included in Chapter 5.

4.3.1 The Sargasso Sea Region

Figures 4.11(a) and 4.11(b) show the January-February-March (JFM) average RMSE and bias profiles of the temperature for the Sargasso Sea region (Region A), and Figures 4.11(c) and 4.11(d) show equivalent plots of the July-August-September (JAS) averages. The staircase-like appearance of the curves is due to the vertical layering of the RMSE and bias fields described in Section 3.3.2. In the Northern Hemisphere winter, the majority of the model runs induce very similar RMSE profiles in this region (Figure 4.11(a)), with local maxima of roughly 1.75 °C and 1.5 °C evidently located at approximately 100 m and 600 m depths, respectively; some

degree of divergence is, however, observed among the model runs below 600 m, where the S2002 parameterisation produces the lowest RMSE. The MS2000 parameterisation displays the only contrasting behaviour, with consistently higher RMSE values induced throughout the vertical. In terms of bias (Figure 4.11(b)), the model runs excluding MS2000 again show similar behaviour, although T2010 and S2002 appear to somewhat reduce the warm (positive) bias over the control run in the uppermost 30 m. The strong mixing induced by MS2000, however, completely reverses the sign of the bias in the top 100 m, and below this, between 100 and 300 m, MS2000 causes a strong warm bias. At greater depths—between approximately 450 and 750 m—MS2000 slightly improves on the cold (negative) bias exhibited by the rest of the model runs. It is, nonetheless, highly questionable whether surface wave-induced effects should be expected to penetrate this deep in the water column.

In the Northern Hemisphere summer (JAS) average, MS2000 exhibits the lowest near-surface temperature RMSE (Figure 4.11(c)), although it quickly surpasses the RMSE exhibited by the other model runs around and below the few uppermost tens of metres. Collectively, all model runs produce reduced root-mean-square errors in the top few averaging layers in JAS compared to JFM, although the upper RMSE maximum is, simultaneously, larger in magnitude (approximately 2 °C) and has also shifted somewhat closer to the sea surface. A marked spread is visible among the model runs in the upper-level temperature bias of the JAS average (Figure 4.11(d)); MS2000 has the lowest-magnitude bias over the uppermost 100 m as well as in the 400-800 m range (where it reduces the cold bias exhibited by the model), whereas the control run produces the largest-magnitude bias over much of the top 100 m. T2010 is seen to slightly enhance the cold bias at large depths.

4.3.2 The Gulf Stream Region

In the Gulf Stream region (Region B), included in Figure 4.12, the wintertime, near-surface RMSEs (Figure 4.12(a)) increase as a result of implementing the Langmuir turbulence parameterisations. While the errors attributable to the control run are large from the outset (between $2.5-3$°C), the MS2000 parameterisation causes the surface RMSE to surpass 3.5°C; similarly, at 400-800 m depth, the errors due to MS2000 surpass those of the other model runs. A somewhat smaller increase in the winter near-surface RMSE is induced by both S2002 and T2010, whereas HD2008 closely follows CTRL. The JFM biases of Figure 4.12(b) likewise display an increase following the introduction of the parameterisations, suggesting that much of the enhanced RMSEs can be explained by the increases in bias. MS2000 introduces the largest increase in surface warm bias (on the order of one degree), followed, in order, by S2002, T2010 and HD2008. Interestingly, the S2002 warm bias decreases with depth and is the lowest of all model runs at intermediate depths (around 75–100 m); below this depth, the biases of all model runs apart from MS2000 converge, implying that the enhanced mixing is confined to a relatively shallow

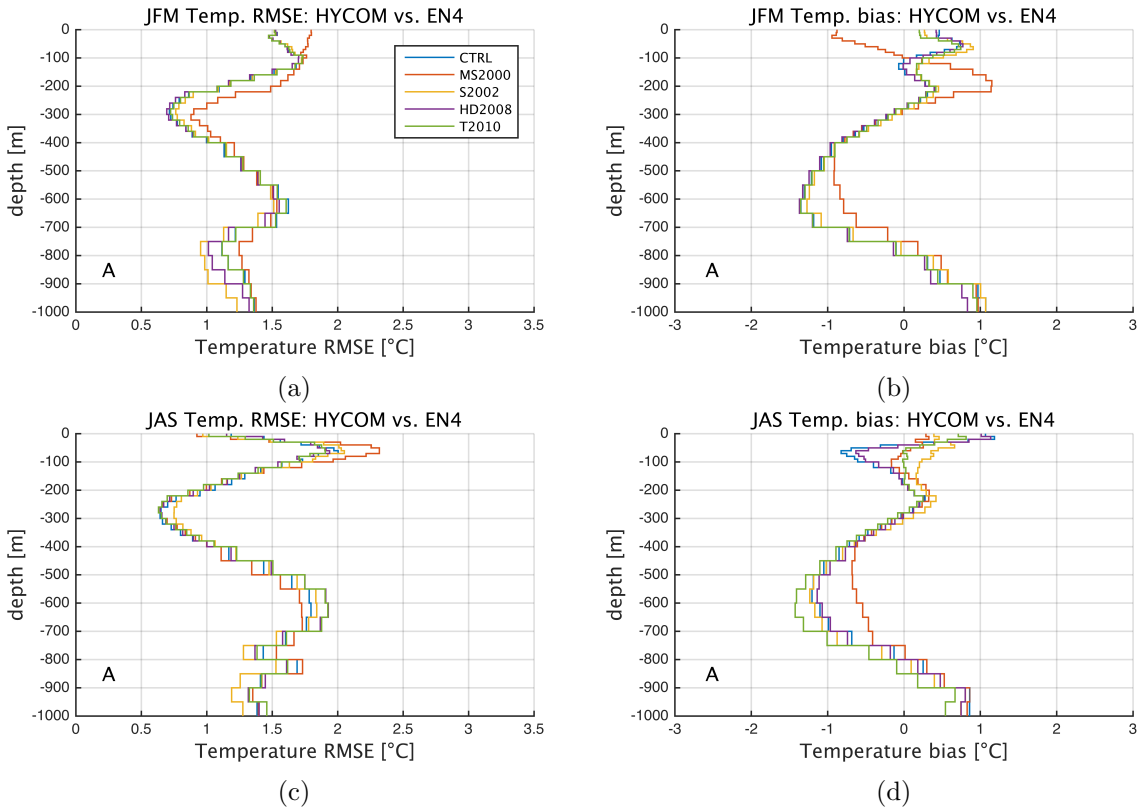

FIGURE 4.11: (left column) (a) JFM and (c) JAS vertical profiles of the root-mean-square errors (RMSE) of the modelled temperature fields against the observed temperature profiles contained in the EN4 dataset, averaged over the Sargasso Sea region (Region A). (right column) (b) JFM and (d) JAS vertical profiles of the bias of modelled against observed temperature profiles, averaged over the same region. The blue lines denote CTRL, the red lines MS2000, the blue lines S2002, the purple lines HD2008, and the green lines T2010.

layer beneath the surface. MS2000, on the other hand, affects the temperature bias down to a depth of around 800 m. This behaviour exhibited by MS2000 is a cause of concern, as such large-scale modifications of the model temperature fields can be expected to lead to significant changes in model performance over time.

The JAS RMSE profiles (Figure 4.12(c)) of CTRL, S2002, HD2008 and T2010 show coherence in the upper levels, but below 200 m, the RMSEs start to diverge, before converging again below roughly 800 m. Curiously, HD2008 clearly deviates from the control run in these depths. A large increase in RMSE is observed for the MS2000 run within the uppermost 500 m, pointing to vigorous mixing covering a large depth. The lowest-magnitude JAS surface temperature bias (Figure 4.12(d)) is exhibited by S2002, although at slightly larger depths (at around 20–50 m), CTRL and HD2008 have the smallest warm bias. MS2000 exhibits a strongly elevated warm bias of roughly 2–3°C relative to the other model runs throughout the uppermost 800 m, indicating that the parameterisation may cause the model to take up excessive amounts heat in this region. The remaining parameterisations, however, appear not to induce large deviations in bias from CTRL. In general, the magnitudes of the RMSEs and biases in the Gulf Stream region are larger

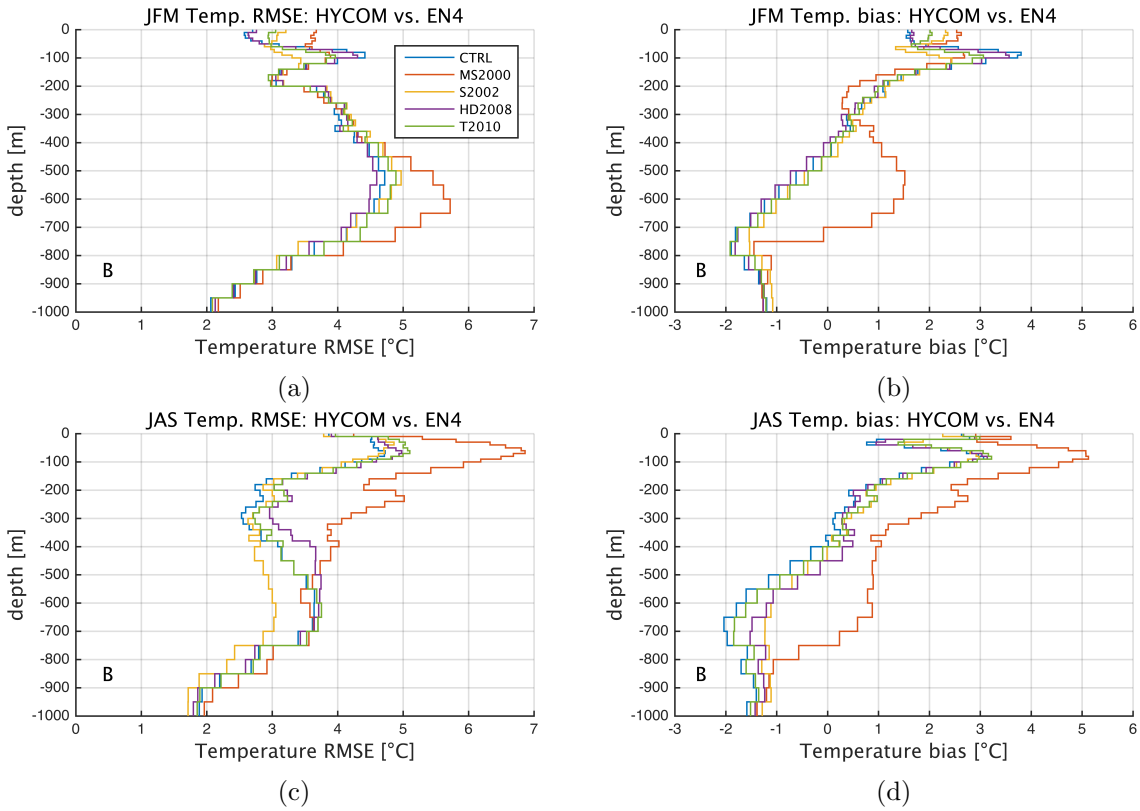

FIGURE 4.12: As Figure 4.11, for the Gulf Stream region (Region B). Note that the scale for both the RMSE and the bias differs from that used in the plots for the other regions.

than in the other focus regions; the errors in this region are, however, more likely to be related to large-scale dynamical errors in the model rather than to misrepresentations of the turbulent mixing. Nevertheless, the Langmuir turbulence parameterisations implemented here—especially the MS2000 parameterisation—have a substantial impact on the modelled temperature fields in the region; this is likely a result of relatively strong surface wave forcing in the region in all seasons.

4.3.3 The Labrador and Irminger Seas Region

Compared to the large impact on the RMSE and bias observed in the Gulf Stream region, the Labrador and Irminger Seas (Region C; Figure 4.13) experience markedly more moderate effects from the Langmuir turbulence parameterisations, presumably owing to the vigorous convective mixing that characterises the region and limits the impact of additional wind or wave-driven mixing. Also, contrary to previously seen results, MS2000 is shown to reduce the magnitudes of the JFM near-surface RMSE (Figure 4.13(a)) and warm bias (Figure 4.13(b)) over the control run.

In the summer season (Figures 4.13(c)), all model runs produce comparable surface RMSEs, but at intermediate (50–200 m) depths, S2002 improves over CTRL by nearly one degree.

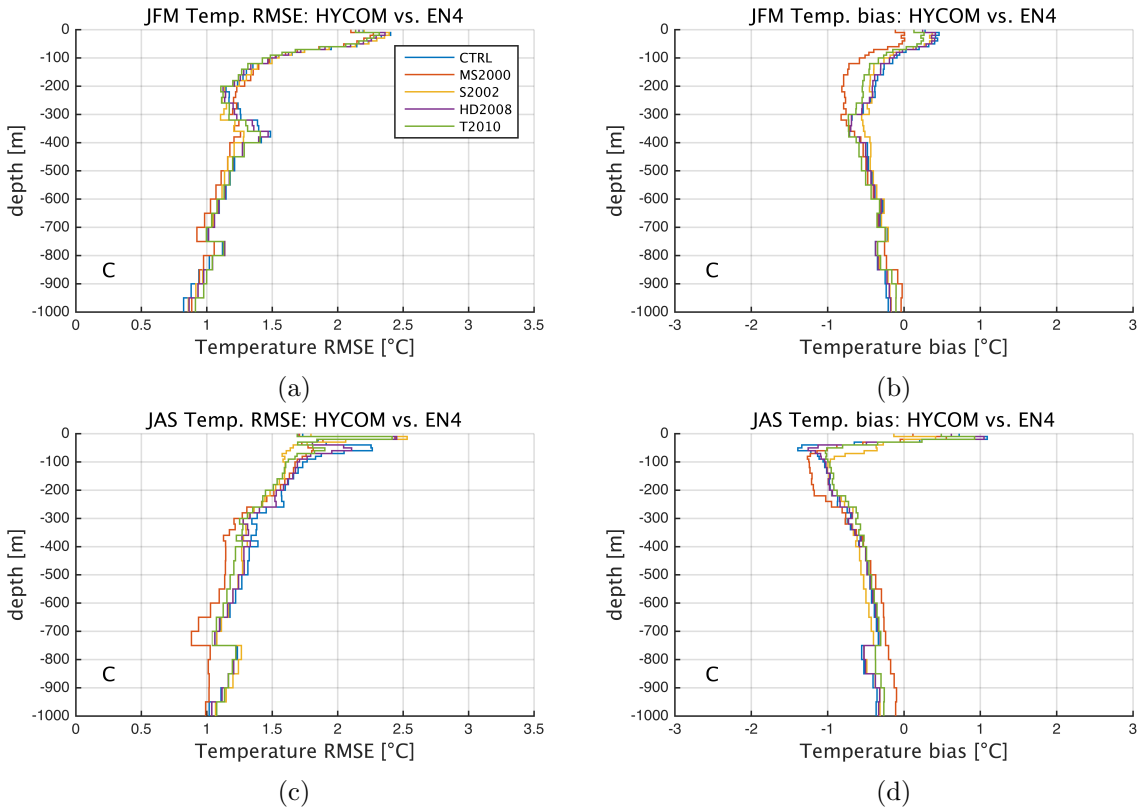

FIGURE 4.13: As Figure 4.11, for the Labrador and Irminger Seas region (Region C).

Furthermore, below 300 m, MS2000 induces the lowest RMSE estimates. In terms of JAS bias (Figure 4.13(d)), S2002 and MS2000 perform the best close to the surface, whereas deeper down the performances of all model runs more or less converge.

4.3.4 The North and Norwegian Seas Region

The JFM and JAS temperature RMSE and bias profiles for the North Sea and Norwegian Sea region (Region D) are shown in Figure 4.14. The lowest winter RMSEs (Figure 4.14(a)) are consistently produced by the control run in the top 200 m, while MS2000 produces the largest RMSE in roughly the uppermost 300 m. The JFM bias (Figure 4.14(b)) shows a similar situation: MS2000 induces the largest cold bias in the uppermost 600 m, followed by T2010, which also exhibits a slightly enhanced bias over the remaining model runs in the uppermost 400 m. It should be noted that both the RMSE and bias magnitudes as well as the magnitudes of the differences between the JFM model runs in Region D are relatively minor compared to, for example, the winter profiles of Region B (Figures 4.11(a) and 4.11(b)).

In the summer RMSE profiles (Figure 4.14(c)), S2002 marginally outperforms the other model runs in the near-surface layers, whereas at around 50–150 m depth the improvement by S2002 over the rest is more substantial—at best approximately 0.5°C. All parameterisations reduce

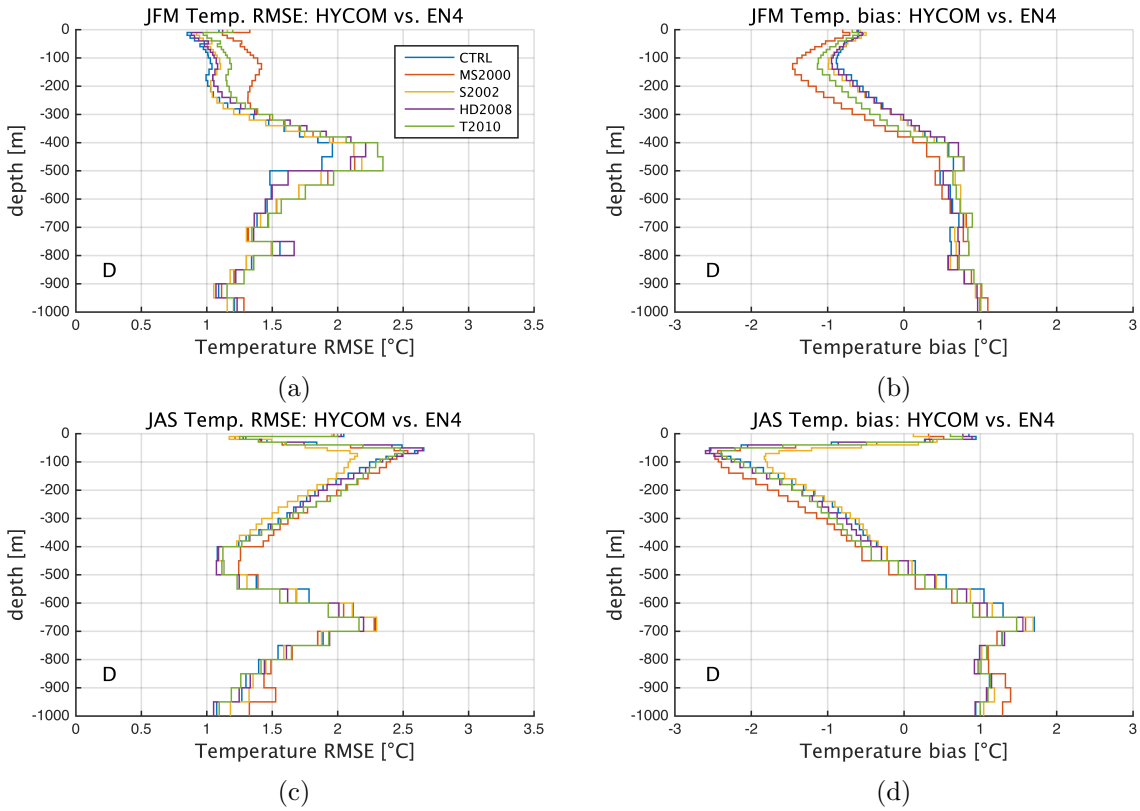

FIGURE 4.14: As Figure 4.11, for the North Sea and Norwegian Sea region (Region D).

the near-surface, JAS warm temperature bias over the control run (Figure 4.14(d)), with S2002 and MS2000 giving rise to the smallest bias in the top layer. Whereas the strong vertical mixing produced by MS2000 induces an increased cold bias below 100 m, S2002 continues to marginally improve on CTRL down to a depth of approximately 700 m. No clear improvement is observed in the HD2008 and T2010 runs, apart from the near-surface regions in which they produce slightly lower warm biases over CTRL. Generally, the JAS profiles converge at depths below roughly 700 m, although MS2000 diverges somewhat from the other runs below 800 m in Figures 4.14(c) and 4.14(d).

Chapter 5

Discussion

Several numerical modelling experiments have been performed in the present thesis using the TOPAZ4 [Sakov et al., 2012] version of the HYCOM ocean model [Bleck, 2002] to assess the effects of parameterising the effects of Langmuir turbulence in the K profile parameterisation (KPP) vertical mixing scheme [Large et al., 1994] by implementing the four parameterisations developed by McWilliams and Sullivan [2000], Smyth et al. [2002], Harcourt and D'Asaro [2008], and Takaya et al. [2010]. Following two-year model integrations spanning the years 2007-2008, the model results have been compared against the IFREMER mixed layer depth (MLD) climatology [de Boyer Montégut et al., 2004], the OSTIA sea-surface temperature reanalysis [Donlon et al., 2012], and the EN4 observational dataset of vertical temperature profiles [Good et al., 2013]. The main conclusion to be drawn from the results of the model experiments, presented in Chapter 4, is that parameterising the vertical mixing has a substantial impact on ocean model output: although comparatively slight differences were noted in the large-scale dynamics between the different model runs, the effects on local temperature fields and mixed-layer depths were considerable in large parts of the model domain, which covered the North Atlantic Ocean and parts of the Arctic Ocean. It is plausible that a more distinct impact would be observed also on the large-scale dynamics in longer-duration model integrations owing to the effects of varying temperature distributions on the model's internal pressure fields, which may require years to adjust to changes in the ambient environment [Griffies et al., 2000]. The results presented in the present thesis also show that overestimating the impact of a parameterised turbulent process can have significant consequences on ocean model temperature and mixed layer properties.

5.1 Evaluation of the Parameterisations

5.1.1 Impact on the Mixed-Layer Depth

A conspicuous wintertime feature present in all model runs (Figures 4.1(b)-(f)) is the deep mixing produced in the region surrounding the Southern tip of Greenland (included in Focus Region C). The IFREMER climatology (Figure 4.1(a)), on the other hand, exhibits more modest levels of mixing in the same region. The Labrador Sea, to the West of Southern Greenland, is a well-known site of intermediate-water formation, with deep convection induced by destabilising sea-surface heat fluxes episodically mixing the water masses down to depths exceeding 2000 m [Lazier et al., 2002]. Extratropical cyclones frequently pass through the region, owing to the area's close proximity to the mid-latitude storm track, generating not only enhanced evaporative surface heat losses, but also rough wind seas that cause significant Stokes drift-induced modifications to the local Ekman current profiles [Perrie et al., 2003]. It is probable that the deep wintertime Labrador Sea mixed layers produced in the model runs including Langmuir effects (Figures 4.1(c)-(f)) are a consequence of the combined influence of highly destabilising surface heat fluxes and periodically strong surface wave forcing. Similar results were observed in a coupled ocean-wave-atmosphere modelling study by Fan and Griffies [2014], who found that parameterising Langmuir turbulence in KPP—and using the Smyth et al. [2002] parameterisation in particular—weakened the water mass stratification in the Labrador Sea, thus creating more favourable conditions for deep convection to occur compared to a control run with no explicit wave forcing. Part of the obvious contrast between the deep modelled Labrador Sea MLDs and the comparatively shallow MLDs exhibited by the IFREMER climatology (Figure 4.1(a)) may be explained by a smoothing effect brought on by the high inter-annual variability known to characterise the deep convection in the region [e.g., Pickart et al., 2002]. The climatology is also constructed on a considerably coarser numerical grid than the HYCOM model runs used in this study (2° for the climatology, vs. approximately 0.12° for HYCOM); this lower resolution can be expected to naturally smoothen the deepest MLD estimates.

The impact on global MLDs induced by parameterising Langmuir mixing according to the McWilliams and Sullivan [2000] and Smyth et al. [2002] models has also been studied by Li et al. [2016], who compared mixed-layer depths produced by multiple-decade coupled wave-ocean and wave-ocean-atmosphere simulations (using Wavewatch III coupled with the POP2 ocean model and the CAM4 atmospheric model) with the de Boyer Montégut et al. [2004] MLD climatology. They found that the Northern-Hemisphere root-mean-square errors of the MLD induced by the Smyth et al. [2002] parameterisation were on the order of 5–20 m in summer months and on the order of 15–130 m in winter. The McWilliams and Sullivan [2000] gave higher RMSEs in the winter season, especially in high latitudes, whereas the summer errors were somewhat lower than those caused by Smyth et al. [2002]. In the Southern Ocean, the Smyth et al. [2002]

parameterisation was found to produce unrealistically vigorous mixing in both summer and winter. The HYCOM results obtained in the current study support the previous observations of overly energetic mixing attributed to using the McWilliams and Sullivan [2000] modification of KPP; the Smyth et al. [2002] modification is, however, shown to rather effectively restrain the winter mixing rates.

5.1.2 Temperature Response

In their fully coupled wave-ocean-atmosphere experiments, Li et al. [2016] found that KPP parameterisations of Langmuir turbulence had an effect on modelled temperature fields down to a depth of approximately 500 m. Enhanced North Atlantic deep convection, induced by the changes in the turbulent mixing, was shown to strengthen the modelled Atlantic meridional overturning circulation (AMOC) by approximately one Sverdrup (or one million m^3/s). While these fully coupled experiments were conducted with a parameterisation [Van Roekel et al., 2012] that is not included in the present thesis, the results of Li et al. [2016] show that temperature RMSEs were reduced at all subsurface depths as a result of including the parameterisation; the global surface temperatures, on the other hand, showed little or no improvement. The most substantial improvements (in terms of RMSE reduction) were observed at depths of approximately 100 m, and the effects on model salinity were found to be small.

Table 5.1 summarises the effects on the HYCOM surface and near-surface temperature fields induced by the five model runs that were performed as a part of the present thesis. In terms of SST (the first panel), none of the parameterised model runs show substantial improvement over the control run in winter months (the unparenthesised values); in fact, the majority show negative improvement in most focus regions, indicating that the control run outperforms the other model runs in reproducing the reanalysed OSTIA winter SST field. This, in turn, suggests that the standard model configuration may already overestimate the wind-induced and convective mixing in winter months. The largest negative JFM improvement is produced by the McWilliams and Sullivan [2000] parameterisation, and the moderate Harcourt and D'Asaro [2008] generally induces the smallest deviations from the control run. The positive improvement produced by McWilliams and Sullivan [2000], Smyth et al. [2002] and Takaya et al. [2010] in summer months (the values in parentheses), on the other hand, suggests that the control run mixes too weakly in more stably stratified conditions, especially at relatively low and high latitudes (the largest positive improvement is seen in focus regions A and D).

The lower two panels of Table 5.1 show the root-mean-square errors and biases of the temperature profiles, presented in Section 4.3, averaged over the uppermost 10 and 100 metres, respectively. It is obvious that the McWilliams and Sullivan [2000] parameterisation, again,

TABLE 5.1: Summary of the performances of the five model runs. The included performance metrics for the JFM (JAS in parentheses) averages are: the mean SST improvement within each focus region; the average temperature RMSE and bias for the top 10 m; and the average temperature RMSE and bias for the top 100 m. The best performer in each focus region and season is marked in blue, and the worst performers are marked in red.

			Model Run				
		Region	CTRL	MS2000	S2002	HD2008	T2010
Avg. I_{SST}	[°C]	A		-0.28 (0.48)	-0.01 (0.44)	0.01 (0.05)	0.02 (0.22)
		B		-0.64 (-0.09)	-0.18 (0.05)	-0.05 (-0.01)	-0.13 (0.02)
		C		-0.03 (0.06)	-0.01 (-0.04)	0.01 (0.03)	0.01 (0.08)
		D		-0.27 (0.22)	-0.06 (0.23)	-0.02 (0.05)	-0.08 (0.15)
RMSE [°C]	0–10 m	A	1.53 (1.19)	1.80 (0.92)	1.52 (0.97)	1.53 (1.15)	1.52 (1.02)
		B	2.70 (3.86)	3.67 (4.24)	3.21 (3.79)	2.76 (3.90)	3.05 (3.97)
		C	2.20 (1.73)	2.10 (1.71)	2.20 (1.80)	2.16 (1.69)	2.14 (1.69)
		D	1.09 (2.05)	1.33 (1.97)	1.16 (1.96)	1.12 (2.03)	1.20 (2.00)
Bias [°C]	0–10 m	A	0.46 (1.07)	-0.88 (0.29)	0.27 (0.39)	0.42 (1.01)	0.20 (0.71)
		B	1.57 (2.63)	2.53 (2.91)	2.32 (2.26)	1.65 (2.67)	2.01 (2.67)
		C	0.27 (0.72)	-0.11 (0.12)	0.25 (-0.13)	0.24 (0.62)	0.13 (0.49)
		D	-0.60 (0.85)	-0.80 (0.32)	-0.57 (0.12)	-0.61 (0.77)	-0.68 (0.61)
RMSE [°C]	0–100 m	A	1.58 (1.70)	1.77 (1.87)	1.59 (1.72)	1.58 (1.69)	1.58 (1.65)
		B	3.30 (4.50)	3.68 (6.13)	3.08 (4.55)	3.23 (4.68)	3.23 (4.82)
		C	2.05 (2.00)	1.97 (1.83)	2.05 (1.78)	2.01 (1.92)	1.98 (1.82)
		D	0.96 (2.15)	1.26 (2.06)	1.03 (1.84)	1.00 (2.14)	1.09 (2.06)
Bias [°C]	0–100 m	A	0.52 (-0.05)	-0.54 (0.10)	0.60 (0.43)	0.54 (0.06)	0.47 (0.28)
		B	2.34 (2.24)	2.41 (4.17)	1.99 (2.43)	2.22 (2.35)	2.14 (2.56)
		C	0.24 (-0.59)	-0.18 (-0.67)	0.17 (-0.39)	0.20 (-0.53)	0.06 (-0.46)
		D	-0.73 (-1.29)	-1.03 (-1.26)	-0.73 (-0.78)	-0.76 (-1.32)	-0.86 (-1.19)

produces the largest errors in most regions in the winter season. In the summer season, however, the control run performs the worst on a number of occasions; the 0–10 m bias, for example, is dominated by CTRL in regions A, C and D. It is also worthy to note that, while relatively rarely producing the best results, the Takaya et al. [2010] parameterisation never ranks last, despite often inducing mixing comparable to the Smyth et al. [2002] parameterisation.

To conclude, Table 5.1, which summarises the results presented in Chapter 4, suggests that enhancing the turbulent mixing in KPP by a positive definite function tends to unnecessarily increase the already-overly-high mixing rates produced by the standard HYCOM configuration, whereas in the summer the model benefits from the elevated levels of mixing induced by the introduction of the Langmuir turbulence parameterisations. Despite exhibiting a positive impact on the model temperatures in summer months, the deeply penetrating effects of the McWilliams and Sullivan [2000] parameterisation—seen in Section 4.3—are worrisome, and should be taken into consideration when assessing the physical credibility of the parameterisation.

TABLE 5.2: Langmuir enhancement factors F_{LT} applied on the vertical turbulent velocity W of the KPP scheme, as defined in the four Langmuir turbulence parameterisations compared in the current thesis.

Parameterisation	MS2000	S2002	HD2008	T2010
F_{LT}	$\left[1+\frac{0.080}{\mathrm{La}_t^4}\right]^{1/2}$	$\left[1+\frac{0.15\left(\frac{u_*^3}{u_*^3+0.6w_*^3}\right)^2}{\mathrm{La}_t^4}\right]^{1/2}$	$\left[1+\frac{0.098}{\mathrm{La}_t^2}\right]^{1/2}$	$\max(1,\mathrm{La}_t^{-2/3})$

5.1.3 Comparison of the Parameterisations

The differences between the four Langmuir turbulence parameterisations are most readily assessed by analysing the definitions of their respective enhancement factors, listed in Table 5.2. The deepest-reaching mixing is almost invariably produced by the McWilliams and Sullivan [2000] and Smyth et al. [2002] parameterisations, which, by design, are the most sensitive to variations in La_t. The Harcourt and D'Asaro [2008] parameterisation, characterised by the lowest sensitivity to La_t, generally exhibits the most marginal deviations from the control run, whereas the performance of the comparatively simplistic Takaya et al. [2010] parameterisation in many cases bears close resemblance to the Smyth et al. [2002] scheme.

Despite being based on relatively similar LES experiments, it is interesting to note that the McWilliams and Sullivan [2000] parameterisation has a markedly higher sensitivity to La_t compared to the Harcourt and D'Asaro [2008] parameterisation, which is formulated according to LES conducted by Li et al. [2005]. Both McWilliams and Sullivan [2000] and Li et al. [2005] use fixed, monochromatic wave forcing corresponding to an e-folding depth of the Stokes drift of $\delta_{St} = 4.77$ m; the former authors, however, impose a weak destabilising surface heat flux of 5 W/m^2, whereas the latter neglect diabatic effects entirely. Although the convective effects induced by the destabilising forcing used by McWilliams and Sullivan [2000] may produce slightly enhanced vertical velocity variances, they are unlikely to fully explain the factor-two difference in the power law dependence on La_t between the enhancement factors. Instead, the difference presumably stems largely from the practical methods in which the parameterisations were constructed in the respective studies. McWilliams and Sullivan [2000] produce two LES experiments with constant $\mathrm{La}_t = 0.3$ and $La = \infty$, and subsequently motivate their power law (2.43), with $\alpha = 2$, by "mathematical esthetics"; the constant $C_w = 0.080$ in the nominator is determined by fitting KPP diffusivity profiles to the LES. Li et al. [2005], on the other hand, perform a greater number of experiments with varying turbulent Langmuir number, and Harcourt and D'Asaro [2008] consequently construct their parameterisation (2.46) by fitting a curve through a plot [Figure 4 of Li et al., 2005] of scaled turbulence intensities corresponding to the LES experiments with varying La_t. While the results obtained in the present thesis, as well as previous studies [Fan and Griffies, 2014; Li et al., 2016], indicate that McWilliams and Sullivan [2000] overestimate the dependency of F_{LT} on La_t, Li et al. [2005] also suggest that their Figure

4 be interpreted with caution, as it is found to underestimate the turbulence intensity when compared to certain [D'Asaro and Dairiki, 1997] near-coast observations.

McWilliams and Sullivan [2000] recognised the potential for excessive boundary-layer mixing by their proposed parameterisation in convective and strongly wind-forced conditions; as the only independent variable in their enhancement factor is La_t, the turbulent vertical velocity will be enhanced to the same degree regardless of whether competing turbulence-enhancing processes are acting in the OBL simultaneously. Smyth et al. [2002] argue, likewise, that such an unbounded surface wave-forced enhancement of strongly convective turbulence produces unrealistically vigorous mixing; they, therefore, propose limiting the parameterised enhancement of W when the surface heat flux is destabilising ($B_f > 0$). This stability dependence is implemented in their parameterisation in the form of a convective velocity scale, $w_* = (\kappa B_f h_{bl})^{1/3}$, which acts to decrease the Langmuir-induced enhancement when the water column is convectively unstable. Likewise, the enhancement is stronger under stabilising surface forcing (i.e., when $w_* < 0$). However, because Smyth et al. [2002] wished to retain the effects of the McWilliams and Sullivan [2000] parameterisation in weakly convective conditions, they chose an enhancement factor that restricted the mixing in strongly stable conditions more than their LES results warranted. Considering that the McWilliams and Sullivan [2000] method is clearly unstable, as has been shown in both previous studies [Fan and Griffies, 2014; Li et al., 2016] as well as in the present thesis, it seems likely that the Smyth et al. [2002] could be improved by a reformulation that completely disregards the McWilliams and Sullivan [2000] results.

It is interesting to note the often similar results in terms of both modelled MLD and temperature fields induced by the Smyth et al. [2002] and Takaya et al. [2010] parameterisations. While the former has an explicit stability dependency, the latter is purely based on a scaling argument [Grant and Belcher, 2009]; nevertheless, the Takaya et al. [2010] scheme effectively manages to restrict the mixing in winter—similarly to the Smyth et al. [2002] and Harcourt and D'Asaro [2008] schemes—while still producing elevated mixing in the summer—something at which the more moderate Harcourt and D'Asaro [2008] scheme fails. This observation gives support to the accuracy of the Grant and Belcher [2009] scaling of Langmuir turbulence. Furthermore, being based on a scaling argument arguably grants the Takaya et al. [2010] parameterisation a more universal applicability than the other three, all of which are effectively based on regression analyses of relatively few idealised LES experiments. The recent results of Kukulka and Harcourt [2017]—showing that the similarity scaling of turbulence in surface wave-forced boundary layers may deviate from the Grant and Belcher [2009] scaling in choppy wind seas—indicate that the Takaya et al. [2010] parameterisation could be further improved by considering recent theoretical advances in the scaling laws.

5.2 Significance of the Boundary-Layer Depth

Although the present and previous studies have focused on analysing the modelled mixed-layer depth (owing to the prevalence of, and easy access to, oceanic datasets based on measurements of the MLD), the key parameter in the KPP mixing scheme is in fact the related, but distinct, boundary-layer depth h_{bl} [Large et al., 1994, see also Section 2.1.4]. The KPP boundary-layer depth controls the depth below the sea-surface over which the mixing scheme acts on the ocean model's momentum and scalar variables, and is defined in terms of a bulk Richardson number criterion (see (2.5)). This bulk Richardson number, in turn, depends on the surface and near-surface buoyancy fluxes as well as the resolved and unresolved velocity shears, the latter of which is directly modified by the Langmuir turbulence parameterisations implemented in the present study. It has recently been shown [Li and Fox-Kemper, 2017] that the standard, unmodified KPP scheme is skilful in reproducing boundary-layer depths similar to those produced by realistic LES experiments in convective and shear-dominated turbulence regimes, but in surface wave-modified Langmuir turbulence conditions the scheme consistently underestimates h_{bl}. This underestimation of h_{bl} is a potential source for the shallow summer MLD biases observed in previous studies that have implemented KPP in large-scale ocean and climate models [e.g., Belcher et al., 2012; Fan and Griffies, 2014; Li et al., 2016]. Although the present study opts to disregard the MLD as a validation parameter, the improvements in modelled SST (see Figures 4.9 and 4.10, and Table 5.1) produced by the McWilliams and Sullivan [2000] and Smyth et al. [2002] parameterisations—both known from previous studies to induce high, and occasionally excessive, rates of mixing, as discussed above—suggest that summertime shallow MLD biases are prevalent in the standard TOPAZ4 HYCOM representation of the North Atlantic as well.

Two methods have been proposed for alleviating the shallow h_{bl} biases in modifications of KPP intended to incorporate Langmuir turbulence effects. First, as suggested by Li et al. [2016], the vertical shear of the Stokes drift can be included in the definition of the bulk Richardson number, leading to an additional square of the Stokes drift in the denominator of (2.5).[1] It is, however, possible that this approach overestimates the contributions of the Stokes drift on the OBL turbulence structure: the unresolved turbulent velocity is, after all, already enhanced by a dependency on La_t (and hence U_S) as a consequence of the implementation of the Langmuir turbulence parameterisations. In addition, one must decide whether to use the surface value of the Stokes drift in the denominator, as in the definition of La_t, or a vertically averaged value. The use of the surface value is problematic because of the high sensitivity of the surface Stokes drift to the high-frequency wave components, which may not be expected to contain large amounts of energy; moreover, the Stokes shear decays rapidly with depth, further complicating the estimation of a surface value in a discretely layered ocean model [e.g., Breivik et al., 2014].

[1] Increasing the denominator of (2.5) will make the bulk Richardson number smaller in magnitude, thus delaying the fulfilment of the h_{bl} criterion, which requires that the number exceed a certain empirical threshold.

In the HYCOM runs conducted in the present thesis, the uppermost vertical layer has a constant 3 m thickness, and the surface Stokes drift values of the WW3 reanalysis are used to represent the entire uppermost layer. While this does not affect the La_t-dependent Langmuir turbulence parameterisations in KPP (as the 'true' surface value of the Stokes drift is used), the Stokes shear may be overestimated in the modified momentum equations which include the Stokes-Coriolis and the CL vortex forces. Increasing the vertical resolution of the ocean model, and especially implementing more crowded near-surface z layers, may provide a more realistic representation of the Stokes shear. However, preliminary testing (conducted by Alfatih Ali at NERSC; not included in the present study) indicates that the surface-wave modifications of the momentum equations induce a marginal impact (compared to the impact of parameterising Langmuir turbulence in the KPP mixing scheme) on multiple-year integrations of the TOPAZ4 HYCOM model.

As a second method for reducing the h_{bl} biases associated with the KPP scheme, Li and Fox-Kemper [2017] propose scaling the entrainment buoyancy flux $\overline{w'b'_e}$—defined as the value of the buoyancy flux at the depth where the buoyancy flux attains its minimum—to include the effects of pycnocline erosion induced by deeply-penetrating Langmuir turbulence. The authors find, using LES experiments, that Langmuir turbulence markedly increases the entrainment rate at the base of the OBL in weakly convective surface forcing conditions; modifying the KPP scheme to account for the enhanced entrainment is found to improve the KPP boundary-layer depth estimates, alongside a positive impact on simulated summertime mixed-layer depths in a large-scale ocean model. Implementing these modifications in the KPP scheme of HYCOM, or another large-scale ocean, model provides an interesting subject for future testing.

5.2.1 The Effects of Stratification

In the KPP scheme, the magnitude of h_{bl} is also constrained, under stabilising and neutral surface forcing conditions, by the classical theoretical length scales L_{MO} (the Monin-Obukhov length) and h_{Ek} (the Ekman layer depth), respectively, as discussed in Section 2.2.4. The mostly negligible impact on the modelled mixed-layer depths induced by interchanging L_{MO} with the Langmuir stability length L_{LT} of Belcher et al. [2012] in the h_{bl} constraint of the KPP code (see Figure 4.5) may indicate that the scaling fails to induce significant deviations from the classical Monin-Obukhov scaling, contrary to the widespread views in the ocean community [e.g., Belcher et al., 2012; Grant and Belcher, 2009; Sutherland et al., 2013] that wave-modified boundary-layer turbulence should be distinct from conventional shear-driven turbulence. However, the more plausible explanation for the marginal differences in modelled MLDs exhibited by Figure 4.5 is that the h_{bl} constraint in question is rarely invoked, implying that both L_{MO} and L_{LT} consistently exceed in magnitude the boundary-layer depth inferred by the bulk Richardson number criterion. It is also interesting to note that the regular L_{MO} constraint generally

produces deeper modelled MLD fields than the modified L_{LT} constraint. This may imply that the constraint is largely invoked under conditions of weak surface-wave forcing, such that $u_*^3 > w_{*L}^3 \equiv u_*^2 U_{S0}$. Moreover, in situations where the two velocity scales (i.e., the friction velocity and the Langmuir velocity scale) are equivalent, the inclusion of the von Karman constant ($\kappa = 0.4$) in the denominator of the definition of L_{MO} (see (2.40)) may contribute to the slightly larger h_{bl} values produced by the standard KPP configuration in which L_{MO} is the limiting parameter.

In a recent study of Langmuir turbulence in stably stratified oceanic boundary layers, Pearson et al. [2015] perform LES experiments which include surface heating in addition to an imposed surface wave field with $\mathrm{La}_t = 0.3$ (i.e., fully developed wind seas). They find that strengthening the stabilising surface heat fluxes increases the fraction of the total TKE production attributable to the Stokes production term in the wave-modified TKE budget (2.33). The relevant length scales for the estimation of the mixed and boundary-layer depths are found to be L_{LT} and the boundary-layer depth prior to the introduction of the stabilising surface heat flux; this prompts Pearson et al. [2015] to suggest that these parameters should be incorporated in the diagnosis of h_{ml} and h_{bl}. Additionally, the authors propose modifying the non-local heat flux parameterisation of the KPP scheme to include Stokes drift-induced effects on the production of the turbulent heat fluxes. These propositions also provide interesting subjects for future sensitivity experiments in HYCOM and other global and basin-scale ocean circulation models. In general, however, the dynamical properties of turbulence in stably stratified boundary layers are poorly understood [e.g., Mahrt, 2014], and advances in that area of research are needed to correctly parameterise their physics in large-scale models [Belcher et al., 2012].

5.3 Suggestions for Improving Parameterisations of Langmuir Mixing

Three of the four Langmuir turbulence parameterisations currently implemented in HYCOM (i.e., those tested in the present study) depend only on the ratio between the friction velocity u_* and the surface magnitude of the Stokes drift U_{S0}, quantified in terms of the turbulent Langmuir number La_t. In light of the above discussion, it may be questioned whether La_t alone can provide an accurate estimate of the sea state in a realistic setting which includes buoyancy forcing in addition to wind forcing. Li et al. [2005] find, using LES forced by both wind stress and surface heat fluxes (i.e., separate experiments from those on which the Harcourt and D'Asaro [2008] parameterisation is based), that the controlling parameters on OBL turbulence are La_t and a stability-dependent dimensionless parameter called the Hoenikker number, Ho [Li and Garrett, 1995]:

$$\mathrm{Ho} = 4\frac{B_f \delta_S}{U_S u_*^2}. \tag{5.1}$$

Whereas La_t relates to the transition between shear-driven and Langmuir turbulence, Ho is designed to separate buoyancy-driven, convective turbulence from Langmuir turbulence; the transition between the convective and Langmuir regimes is found by Li et al. [2005] to occur when $\mathrm{Ho} = \mathcal{O}(1)$. A similar parameter to Ho, in which the Stokes depth δ_{St} has been replaced with the—arguably more relevant (see Section 2.2.4 and references therein)—mixed-layer depth h_{ml}, is used by Belcher et al. [2012] and Sutherland et al. [2014] to describe characteristic sea states obtained from modelling results and observations, respectively. Regime diagrams in which La_t is plotted against the alternative Hoenikker number h_{ml}/L_{LT} reveal [see, e.g., Belcher et al., 2012, their Figure 3] that typical ocean states lie roughly in between Langmuir, shear-driven, and convective turbulence regimes; consequently, ignoring convective stability parameters in Langmuir turbulence parameterisations most likely gives an incomplete representation of the mixing induced by surface waves.

A rough estimate of the parameters required to represent surface wave-forced turbulence in a large-scale ocean model is readily acquired through a classical dimensional analysis.[2] Following the principles of the Buckingham Pi theory, described in Kundu et al. [2012, pp. 21–26], the following model variables may be selected to represent the state of the OBL in a realistic setting: the Stokes drift U_S is chosen to express the surface-wave forcing, τ the wind stress, B_f the surface buoyancy flux; h_{ml} is chosen as the relevant length scale, and ρ represents the water density. A functional dependence between the five aforementioned variables is sought for a function, such as the Langmuir enhancement factor F_{LT}, that incorporates the combined effects of Langmuir, shear-driven, and convective turbulence. The selected model variables are used to set up a so-called dimensional matrix, in which the dimensions of each variable are expressed in terms of powers of mass (M), length (L), and time (T):

	U_S	τ	B_f	h_{ml}	ρ
M	0	1	0	0	1
L	1	−1	2	1	−3
T	−1	−2	−3	0	0

(5.2)

The units of the wind stress, $[\mathrm{M}^1\mathrm{L}^{-1}\mathrm{T}^{-2}]$, are easily retrieved from the definition of the friction velocity, $u_* = (\tau/\rho)^{1/2}$, and the units of B_f can, for instance, be derived from the definition $L_{MO} = -u_*^3/(\kappa B_f)$. The rank of the dimensional matrix (5.2) is 3; consequently, the Buckingham theory predicts that the problem can be described in terms of two dimensionless parameters

[2] Dimensional analysis in classical mechanics builds on the principle that the study of natural phenomena is invariant to the units of measurement chosen to describe their properties. Hence, it is often convenient to express relationships between physical variables in dimensionless form [e.g., Kundu et al., 2012, p. 21].

(the number of dimensionless parameters is given by the difference between the number of variables and the rank of the dimensional matrix). An observant reader of the current thesis will immediately recognise $\mathrm{La}_t^2 = (\tau/\rho)/U_S$ as a potential parameter. Choosing U_S as the repeating variable, the second parameter must be formed by combining U_S, B_f, and h_{ml}. An obvious combination involves the cube of a velocity scale weighed against the product $B_f h_{ml}$. Using the Langmuir velocity scale $w_{*L}^3 = u_*^2 U_S$ of Grant and Belcher [2009] (see (2.38)) yields a second parameter of the form $B_f h_{ml}/w_{*L}^3$, which can be rewritten using (2.41) as h_{ml}/L_{LT}. The second dimensionless parameter can, therefore, be chosen as the alternative Hoenikker number used by Belcher et al. [2012] and Sutherland et al. [2014] to differentiate between turbulence regimes in realistic sea states.

The preceding dimensional analysis supports suggestions [e.g., Pearson et al., 2015; Smyth et al., 2002] that, instead of solely relying on La_t, Langmuir turbulence parameterisations should be formulated to include an explicit stability dependency. The KPP enhancement factor F_{LT} could, for instance, have the functional form

$$F_{LT} = f\left(\mathrm{La}_t, \frac{h_{ml}}{L_{LT}}\right). \tag{5.3}$$

The practical implementation of a h_{ml}-dependent parameterisation is, however, problematic owing to the high sensitivity of the MLD to the definition used (see Section 4.1). This could be resolved by extrapolating an estimate for the mixed-layer depth from known quantities, such as h_{bl}. Li and Fox-Kemper [2017], for instance, show that, in convective conditions, the ratio of h_{ml} to h_{bl} stays approximately constant at $h_{ml}/h_{bl} \approx 0.95$, making h_{bl} a fairly consistent estimator for h_{ml}.

Substantial attention has also been directed recently in the academic literature toward formulating alternative, more comprehensive definitions of La_t. It is known that the high sensitivity of the surface Stokes drift to high-wavenumber components of the wave field gives the Stokes drift a highly sheared near-surface profile [e.g., Breivik et al., 2014]. In order to avoid potentially overestimating the turbulent kinetic energy (TKE) production by giving unwarranted weight to these relatively low-energy waves, Harcourt and D'Asaro [2008] propose using a depth-averaged value of the Stokes drift in the definition of La_t. More recently, Kukulka and Harcourt [2017] show that the presence of short, high-wavenumber waves tends to increase the near-surface TKE dissipation; they consequently propose using a spectrally filtered Stokes drift, which in practice corresponds to a weighted vertical average, not much unlike the Harcourt and D'Asaro [2008] version.

The results of the present study show that the wintertime mixing in the standard HYCOM setup tends to be too vigorous in many regions of the North Atlantic model domain. As a

result, because all Langmuir turbulence parameterisations developed so far rely on positive definite enhancement factors, pre-existing winter SST biases tend to grow as a result of implementing the parameterisations. However, as shown by Craik [1977] and Leibovich [1977a], the Craik-Leibovich vortex force—the primary vorticity-stretching component in the wave-averaged dynamics typically applied in studies of Langmuir turbulence—can be viewed as being equivalent to a buoyancy force, capable of destabilising the water column. The instability induced by the vortex force manifests itself physically as Langmuir circulations, and requires that the waves and surface currents be aligned; if the waves oppose the currents—a situation which may arise, for instance, as swell generated in a distant storm propagates into a local windsea—the vortex force instead has a stabilising effect, as pointed out by Leibovich [1983] and, more recently, by Bühler [2014, p. 271]. This stabilising effect in the case of opposing waves and mean currents is to the author's best knowledge not accounted for in any existing Langmuir turbulence parameterisations, which currently only take into account the magnitude, or speed, of the (near) surface Stokes drift. Van Roekel et al. [2012] have developed a parameterisation which allows for misaligned winds and waves; testing of their scheme conducted by Li et al. [2016] has shown promising results, with improved agreement of model results with MLD and SST climatologies compared to results obtained with the McWilliams and Sullivan [2000] and Smyth et al. [2002] parameterisations. The Van Roekel et al. [2012] parameterisation, however, neglects any potential stabilising effects of opposing winds and waves.

5.4 Implicit and Neglected Factors in the Model

Because the original formulation of the KPP mixing scheme by Large et al. [1994] includes empirically determined parameters, such as the critical bulk Richardson number Ri_c, and because wind-generated surface waves are a ubiquitous feature of the OBL, it has been suggested [e.g., Wang et al., 2010] that Langmuir turbulence effects may already be implicitly incorporated in the standard, unmodified KPP scheme. Therefore, the additional enhancement of the unresolved turbulent velocity by La_t–dependent functions may overestimate the impact of surface waves on the turbulent mixing of near-surface waters. The question is addressed by Belcher et al. [2012], who argue that results indicating that winds and surface waves rarely coexist in equilibrium [e.g., Sullivan et al., 2008] provide evidence to the contrary: since the turbulent mixing induced by pure wind-driven shear markedly differs in its dynamical properties from surface wave-forced Langmuir turbulence, the parameterisations of the two processes should, according to Belcher et al. [2012], depend on distinct parameters. [Reichl et al., 2016], on the other hand, show that retuning the value of Ri_c in the KPP scheme in accordance with realistic LES simulations of purely wind shear-driven boundary layers results in a lower optimal threshold value ($\mathrm{Ri}_c = 0.235$, vs. the standard $\mathrm{Ri}_c = 0.3$); the correspondence of the retuned threshold with the critical value of 0.25 used in atmospheric applications suggests that the KPP

threshold implicitly contains contributions from processes, such as Langmuir turbulence, that are unique to the OBL. While potentially damping the overly energetic KPP representations of wintertime mixing in mid-latitude regions, the application of a retuned, lower Ri_c may further exacerbate the shallow summertime MLD biases that persist in many large-scale ocean models despite efforts [e.g., Fan and Griffies, 2014; Li et al., 2016] to incorporate previously neglected physics into the mixing schemes.

The HYCOM control run conducted in the present study is set up according to the standard TOPAZ4 configuration. Having been designed as an operational ocean forecasting system for the North Atlantic and Arctic Oceans, the performance of the TOPAZ4 system has been finely tuned to accurately represent the endemic water mass properties; Sakov et al. [2012] mention, for instance, that the HYCOM viscosity and diffusivity parameters have been modified to conform with empirical values. Likewise, river run-off and other fresh water sources have been optimised to replicate Arctic conditions. While these modifications might give the control run a certain advantage, the diffusivity modifications, especially, might also implicitly incorporate contributions from unresolved and neglected processes such as Langmuir turbulence. Also, in case the modifications happen to be suboptimal, they may also introduce biases that possibly overshadow improvements induced by implementing the Langmuir turbulence parameterisations.

Although the present thesis has focused on assessing the impact of introducing surface wave-induced effects in the mixing dynamics of HYCOM, it must be kept in mind that a number of distinct, potentially important mixing processes remain poorly represented and even unaccounted for in the model. As pointed out by [Belcher et al., 2012], inertial oscillations generated by rapidly varying winds are rarely resolved owing to the comparatively low frequency at which atmospheric forcing is applied to ocean models; persistent SST biases can also be attributed to shortcomings in the large-scale dynamics of a model such as a misrepresentation of the strength of the Atlantic meridional overturning circulation (AMOC) [Zhang and Zhao, 2015]. Furthermore, several additional surface wave-related processes—including wave breaking [Sullivan et al., 2004], wave-mesoscale eddy [Hamlington et al., 2014] and wave-submesoscale front interactions [Suzuki et al., 2016], and wave effects on the roughness scaling of the air-sea interface [Garfinkel et al., 2011]—have been neglected in the current work.

Chapter 6

Summary and Conclusions

Initially neglected in large-scale oceanic simulations due to the vast differences in scale between the surface waves and the general circulation [e.g., Yuan and Huang, 2012], a number of recent studies have investigated the impact of surface wave-enhanced turbulence in global and basin-scale ocean models, spurred on by theoretical advances [e.g., Li et al., 1995; McWilliams et al., 1997] that indicate that waves may significantly alter the form and magnitude of the crucial diapycnal mixing processes in the upper ocean boundary layer (OBL). Acquiring reliable measurements of turbulence in the wavy open ocean has always been, and still remains, a daunting challenge—a fact that severely complicates the real-world validation of wave-turbulence interaction theories [Sullivan and McWilliams, 2010]. Recent field experiments [e.g., Qiao et al., 2016], however, indicate that the modification of OBL turbulence by the surface wave field is indeed a phenomenon of substantial effect, and ought therefore to be considered in the mixing parameterisations of large-scale ocean and climate models. The present thesis has shown that the impact on selected OBL properties—namely, the mixed-layer depth (MLD), the sea-surface temperature (SST), and subsurface temperatures—of parameterising surface wave-induced Langmuir turbulence effects in the K profile parameterisation (KPP) mixing scheme of the HYCOM ocean model is substantial, and care must be taken when deciding to incorporate a parameterisation of the process in operational forecasts.

6.1 Main Results

The results of the present thesis show considerable spread in the model performance produced by implementing the different parameterisations. Furthermore, even though the parameterisations improved the model's performance in certain regions, situations were still found in which the standard model setup, which neglects explicit surface-wave effects, gave the best results when compared to observational datasets. The most marked improvements resulting from the

introduction of the Langmuir turbulence parameterisations were observed in the summer season, whereas in winter, the enhanced mixing produced by the parameterisations induced largely increased errors when compared to observational datasets.

The main findings of the present work can be summarised as follows:

- Although the impact of applying the Langmuir turbulence parameterisations in practice is highly local—in the sense that KPP is a purely one-dimensional mixing scheme—the model MLD and temperature response was shown to be basin-wide, and rapid adjustments were observed to enhanced turbulent diffusivities.
- The positive definite enhancement factors used in the parameterisations generally induce exaggerated levels of mixing in winter months, when the standard model configuration already produces vigorous, and possibly excessive mixing.
- The operational use of the McWilliams and Sullivan [2000] parameterisation is not recommended due to its tendency to induce unbounded mixing in common oceanic conditions, especially in mid and high latitudes.
- The practical implementation of the weakly-mixing Harcourt and D'Asaro [2008] parameterisation is unlikely to improve model performance considerably.
- The stability dependence of the Smyth et al. [2002] parameterisation was shown to prohibit excessive mixing in winter, while enhancing the mixing during conditions of stabilising surface buoyancy forcing.
- Promising results were produced by the Takaya et al. [2010], which, despite lacking a an explicit dependency on stability parameters, managed to both restrict winter mixing and produce noticeable enhancement of mixing rates in summer.

To conclude, both previous studies [Fan and Griffies, 2014; Li et al., 2016] and the present work have shown that the McWilliams and Sullivan [2000] parameterisation of Langmuir turbulence induces unstable model performance in a realistic oceanic setting. Therefore, it is recommended that the practical implementation of this parameterisation be neglected in future studies. The Harcourt and D'Asaro [2008] parameterisation, on the other hand, induces fairly modest changes to the modelled MLD and temperature fields. While the oceanographic community remains undecided regarding the true scale and magnitude of Langmuir turbulence-induced mixing in the global OBL [e.g., Thorpe, 2004], the present study indicates that marginal improvements, at best, can be achieved in model performance by implementing the parameterisation proposed by Harcourt and D'Asaro [2008] in a large-scale ocean model such as HYCOM.

Of the four parameterisations included in the present thesis, arguably the best results were achieved by implementing the Smyth et al. [2002] and Takaya et al. [2010] schemes. The

explicit stratification dependence of Smyth et al. [2002] was shown to efficiently restrict mixing rates in destabilising surface forcing conditions; however, its comparatively high sensitivity to variations in La_t—a consequence of being partly based on the McWilliams and Sullivan [2000] parameterisation—may lead to overly energetic mixing rates in conditions of weak buoyancy forcing. The encouraging results produced by the Takaya et al. [2010] parameterisation show that the successful similarity scaling of surface wave-forced boundary layers may lead to effective parameterisations of Langmuir turbulence, applicable to a wide range of oceanic conditions.

6.2 Suggestions for Future Work

Because none of the parameterisations included in the HYCOM test runs conducted in this thesis managed to consistently improve model performance in all seasons and all model regions, the author has the following remarks regarding future research on the subject.

- Continued testing and development of alternative Langmuir turbulence parameterisations for applications in large-scale ocean circulation models is recommended. Existing parameterisations that should be included in future tests include the misaligned wind and waves parameterisation of Van Roekel et al. [2012], the Pearson et al. [2015] proposals for improved boundary-layer depth estimation and non-local heat flux parameterisations, and the Li and Fox-Kemper [2017] suggestion of modifying the KPP entrainment buoyancy flux to account for pycnocline erosion by deeply-penetrating Langmuir turbulence.
- Controlling the magnitude of the enhancement of unresolved turbulent velocities in convectively unstable conditions, and allowing for stabilising effects in situations of opposing waves and currents are proposed as key focus points in the development of future parameterisations.
- The similarity scaling of surface wave-forced oceanic boundary layers remains one of the leading sources of uncertainty in the validation of parameterisations of Langmuir turbulence [Grant and Belcher, 2009]. While this is reason enough to continue pursuing improved scaling laws, the Takaya et al. [2010] parameterisation implemented in the present study has shown that mixing parameterisations based purely on scaling considerations have the potential to provide truthful representations of the mixing characteristics in realistic oceanic boundary layers.

As computing power continues to increase, enabling large-scale oceanic simulations to be run on grids of ever finer horizontal and vertical resolution, it is conceivable that certain subgrid-scale parameterisations will become increasingly obsolete in the future [e.g., Soufflet et al., 2016]. However, the large computing resources required by, for instance, long-term coupled

climate simulations—compounded by the vast scale separation between the small-scale OBL turbulence and the basin-scale general circulation—guarantee that the continued development of turbulent mixing parameterisations will, in all likelihood, remain a worthwhile endeavour in the foreseeable future. Developments in observation techniques suitable for rough oceanic conditions [e.g., Qiao et al., 2016] also promise to improve the general understanding of the validity of different parameterisations.

The inclusion of wind-driven surface wave effects in an operational ocean forecasting system such as TOPAZ will in all likelihood require coupling with a separate wave forecasting model. This is known to incur substantial increases in required computational resources [Li et al., 2016]—at any rate, if the sole purpose of the wave model is to provide input for the Langmuir turbulence parameterisations. However, surface wave forecasts are an integral component of operational ocean forecasting, contributing valuable information to actors in the shipping and offshore platform industries, as well as to search-and-rescue authorities. In climate-scale studies, coupled wave models can be used—for instance—to infer projections of future wave climate [e.g., Hemer et al., 2013], and to provide parameters for sea-surface drag coefficient estimates needed for accurately modelling the momentum fluxes between the atmosphere and the ocean [e.g., Donelan et al., 2004; Sullivan and McWilliams, 2010]. In this regard, the additional resources required for coupling designated wave models to operational ocean or climate models can hardly be considered wasteful. Based on the results of the present thesis, however, a full wave-ocean coupling cannot be expected to consistently improve HYCOM model performance with the current set of Langmuir turbulence parameterisations implemented in the KPP scheme that is in use in the TOPAZ4 system at NERSC. Therefore, it is reiterated that continued development and testing of parameterisations that perform optimally in a wide range of oceanic conditions and geographical regions is recommended.

Appendix A

Derivation of the Wave-Induced Shears

The originally reported expressions for the wave-induced shears [Ardhuin and Jenkins, 2006, their equations (10) and (11)] include erroneous factors of 0.5. This appendix shows the calculations made in the current thesis to arrive at the corrected expressions given in (2.31).

Applying the GLM definitions (2.20) and (2.21), on the vertical shear of the x component of the wave orbital velocities, $\widetilde{u}$, yields, to first order in wave slope, following Ardhuin and Jenkins [2006],

$$\overline{\frac{\partial \widetilde{u}}{\partial z}}^{L} = \overline{\frac{\partial \widetilde{u}}{\partial z}} + \overline{\xi_1 \frac{\partial}{\partial x}\frac{\partial \widetilde{u}}{\partial z}} + \overline{\xi_3 \frac{\partial}{\partial z}\frac{\partial \widetilde{u}}{\partial z}}, \tag{A.1}$$

where the first term, the Eulerian mean of the shear of the orbital velocity, is zero by definition. The remaining two terms can be written, using the linear wave theory definitions (2.29) and (2.30), as

$$\begin{aligned} \overline{\xi_1 \frac{\partial^2 \widetilde{u}}{\partial x \partial z}} &= \overline{-aF_{cs}\sin(kx-\omega t)[-ak^2\omega F_{ss}\sin(kx-\omega t)]} \\ &= \overline{a^2k^2\omega F_{ss}F_{cs}\sin^2(kx-\omega t)}, \end{aligned} \tag{A.2}$$

and

$$\begin{aligned}\overline{\xi_3 \frac{\partial^2 \widetilde{u}}{\partial z^2}} &= \overline{aF_{ss}\cos(kx-\omega t)ak^2\omega F_{ss}\cos(kx-\omega t)} \\ &= \overline{a^2k^2\omega F_{ss}F_{cs}\cos^2(kx-\omega t)}. \end{aligned} \tag{A.3}$$

Combining (A.2) and (A.3) and using an elementary trigonometric identity gives the first identity in (2.31), that is,

$$\begin{aligned}\overline{\frac{\partial \widetilde{u}}{\partial z}}^L &= a^2k^2\omega F_{ss}F_{cs}\overline{[\sin^2(kx-\omega t)+\cos^2(kx-\omega t)]} \\ &= a^2k^2\omega F_{ss}F_{cs}. \end{aligned} \tag{A.4}$$

Using the same procedure, it is straightforward to show that the GLM approximation of the horizontal gradient of the vertical orbital velocity $\widetilde{w}$ follows the same expression:

$$\overline{\frac{\partial \widetilde{w}}{\partial x}}^L = \overline{\frac{\partial \widetilde{w}}{\partial x}} + \overline{\xi_1 \frac{\partial}{\partial x}\frac{\partial \widetilde{w}}{\partial x}} + \overline{\xi_3 \frac{\partial}{\partial z}\frac{\partial \widetilde{w}}{\partial x}} = a^2k^2\omega F_{ss}F_{cs}. \tag{A.5}$$

In (A.5), the first term on the right-hand side of the first equality is again equal to zero owing to linear wave kinematics.

Appendix B

Changes made to the KPP code

The present Appendix displays the changes made to the main KPP Fortran code for HYCOM called *mxkprf.F*. The line numbering refers to the code in use in the TOPAZ4 system at the time of writing of the current thesis.

Line 579: Declared a variable *stksp* (surface Stokes speed, U_{S0}) for the calculation of the Langmuir velocity scale $w_{*L} = (u_*^2 U_S 0)^{1/3}$. This is needed in the calculation of Langmuir length scale L_{LC}.

Lines 1176-1181: Computed L_{LC} using *stksp* if Stokes dynamics are turned on (#if defined(STOKES)). This is done by redefining the variable hmonob(i,j) (the Monin-Obukhov length L_{MO}).

```
c --- limit check on hbl for negative (stablizing) surface buoyancy forcing
        bfsfc=buoyfl-swfrml*buoysw
        if (bfsfc.le.0.0) then
          bfsfc=bfsfc-epsil  !insures bfsfc never=0
\#if defined(STOKES)
          stksp=sqrt(usds(i,j)**2 + vsds(i,j)**2) ! Stokes speed
          hmonob(i,j)=min(-cmonob*stksp*ustar(i,j)**2/bfsfc, hblmax)
          ! Langmuir stability length (Belcher et al. 2012)
\#else
          hmonob(i,j)=min(-cmonob*ustar(i,j)**3/(vonk*bfsfc), hblmax)
\#endif
          hbl=max(hblmin,
     &            min(hbl,
     &                hekman(i,j),
     &                hmonob(i,j)))
        else
          hmonob(i,j)=hblmax
        endif
```

```
c
```

Lines 3942-3956: Fixed two lines in the Smyth et al. [2002] parameterisation: the original definition of w_*^3 had the wrong sign, and the maximum condition in the definition of the variable *cw* allowed division by *epsil*, which is a small number. This led to unrealistically deep mixing in conditions of $w_*^3 < 0$.

```
          case (2) ! Smyth et al, 2002 Ocean Dynamics 52, pp 104-115
                   !   Nonlocal fluxes and Stokes drift effects in the KPP
                   ! flang=max(1,min(5,sqrt(1+cw/La**4)))
            ucube=ust**3
c ---   note: surface density increases (column is destabilized) if bflux > 0
            !wcube=-vonk*bflux*zlevel  ! Original, wrong sign
            wcube=max(vonk*bflux*zlevel,0)  ! Changed sign 13.5.2017 + max cond.
            !cw   =0.15*(ucube/max(ucube + 0.6*wcube, epsil))**2 ! Original
            cw   =0.15*(ucube/(ucube + 0.6*wcube + epsil))**2 ! Removed max. cond.
            if (altrlangmr) then
               cw=cw*(1./scnew**4)
            endif
            flang=sqrt(1+cw*ustk2/(ust*ust + epsil))
            flang=max(1.0, flang)
            flang=min(5.0, flang)  !original used 5.0
```

Appendix C

Bilinear Interpolation

The current appendix shows the bilinear interpolation technique used to horizontally interpolate model variables to observation locations in the comparison against EN4 profiles. A description of the procedure can be found in, for example, Christiansen [1973], and will be briefly reproduced here. Suppose that an observation has the grid coordinates $(i+t, j+u)$, where t is a normalised longitudinal coordinate and u is a normalised latitudinal coordinate (i.e., u and t have no relation to either velocity nor time; see Figure C.1 for the normalisation formulas). The surrounding model temperatures are interpolated into the observation point as $p_{i+t,j+u} = a_1 p_{i,j} + a_2 p_{i+1,j} + a_3 p_{i+1,j+1} + a_4 p_{i,j+1}$, where the weighting coefficients $a_1, ..., a_4$ are given by

$$\begin{aligned} a_1 &= (1-t)(1-u); \\ a_2 &= t(1-u); \\ a_3 &= tu; \\ a_4 &= (1-t)u. \end{aligned} \tag{C.1}$$

The weighting coefficients are defined such that the p-point closest to the observation point gets assigned the highest weight, and the sum of all coefficients is equal to one. A schematic of the bilinear interpolation procedure is provided in Figure C.1.

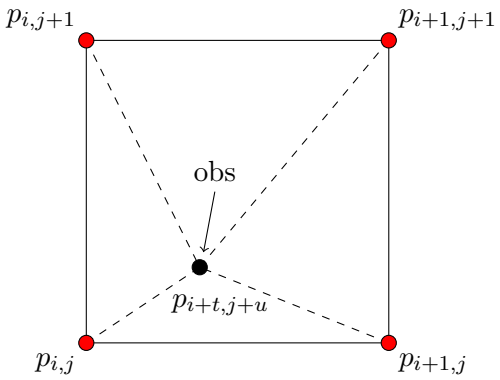

$$t = \frac{lon(obs) - lon(p_{i,j})}{lon(p_{i+1,j+1}) - lon(p_{i,j})}$$

$$u = \frac{lat(obs) - lat(p_{i,j})}{lat(p_{i+1,j+1}) - lat(p_{i,j})}$$

FIGURE C.1: Schematic of the bilinear interpolation of model variables (p) to the observation point (obs). The formulas used to calculate the normalised coordinates t, u from the longitudes (lon) and latitudes (lat) of the observation and model grid locations are provided on the right.

Bibliography

Adcroft, A., Hill, C., and Marshall, J. (1999). A new treatment of the Coriolis terms in C-grid models at both high and low resolutions. *Monthly Weather Review*, 127(8):1928–1936.

Agrawal, Y., Terray, E., Donelan, M., Hwang, P., Williams, A. J., Drennan, W. M., Kahma, K., and Krtaigorodskii, S. (1992). Enhanced dissipation of kinetic energy beneath surface waves. *Nature*, 359(6392):219–220.

Andrews, D. G. and McIntyre, M. (1978a). An exact theory of nonlinear waves on a Lagrangian-mean flow. *Journal of Fluid Mechanics*, 89(04):609–646.

Andrews, D. G. and McIntyre, M. (1978b). On wave-action and its relatives. *Journal of Fluid Mechanics*, 89(4):647–664.

Antonov, J., Locarnini, R., Boyer, R., Mishonov, A., and Garcia, H. (2006). World ocean atlas 2005. Vol. 2, Salinity.

Arakawa, A. and Lamb, V. R. (1977). Computational design of the basic dynamical processes of the UCLA general circulation model. *Methods in computational physics*, 17:173–265.

Ardhuin, F. and Jenkins, A. D. (2006). On the interaction of surface waves and upper ocean turbulence. *Journal of physical oceanography*, 36(3):551–557.

Ardhuin, F., Jenkins, A. D., and Belibassakis, K. A. (2008a). Comments on "The three-dimensional current and surface wave equations". *Journal of Physical Oceanography*, 38(6):1340–1350.

Ardhuin, F., Marié, L., Rascle, N., Forget, P., and Roland, A. (2009). Observation and estimation of Lagrangian, Stokes, and Eulerian currents induced by wind and waves at the sea surface. *Journal of Physical Oceanography*, 39(11):2820–2838.

Ardhuin, F., Rascle, N., and Belibassakis, K. A. (2008b). Explicit wave-averaged primitive equations using a generalized Lagrangian mean. *Ocean Modelling*, 20(1):35–60.

Aris, R. (1990). *Vectors, Tensors and the Basic Equations of Fluid Mechanics*. Courier Corporation.

Babanin, A. V., Ganopolski, A., and Phillips, W. R. (2009). Wave-induced upper-ocean mixing in a climate model of intermediate complexity. *Ocean Modelling*, 29(3):189–197.

Behrenfeld, M. J., O'Malley, R. T., Siegel, D. A., McClain, C. R., Sarmiento, J. L., Feldman, G. C., Milligan, A. J., Falkowski, P. G., Letelier, R. M., and Boss, E. S. (2006). Climate-driven trends in contemporary ocean productivity. *Nature*, 444(7120):752–755.

Belcher, S. and Hunt, J. (1998). Turbulent flow over hills and waves. *Annual Review of Fluid Mechanics*, 30(1):507–538.

Belcher, S. E., Grant, A. L., Hanley, K. E., Fox-Kemper, B., Van Roekel, L., Sullivan, P. P., Large, W. G., Brown, A., Hines, A., Calvert, D., et al. (2012). A global perspective on Langmuir turbulence in the ocean surface boundary layer. *Geophysical Research Letters*, 39(18).

Bennis, A.-C., Ardhuin, F., and Dumas, F. (2011). On the coupling of wave and three-dimensional circulation models: Choice of theoretical framework, practical implementation and adiabatic tests. *Ocean Modelling*, 40(3):260–272.

Bentsen, M., Evensen, G., Drange, H., and Jenkins, A. (1999). Coordinate transformation on a sphere using conformal mapping. *Monthly Weather Review*, 127(12):2733–2740.

Bleck, R. (2002). An oceanic general circulation model framed in hybrid isopycnic-Cartesian coordinates. *Ocean modelling*, 4(1):55–88.

Bleck, R., Halliwell Jr, G., Wallcraft, A., Carroll, S., Kelly, K., and Rushing, K. (2002). HYbrid Coordinate Ocean Model (HYCOM) user's manual: Details of the numerical code. *HYCOM, version*, 2(01).

Bleck, R., Rooth, C., Hu, D., and Smith, L. T. (1992). Salinity-driven thermocline transients in a wind-and thermohaline-forced isopycnic coordinate model of the North Atlantic. *Journal of Physical Oceanography*, 22(12):1486–1505.

Bleck, R. and Smith, L. T. (1990). A wind-driven isopycnic coordinate model of the North and Equatorial Atlantic Ocean. *J. Geophys. Res*, 95:3273–3285.

Breivik, Ø., Janssen, P. A., and Bidlot, J.-R. (2014). Approximate stokes drift profiles in deep water. *Journal of Physical Oceanography*, 44(9):2433–2445.

Bretherton, F. P. and Garrett, C. J. (1968). Wavetrains in inhomogeneous moving media. In *Proceedings of the Royal Society of London A: Mathematical, Physical and Engineering Sciences*, volume 302, pages 529–554. The Royal Society.

Brown, A. and Grant, A. (1997). Non-local mixing of momentum in the convective boundary layer. *Boundary-Layer Meteorology*, 84(1):1–22.

Brydon, D., Sun, S., and Bleck, R. (1999). A new approximation of the equation of state for seawater, suitable for numerical ocean models. *Journal of Geophysical Research: Oceans*, 104(C1):1537–1540.

Bühler, O. (2014). *Waves and mean flows*. Cambridge University Press.

Canuto, V. M., Howard, A., Cheng, Y., and Dubovikov, M. (2001). Ocean turbulence. Part I: One-point closure model—Momentum and heat vertical diffusivities. *Journal of Physical Oceanography*, 31(6):1413–1426.

Charnock, H. (1955). Wind stress on a water surface. *Quarterly Journal of the Royal Meteorological Society*, 81(350):639–640.

Chassignet, E. P., Hurlburt, H. E., Smedstad, O. M., Halliwell, G. R., Hogan, P. J., Wallcraft, A. J., Baraille, R., and Bleck, R. (2007). The HYCOM (hybrid coordinate ocean model) data assimilative system. *Journal of Marine Systems*, 65(1):60–83.

Chassignet, E. P., Smith, L. T., Bleck, R., and Bryan, F. O. (1996). A model comparison: numerical simulations of the north and equatorial Atlantic oceanic circulation in depth and isopycnic coordinates. *Journal of Physical Oceanography*, 26(9):1849–1867.

Chassignet, E. P., Smith, L. T., Halliwell, G. R., and Bleck, R. (2003). North Atlantic simulations with the Hybrid Coordinate Ocean Model (HYCOM): Impact of the vertical coordinate choice, reference pressure, and thermobaricity. *Journal of Physical Oceanography*, 33(12):2504–2526.

Chelton, D. B., Deszoeke, R. A., Schlax, M. G., El Naggar, K., and Siwertz, N. (1998). Geographical variability of the first baroclinic Rossby radius of deformation. *Journal of Physical Oceanography*, 28(3):433–460.

Christiansen, I. (1973). Numerical simulation of hydrodynamics by the method of point vortices. *Journal of Computational Physics*, 13(3):363–379.

Churchill, J. and Csanady, G. (1983). Near-surface measurements of quasi-Lagrangian velocities in open water. *Journal of physical oceanography*, 13(9):1669–1680.

Craig, P. D. and Banner, M. L. (1994). Modeling wave-enhanced turbulence in the ocean surface layer. *Journal of Physical Oceanography*, 24(12):2546–2559.

Craik, A. (1977). The generation of Langmuir circulations by an instability mechanism. *Journal of Fluid Mechanics*, 81(02):209–223.

Craik, A. and Leibovich, S. (1976). A rational model for Langmuir circulations. *Journal of Fluid Mechanics*, 73(03):401–426.

D'Asaro, E., Thomson, J., Shcherbina, A., Harcourt, R., Cronin, M., Hemer, M., and Fox-Kemper, B. (2014). Quantifying upper ocean turbulence driven by surface waves. *Geophysical Research Letters*, 41(1):102–107.

D'Asaro, E. A. (2001). Turbulent vertical kinetic energy in the ocean mixed layer. *Journal of Physical Oceanography*, 31(12):3530–3537.

D'Asaro, E. A. and Dairiki, G. T. (1997). Turbulence intensity measurements in a wind-driven mixed layer. *Journal of physical oceanography*, 27(9):2009–2022.

de Boyer Montégut, C., Madec, G., Fischer, A. S., Lazar, A., and Iudicone, D. (2004). Mixed layer depth over the global ocean: An examination of profile data and a profile-based climatology. *Journal of Geophysical Research: Oceans*, 109(C12).

Deardorff, J. W. (1970). Convective velocity and temperature scales for the unstable planetary boundary layer and for Rayleigh convection. *Journal of the atmospheric sciences*, 27(8):1211–1213.

Dee, D., Uppala, S., Simmons, A., Berrisford, P., Poli, P., Kobayashi, S., Andrae, U., Balmaseda, M., Balsamo, G., Bauer, P., et al. (2011). The ERA-Interim reanalysis: Configuration and performance of the data assimilation system. *Quarterly Journal of the royal meteorological society*, 137(656):553–597.

Dingemans, M. W. (1997). *Water Wave Propagation Over Uneven Bottoms: Part 1*. World Scientific.

Donelan, M., Haus, B., Reul, N., Plant, W., Stiassnie, M., Graber, H., Brown, O., and Saltzman, E. (2004). On the limiting aerodynamic roughness of the ocean in very strong winds. *Geophysical Research Letters*, 31(18).

Donlon, C., Rayner, N., Robinson, I., Poulter, D., Casey, K., Vazquez-Cuervo, J., Armstrong, E., Bingham, A., Arino, O., Gentemann, C., et al. (2007). The global ocean data assimilation experiment high-resolution sea surface temperature pilot project. *Bulletin of the American Meteorological Society*, 88(8):1197–1213.

Donlon, C. J., Martin, M., Stark, J., Roberts-Jones, J., Fiedler, E., and Wimmer, W. (2012). The operational sea surface temperature and sea ice analysis (OSTIA) system. *Remote Sensing of Environment*, 116:140–158.

Drange, H. and Simonsen, K. (1996). *Formulation of air-sea fluxes in the ESOP2 version of MICOM*. Nansen Environmental and Remote Sensing Center.

Durran, D. R. (2010). *Numerical methods for fluid dynamics: With applications to geophysics*, volume 32. Springer Science & Business Media.

Emanuel, K. A. (1999). Thermodynamic control of hurricane intensity. *Nature*, 401(6754):665–669.

Fairall, C. W., Bradley, E. F., Rogers, D. P., Edson, J. B., and Young, G. S. (1996). Bulk parameterization of air-sea fluxes for tropical ocean-global atmosphere coupled-ocean atmosphere response experiment. *Journal of Geophysical Research: Oceans*, 101(C2):3747–3764.

Faller, A. J. and Caponi, E. A. (1978). Laboratory studies of wind-driven Langmuir circulations. *Journal of Geophysical Research: Oceans*, 83(C7):3617–3633.

Fan, Y. and Griffies, S. M. (2014). Impacts of parameterized Langmuir turbulence and nonbreaking wave mixing in global climate simulations. *Journal of Climate*, 27(12):4752–4775.

Farmer, D. and Li, M. (1995). Patterns of bubble clouds organized by Langmuir circulation. *Journal of Physical Oceanography*, 25(6):1426–1440.

Ferland, J., Gosselin, M., and Starr, M. (2011). Environmental control of summer primary production in the Hudson Bay system: The role of stratification. *Journal of Marine Systems*, 88(3):385–400.

Foken, T. (2006). 50 years of the Monin–Obukhov similarity theory. *Boundary-Layer Meteorology*, 119(3):431–447.

Fox-Kemper, B., Danabasoglu, G., Ferrari, R., Griffies, S., Hallberg, R., Holland, M., Maltrud, M., Peacock, S., and Samuels, B. (2011). Parameterization of mixed layer eddies. III: Implementation and impact in global ocean climate simulations. *Ocean Modelling*, 39(1):61–78.

Garfinkel, C. I., Molod, A., Oman, L., and Song, I.-S. (2011). Improvement of the GEOS-5 AGCM upon updating the air-sea roughness parameterization. *Geophysical Research Letters*, 38(18).

Gargett, A. and Grosch, C. (2014). Turbulence process domination under the combined forcings of wind stress, the Langmuir vortex force, and surface cooling. *Journal of Physical Oceanography*, 44(1):44–67.

Garrett, C. (1976). Generation of Langmuir circulations by surface waves-a feedback mechanismangmuir circulations by surface waves-a feedback mechanism. *J. Mar. Res.*, 34:117–130.

Gaspar, P. (1988). Modeling the seasonal cycle of the upper ocean. *Journal of Physical Oceanography*, 18(2):161–180.

Gemmrich, J. R. and Farmer, D. M. (1999). Near-surface turbulence and thermal structure in a wind-driven sea. *Journal of Physical Oceanography*, 29(3):480–499.

Good, S. A., Martin, M. J., and Rayner, N. A. (2013). EN4: Quality controlled ocean temperature and salinity profiles and monthly objective analyses with uncertainty estimates. *Journal of Geophysical Research: Oceans*, 118(12):6704–6716.

Grant, A. L. and Belcher, S. E. (2009). Characteristics of Langmuir turbulence in the ocean mixed layer. *Journal of Physical Oceanography*, 39(8):1871–1887.

Griffies, S., Adcroft, A., Banks, H., Böning, C., Chassignet, E., Danabasoglu, G., Danilov, S., Deleersnijder, E., Drange, H., England, M., et al. (2009). Problems and prospects in large-scale ocean circulation models. *Proceedings of OceanObs*, 9:410–431.

Griffies, S. M., Böning, C., Bryan, F. O., Chassignet, E. P., Gerdes, R., Hasumi, H., Hirst, A., Treguier, A.-M., and Webb, D. (2000). Developments in ocean climate modelling. *Ocean Modelling*, 2(3):123–192.

Hallberg, R. (2005). A thermobaric instability of Lagrangian vertical coordinate ocean models. *Ocean Modelling*, 8(3):279–300.

Hallberg, R. (2013). Using a resolution function to regulate parameterizations of oceanic mesoscale eddy effects. *Ocean Modelling*, 72:92–103.

Halliwell, G. R. (2004). Evaluation of vertical coordinate and vertical mixing algorithms in the HYbrid-Coordinate Ocean Model (HYCOM). *Ocean Modelling*, 7(3):285–322.

Haltiner, G. J. W. and Terry, R. (1980). Numerical prediction and dynamic meteorology.

Hamlington, P. E., Van Roekel, L. P., Fox-Kemper, B., Julien, K., and Chini, G. P. (2014). Langmuir–submesoscale interactions: descriptive analysis of multiscale frontal spindown simulations. *Journal of Physical Oceanography*, 44(9):2249–2272.

Haney, R. L. (1991). On the pressure gradient force over steep topography in sigma coordinate ocean models. *Journal of physical Oceanography*, 21(4):610–619.

Harcourt, R. R. (2013). A second-moment closure model of Langmuir turbulence. *Journal of Physical Oceanography*, 43(4):673–697.

Harcourt, R. R. (2015). An improved second-moment closure model of Langmuir turbulence. *Journal of Physical Oceanography*, 45(1):84–103.

Harcourt, R. R. and D'Asaro, E. A. (2008). Large-eddy simulation of Langmuir turbulence in pure wind seas. *Journal of Physical Oceanography*, 38(7):1542–1562.

Hasselmann, K. (1970). Wave-driven inertial oscillations. *Geophysical and Astrophysical Fluid Dynamics*, 1(3-4):463–502.

Hemer, M. A., Fan, Y., Mori, N., Semedo, A., and Wang, X. L. (2013). Projected changes in wave climate from a multi-model ensemble. *Nature climate change*, 3(5):471–476.

Higdon, R. L. and de Szoeke, R. A. (1997). Barotropic-baroclinic time splitting for ocean circulation modeling. *Journal of Computational Physics*, 135(1):30–53.

Holm, D. D. (1996). The ideal Craik-Leibovich equations. *Physica D: Nonlinear Phenomena*, 98(2):415–441.

Holthuijsen, L. H. (2010). *Waves in oceanic and coastal waters*. Cambridge University Press.

Hunke, E. and Dukowicz, J. (1997). An elastic–viscous–plastic model for sea ice dynamics. *Journal of Physical Oceanography*, 27(9):1849–1867.

Iselin, C. (1939). The influence of vertical and lateral turbulence on the characteristics of the waters at mid-depths. *Eos, Transactions American Geophysical Union*, 20(3):414–417.

Ishihara, T., Gotoh, T., and Kaneda, Y. (2009). Study of high–Reynolds number isotropic turbulence by direct numerical simulation. *Annual Review of Fluid Mechanics*, 41:165–180.

Jähne, B. and Haußecker, H. (1998). Air-water gas exchange. *Annual Review of Fluid Mechanics*, 30(1):443–468.

Kantha, L., Wittmann, P., Sclavo, M., and Carniel, S. (2009). A preliminary estimate of the Stokes dissipation of wave energy in the global ocean. *Geophysical Research Letters*, 36(2).

Kantha, L. H. and Clayson, C. A. (1994). An improved mixed layer model for geophysical applications. *Journal of Geophysical Research: Oceans*, 99(C12):25235–25266.

Kantha, L. H. and Clayson, C. A. (2000). *Small scale processes in geophysical fluid flows*. Academic press.

Kantha, L. H. and Clayson, C. A. (2004). On the effect of surface gravity waves on mixing in the oceanic mixed layer. *Ocean Modelling*, 6(2):101–124.

Kara, A. B., Rochford, P. A., and Hurlburt, H. E. (2003). Mixed layer depth variability over the global ocean. *Journal of Geophysical Research: Oceans*, 108(C3).

Kitaigorodskii, S., Donelan, M., Lumley, J., and Terray, E. (1983). Wave-turbulence interactions in the upper ocean. part ii. statistical characteristics of wave and turbulent components of the random velocity field in the marine surface layer. *Journal of Physical Oceanography*, 13(11):1988–1999.

Komen, G. J., Cavaleri, L., Donelan, M., Hasselmann, K., Hasselmann, S., and Janssen, P. (1994). *Dynamics and modelling of ocean waves*. Cambridge university press.

Kraus, E. B. and Turner, J. S. (1967). A one-dimensional model of the seasonal thermocline II. The general theory and its consequences. *Tellus*, 19(1):98–106.

Kukulka, T. and Harcourt, R. R. (2017). Influence of Stokes Drift Decay Scale on Langmuir Turbulence. *Journal of Physical Oceanography*, 47(7):1637–1656.

Kukulka, T., Plueddemann, A. J., Trowbridge, J. H., and Sullivan, P. P. (2009). Significance of Langmuir circulation in upper ocean mixing: Comparison of observations and simulations. *Geophysical Research Letters*, 36(10).

Kundu, P. K., Cohen, I. M., and Dowling, D. R. (2012). *Fluid Mechanics*. Academic Press, Waltham, MA.

Lane, E. M., Restrepo, J. M., and McWilliams, J. C. (2007). Wave–current interaction: A comparison of radiation-stress and vortex-force representations. *Journal of physical oceanography*, 37(5):1122–1141.

Langmuir, I. (1938). Surface motion of water induced by wind. *Science*, 87(2250):119–123.

Large, W. G., McWilliams, J. C., and Doney, S. C. (1994). Oceanic vertical mixing: A review and a model with a nonlocal boundary layer parameterization. *Reviews of Geophysics*, 32(4):363–403.

Lazier, J., Hendry, R., Clarke, A., Yashayaev, I., and Rhines, P. (2002). Convection and restratification in the Labrador Sea, 1990–2000. *Deep Sea Research Part I: Oceanographic Research Papers*, 49(10):1819–1835.

Legates, D. R. and McCabe, G. J. (1999). Evaluating the use of "goodness-of-fit" measures in hydrologic and hydroclimatic model validation. *Water resources research*, 35(1):233–241.

Leibovich, S. (1977a). Convective instability of stably stratified water in the ocean. *Journal of Fluid Mechanics*, 82(03):561–581.

Leibovich, S. (1977b). On the evolution of the system of wind drift currents and Langmuir circulations in the ocean. Part 1. Theory and averaged current. *Journal of Fluid Mechanics*, 79(04):715–743.

Leibovich, S. (1980). On wave-current interaction theories of Langmuir circulations. *Journal of Fluid Mechanics*, 99(04):715–724.

Leibovich, S. (1983). The form and dynamics of Langmuir circulations. *Annual Review of Fluid Mechanics*, 15(1):391–427.

Levitus, S., JI, A., OK, B., TP, B., HE, G., AI, G., RA, L., AV, M., Seidov, D., Smolyar, I., et al. (2013). The world ocean database. *Data Science Journal*, 12:WDS229–WDS234.

Li, M. and Garrett, C. (1995). Is Langmuir circulation driven by surface waves or surface cooling? *Journal of Physical Oceanography*, 25(1):64–76.

Li, M., Garrett, C., and Skyllingstad, E. (2005). A regime diagram for classifying turbulent large eddies in the upper ocean. *Deep Sea Research Part I: Oceanographic Research Papers*, 52(2):259–278.

Li, M., Zahariev, K., and Garrett, C. (1995). Role of Langmuir circulation in the deepening of the ocean surface mixed layer. *Science*, 270(5244):1955.

Li, Q. and Fox-Kemper, B. (2017). Assessing the effects of Langmuir turbulence on the entrainment buoyancy flux in the ocean surface boundary layer. *Journal of Physical Oceanography*, 0(0):null.

Li, Q., Fox-Kemper, B., Breivik, Ø., and Webb, A. (2017). Statistical models of global Langmuir mixing. *Ocean Modelling*, 113:95–114.

Li, Q., Webb, A., Fox-Kemper, B., Craig, A., Danabasoglu, G., Large, W. G., and Vertenstein, M. (2016). Langmuir mixing effects on global climate: WAVEWATCH III in CESM. *Ocean Modelling*, 103:145–160.

Li, S., Song, J., and Fan, W. (2013). Effect of Langmuir circulation on upper ocean mixing in the South China Sea. *Acta Oceanologica Sinica*, 32(3):28.

Lombardo, C. and Gregg, M. (1989). Similarity scaling of viscous and thermal dissipation in a convecting surface boundary layer. *Journal of Geophysical Research: Oceans*, 94(C5):6273–6284.

Longuet-Higgins, M. S. and Stewart, R. (1964). Radiation stresses in water waves; a physical discussion, with applications. In *Deep Sea Research and Oceanographic Abstracts*, volume 11, pages 529–562. Elsevier.

Mahrt, L. (2014). Stably stratified atmospheric boundary layers. *Annual Review of Fluid Mechanics*, 46:23–45.

Marshall, J., Hill, C., Perelman, L., and Adcroft, A. (1997). Hydrostatic, quasi-hydrostatic, and nonhydrostatic ocean modeling. *Journal of Geophysical Research: Oceans*, 102(C3):5733–5752.

McDougall, T. J. and Church, J. A. (1986). Pitfalls with the Numerical Representation of Isopycnal Diapycnal Mixing. *Journal of Physical Oceanography*, 16(1):196–199.

McGill, R., Tukey, J. W., and Larsen, W. A. (1978). Variations of box plots. *The American Statistician*, 32(1):12–16.

McIntyre, M. (1981). On the 'wave momentum' myth. *Journal of Fluid Mechanics*, 106:331–347.

McWilliams, J. C., Huckle, E., Liang, J.-H., and Sullivan, P. P. (2012). The wavy Ekman layer: Langmuir circulations, breaking waves, and Reynolds stress. *Journal of Physical Oceanography*, 42(11):1793–1816.

McWilliams, J. C. and Restrepo, J. M. (1999). The wave-driven ocean circulation. *Journal of Physical Oceanography*, 29(10):2523–2540.

McWilliams, J. C. and Sullivan, P. P. (2000). Vertical mixing by Langmuir circulations. *Spill Science & Technology Bulletin*, 6(3):225–237.

McWilliams, J. C., Sullivan, P. P., and Moeng, C.-H. (1997). Langmuir turbulence in the ocean. *Journal of Fluid Mechanics*, 334(1):1–30.

Mellor, G. (2003). The three-dimensional current and surface wave equations. *Journal of Physical Oceanography*, 33(9):1978–1989.

Mellor, G. (2008). The depth-dependent current and wave interaction equations: a revision. *Journal of Physical Oceanography*, 38(11):2587–2596.

Mellor, G. (2016). On theories dealing with the interaction of surface waves and ocean circulation. *Journal of Geophysical Research: Oceans*, 121(7):4474–4486.

Mellor, G. and Yamada, T. (1982). Development of a turbulence closure model for geophysical fluid problems. *Reviews of Geophysics*, 20(4):851–875.

Melville, W. K. (1996). The role of surface-wave breaking in air-sea interaction. *Annual review of fluid mechanics*, 28(1):279–321.

Mentaschi, L., Besio, G., Cassola, F., and Mazzino, A. (2013). Problems in RMSE-based wave model validations. *Ocean Modelling*, 72:53–58.

Monin, A. and Obukhov, A. (1954). Basic laws of turbulent mixing in the atmosphere near the ground. *Tr. Akad. Nauk SSSR Geofiz. Inst*, 24(151):163–187.

Noh, Y. and Jin Kim, H. (1999). Simulations of temperature and turbulence structure of the oceanic boundary layer with the improved near-surface process. *Journal of Geophysical Research: Oceans*, 104(C7):15621–15634.

Noh, Y., Min, H. S., and Raasch, S. (2004). Large eddy simulation of the ocean mixed layer: The effects of wave breaking and Langmuir circulation. *Journal of physical oceanography*, 34(4):720–735.

O'Brien, J. J. (1970). A note on the vertical structure of the eddy exchange coefficient in the planetary boundary layer. *Journal of the Atmospheric Sciences*, 27(8):1213–1215.

Osborn, T. (1980). Estimates of the local rate of vertical diffusion from dissipation measurements. *Journal of Physical Oceanography*, 10(1):83–89.

Paskyabi, M. B., Zieger, S., Jenkins, A. D., Babanin, A., and Chalikov, D. (2014). Sea surface gravity wave-wind interaction in the marine atmospheric boundary layer. *Energy Procedia*, 53:184–192.

Pearson, B. C., Grant, A. L., Polton, J. A., and Belcher, S. E. (2015). Langmuir turbulence and surface heating in the ocean surface boundary layer. *Journal of Physical Oceanography*, 45(12):2897–2911.

Perrie, W., Tang, C., Hu, Y., and DeTracy, B. (2003). The impact of waves on surface currents. *Journal of physical oceanography*, 33(10):2126–2140.

Phillips, N. A. (1957). A coordinate system having some special advantages for numerical forecasting. *Journal of Meteorology*, 14(2):184–185.

Phillips, O. (1977). *The Dynamics of the Upper Ocean*. Cambridge University Press.

Pickart, R. S., Torres, D. J., and Clarke, R. A. (2002). Hydrography of the Labrador Sea during active convection. *Journal of Physical Oceanography*, 32(2):428–457.

Plueddemann, A. J., Smith, J. A., Farmer, D. M., Weller, R. A., Crawford, W. R., Pinkel, R., Vagle, S., and Gnanadesikan, A. (1996). Structure and variability of Langmuir circulation during the Surface Waves Processes Program. *Journal of Geophysical Research: Oceans*, 101(C2):3525–3543.

Polton, J. A. and Belcher, S. E. (2007). Langmuir turbulence and deeply penetrating jets in an unstratified mixed layer. *Journal of Geophysical Research: Oceans*, 112(C9).

Pope, S. (2000). *Turbulent Flows*. Cambridge University Press.

Press, W. H. (2007). *Numerical recipes 3rd edition: The art of scientific computing*. Cambridge university press.

Price, J. F., Weller, R. A., and Pinkel, R. (1986). Diurnal cycling: Observations and models of the upper ocean response to diurnal heating, cooling, and wind mixing. *Journal of Geophysical Research: Oceans*, 91(C7):8411–8427.

Qiao, F., Yuan, Y., Deng, J., Dai, D., and Song, Z. (2016). Wave–turbulence interaction-induced vertical mixing and its effects in ocean and climate models. *Phil. Trans. R. Soc. A*, 374(2065):20150201.

Qiao, F., Yuan, Y., Yang, Y., Zheng, Q., Xia, C., and Ma, J. (2004). Wave-induced mixing in the upper ocean: Distribution and application to a global ocean circulation model. *Geophysical Research Letters*, 31(11).

Rascle, N. and Ardhuin, F. (2013). A global wave parameter database for geophysical applications. Part 2: Model validation with improved source term parameterization. *Ocean Modelling*, 70:174–188.

Rascle, N., Ardhuin, F., Queffeulou, P., and Croizé-Fillon, D. (2008). A global wave parameter database for geophysical applications. Part 1: Wave-current–turbulence interaction parameters for the open ocean based on traditional parameterizations. *Ocean Modelling*, 25(3):154–171.

Rascle, N., Ardhuin, F., and Terray, E. A. (2006). Drift and mixing under the ocean surface: A coherent one-dimensional description with application to unstratified conditions. *Journal of Geophysical Research: Oceans*, 111(C3).

Reichl, B. G., Wang, D., Hara, T., Ginis, I., and Kukulka, T. (2016). Langmuir turbulence parameterization in tropical cyclone conditions. *Journal of Physical Oceanography*, 46(3):863–886.

Richman, J., Szoeke, R., and Davis, R. (1987). Measurements of near-surface shear in the ocean. *Journal of Geophysical Research: Oceans*, 92(C3):2851–2858.

Sakov, P., Counillon, F., Bertino, L., Lisæter, K., Oke, P., and Korablev, A. (2012). TOPAZ4: an ocean-sea ice data assimilation system for the North Atlantic and Arctic. *Ocean Science*, 8(4):633.

Sallée, J.-B., Shuckburgh, E., Bruneau, N., Meijers, A. J., Bracegirdle, T. J., and Wang, Z. (2013). Assessment of Southern Ocean mixed-layer depths in CMIP5 models: Historical bias and forcing response. *Journal of Geophysical Research: Oceans*, 118(4):1845–1862.

Skyllingstad, E. D. (2000). Scales of Langmuir circulation generated using a large-eddy simulation model. *Spill Science & Technology Bulletin*, 6(3):239–246.

Skyllingstad, E. D. and Denbo, D. W. (1995). An ocean large-eddy simulation of Langmuir circulations and convection in the surface mixed layer. *Journal of Geophysical Research: Oceans*, 100(C5):8501–8522.

Smith, J. A. (1992). Observed growth of Langmuir circulation. *Journal of Geophysical Research: Oceans*, 97(C4):5651–5664.

Smith, J. A. (1996). Observations of Langmuir circulation, waves, and the mixed layer. *The Air Sea Interface: Radio and Acoustic Sensing, Turbulence, and Wave Dynamics*, pages 613–622.

Smith, J. A. (1999). Observations of wind, waves, and the mixed layer: the scaling of surface motion. *The Wind-Driven Air–Sea Interface*, pages 231–238.

Smyth, W. D., Skyllingstad, E. D., Crawford, G. B., and Wijesekera, H. (2002). Nonlocal fluxes and Stokes drift effects in the K-profile parameterization. *Ocean Dynamics*, 52(3):104–115.

Soufflet, Y., Marchesiello, P., Lemarié, F., Jouanno, J., Capet, X., Debreu, L., and Benshila, R. (2016). On effective resolution in ocean models. *Ocean Modelling*, 98:36–50.

Stull, R. B. (1988). *An Introduction to Boundary Layer Meteorology*. Springer Science & Business Media.

Sullivan, P. P., Edson, J. B., Hristov, T., and McWilliams, J. C. (2008). Large-eddy simulations and observations of atmospheric marine boundary layers above nonequilibrium surface waves. *Journal of the Atmospheric Sciences*, 65(4):1225–1245.

Sullivan, P. P. and McWilliams, J. C. (2010). Dynamics of winds and currents coupled to surface waves. *Annual Review of Fluid Mechanics*, 42:19–42.

Sullivan, P. P., McWILLIAMS, J. C., and Melville, W. K. (2004). The oceanic boundary layer driven by wave breaking with stochastic variability. Part 1. Direct numerical simulations. *Journal of Fluid Mechanics*, 507:143–174.

Sullivan, P. P., McWILLIAMS, J. C., and Melville, W. K. (2007). Surface gravity wave effects in the oceanic boundary layer: Large-eddy simulation with vortex force and stochastic breakers. *Journal of Fluid Mechanics*, 593:405–452.

Sun, S., Bleck, R., Rooth, C., Dukowicz, J., Chassignet, E., and Killworth, P. (1999). Inclusion of thermobaricity in isopycnic-coordinate ocean models. *Journal of Physical Oceanography*, 29(10):2719–2729.

Sutherland, G., Christensen, K., and Ward, B. (2014). Evaluating Langmuir turbulence parameterizations in the ocean surface boundary layer. *Journal of Geophysical Research: Oceans*, 119(3):1899–1910.

Sutherland, G., Ward, B., and Christensen, K. (2013). Wave-turbulence scaling in the ocean mixed layer. *Ocean Science*, 9(4):597.

Suzuki, N. and Fox-Kemper, B. (2016). Understanding Stokes forces in the wave-averaged equations. *Journal of Geophysical Research: Oceans*, 121(5):3579–3596.

Suzuki, N., Fox-Kemper, B., Hamlington, P. E., and Van Roekel, L. P. (2016). Surface waves affect frontogenesis. *Journal of Geophysical Research: Oceans*, 121(5):3597–3624.

Takaya, Y., Bidlot, J.-R., Beljaars, A., and Janssen, P. A. (2010). Refinements to a prognostic scheme of skin sea surface temperature. *Journal of Geophysical Research: Oceans*, 115(C6).

Teixeira, M. and Belcher, S. (2002). On the distortion of turbulence by a progressive surface wave. *Journal of Fluid Mechanics*, 458:229–267.

Teixeira, M. and Belcher, S. (2010). On the structure of Langmuir turbulence. *Ocean Modelling*, 31(3):105–119.

Tennekes, H. and Lumley, J. L. (1972). *A first course in turbulence*. MIT press.

Terray, E., Donelan, M., Agrawal, Y., Drennan, W., Kahma, K., Williams, A. J., Hwang, P., and Kitaigorodskii, S. (1996). Estimates of kinetic energy dissipation under breaking waves. *Journal of Physical Oceanography*, 26(5):792–807.

Thomson, R. E. and Emery, W. J. (2014). *Data analysis methods in physical oceanography*. Elsevier, 3rd edition.

Thorpe, S. (1984). The effect of Langmuir circulation on the distribution of submerged bubbles caused by breaking wind waves. *Journal of Fluid Mechanics*, 142:151–170.

Thorpe, S. (2004). Langmuir circulation. *Annu. Rev. Fluid Mech.*, 36:55–79.

Thorpe, S., Osborn, T., Jackson, J., Hall, A., and Lueck, R. (2003). Measurements of turbulence in the upper-ocean mixing layer using Autosub. *Journal of Physical Oceanography*, 33(1):122–145.

Tolman, H. L., Balasubramaniyan, B., Burroughs, L. D., Chalikov, D. V., Chao, Y. Y., Chen, H. S., and Gerald, V. M. (2002). Development and implementation of wind-generated ocean surface wave Modelsat NCEP. *Weather and forecasting*, 17(2):311–333.

Tolman, H. L. et al. (2009). User manual and system documentation of WAVEWATCH III TM version 3.14. *Technical note, MMAB Contribution*, 276:220.

Troen, I. and Mahrt, L. (1986). A simple model of the atmospheric boundary layer; sensitivity to surface evaporation. *Boundary-Layer Meteorology*, 37(1-2):129–148.

Tsai, W.-T., Chen, S.-M., and Moeng, C.-H. (2005). A numerical study on the evolution and structure of a stress-driven free-surface turbulent shear flow. *Journal of Fluid Mechanics*, 545:163–192.

Uppala, S. M., Kållberg, P., Simmons, A., Andrae, U., Bechtold, V. d., Fiorino, M., Gibson, J., Haseler, J., Hernandez, A., Kelly, G., et al. (2005). The ERA-40 re-analysis. *Quarterly Journal of the royal meteorological society*, 131(612):2961–3012.

Vallis, G. K. (2006). *Atmospheric and oceanic fluid dynamics: fundamentals and large-scale circulation*. Cambridge University Press.

van den Bremer, T. and Breivik, Ø. (2017). Stokes drift. *Accepted for publ in Phil Trans R Soc Lond A*, page 23.

Van Roekel, L., Fox-Kemper, B., Sullivan, P., Hamlington, P., and Haney, S. (2012). The form and orientation of Langmuir cells for misaligned winds and waves. *Journal of Geophysical Research: Oceans*, 117(C5).

Wallcraft, A., Metzger, E., and Carroll, S. (2009). Software design description for the hybrid coordinate ocean model (HYCOM), Version 2.2. Technical report, NAVAL RESEARCH LAB STENNIS SPACE CENTER MS OCEANOGRAPHY DIV.

Wang, Y., Counillon, F., Bethke, I., Keenlyside, N., Bocquet, M., and Shen, M.-l. (2017). Optimising assimilation of hydrographic profiles into isopycnal ocean models with ensemble data assimilation. *Ocean Modelling*, 114:33–44.

Wang, Y., Qiao, F., Fang, G., and Wei, Z. (2010). Application of wave-induced vertical mixing to the K profile parameterization scheme. *Journal of Geophysical Research: Oceans*, 115(C9).

Wanninkhof, R., Asher, W. E., Ho, D. T., Sweeney, C., and McGillis, W. R. (2009). Advances in quantifying air-sea gas exchange and environmental forcing.

Weber, J. E. (1983). Attenuated wave-induced drift in a viscous rotating ocean. *Journal of Fluid Mechanics*, 137:115–129.

Webster, P. J., Clayson, C. A., and Curry, J. A. (1996). Clouds, radiation, and the diurnal cycle of sea surface temperature in the tropical western Pacific. *Journal of Climate*, 9(8):1712–1730.

Weijer, W., Sloyan, B. M., Maltrud, M. E., Jeffery, N., Hecht, M. W., Hartin, C. A., van Sebille, E., Wainer, I., and Landrum, L. (2012). The Southern Ocean and its climate in CCSM4. *Journal of Climate*, 25(8):2652–2675.

Weller, R. A. and Price, J. F. (1988). Langmuir circulation within the oceanic mixed layer. *Deep Sea Research Part A. Oceanographic Research Papers*, 35(5):711–747.

Willmott, C. J. and Matsuura, K. (2005). Advantages of the mean absolute error (MAE) over the root mean square error (RMSE) in assessing average model performance. *Climate research*, 30(1):79–82.

Wu, J. (1975). Wind-induced drift currents. *Journal of Fluid Mechanics*, 68(01):49–70.

Wunsch, C. and Ferrari, R. (2004). Vertical mixing, energy, and the general circulation of the oceans. *Annu. Rev. Fluid Mech.*, 36:281–314.

Yuan, Y. and Huang, N. E. (2012). A reappraisal of ocean wave studies. *Journal of Geophysical Research: Oceans*, 117(C11).

Zeng, X. and Beljaars, A. (2005). A prognostic scheme of sea surface skin temperature for modeling and data assimilation. *Geophysical Research Letters*, 32(14).

Zhang, L. and Zhao, C. (2015). Processes and mechanisms for the model SST biases in the North Atlantic and North Pacific: A link with the Atlantic meridional overturning circulation. *Journal of Advances in Modeling Earth Systems*, 7(2):739–758.

Zweng, M. M. and Münchow, A. (2006). Warming and freshening of Baffin Bay, 1916–2003. *Journal of Geophysical Research: Oceans*, 111(C7).